NEW MODEL OF EDDY CURRENT LOSS CALCULATION AND APPLICATIONS FOR PARTIAL CORE TRANSFORMERS

Huo, Xi Ting

A thesis submitted in partial fulfilment

of the requirements for the degree of

Master of Engineering

Department of Electrical and Computer Engineering

at the

University of Canterbury,

Christchurch, New Zealand.

November 2009

Abstract

This thesis first explains the eddy current and the phenomenon of skin effect, where the resultant flux flows near the surface of the metal. A new flux direction perspective is created for steel laminations, from which derivations of the eddy current resistance and power losses in different directions are developed assuming uniform flux conditions. The developed method compares with a proposed theory through experimental data. The results from the comparison support the validity of the developed derivations.

Two uniform flux generators and their billets construction are introduced. The power loss between two cubic billets with different orientations is compared. A Finite Element Analysis (FEA) program is used to show the difference between lamination alignments. To prove the validity of the developed theory, two experiments were performed using two different electroheating apparatus. The results give scale factors from which the theoretical values can be matched to the experimental ones. Due to the poorer construction of the first apparatus, the scale factor of measured to computed losses is 1.15. The scale factor for the second apparatus can be taken as unity, revealing a good match between theory and measurements.

After verification of the developed equations for uniform flux experiments, the focus of the eddy current loss calculation turned to partial core transformers. The flux background of a cubical core is reviewed. Three key factors (L', K_{ec} and β_a) are introduced into the eddy current power loss model. L' is a length which indicates the region of the flux spreading at the ends of the core. K_{ec} as a ratio indicates how much of the main flux spreads at the ends of the core. β_a is the ratio of the winding axial length and winding thickness. Using simulations from the Finite Element Analysis (FEA) program MagNet, a partial core side view with the flux distribution and flux density from two orthogonal angles is created. A flux linkage comparison between the experimental results and the

returned values from MagNet verifies the high accuracy of the flux plot in MagNet. The eddy current power loss model is then built up with equations. The relationships amongst the three key factors are studied and confirmed using the experimental results.

Normally, a partial core transformer uses a cylindrical partial core rather than a cubical partial core, to reduce the amount of winding material. Therefore, a further goal was to prove the developed model for cylindrical partial core transformers. The construction differences between the cubical and cylindrical core is discussed. The orthogonal flux assumptions for the cylindrical core in two directions are reviewed. The flux penetration between two adjacent blocks is considered and explained. The mathematical core loss model is created for a cylindrical core composing by ten blocks. Three tests were performed using the developed core loss model. The results visualize the power loss from the core by its temperature distribution, and consequently prove the validity of the developed core loss model. An eddy current loss comparison and the discussion are made between the previous method and the developed method. Overall, the results confirm a significant improvement using the developed core loss model, and a generic form of the partial core can be used for designing future models of partial core transformers which have a stacking factor greater than 0.96.

Acknowledgements

While writing the last part of this thesis, it reminds me about a lot of feelings from my two years and seven months of postgraduate life. Confusion, questions, stress, emotion, constancy, efforts, surprise, and happiness, they are all around me during my studies, but, peace is what I can only feel after completing this thesis. It is a process, a story, a milestone in my life!

I would like to give the most sincerely appreciation to my supervisor Professor Pat Bodger. With your encouragement, there is no fear; with your support, there is no looking back; with your guidance, my eyes become brighter; with your advice, my mind becomes clearer. Learning from you is the part that I enjoyed the most in my postgraduate studies.

I would like to thank my lovely beloved parents for their very long-term mental and financial support. The love and the supports that both of you have given to me, I can never pay off. Without you two, I can not go this far today. I would also like to thank Ken Smart for his help and advice in machines lab (that keeps me still alive), Jac Woudberg for his help in the workshop, David Healy for building the billets, and Pieter Kikstra for computer maintenance.

Finally, special thanks to my friends who spent many years in university with me, thank you for all the discussions, questions, and supports; Bing Wu, Rui Lin, Jeff Wei, William Liu, Wei Bo Li, Ming Yuan Ma, Yin Jia Peng, Jit Sham, Simon Bell, Andrew Lapthorn, Vijay Bendre, Huan Zhang, Wang Yuan, Helen Zhang, Maggie Wang, Hunter Han, Ian Gough, and all my mates in C4 basketball team, thank you all.

Contents

List of Figures

List of Tables

0

Chapter 1

INTRODUCTION

1.1 General Overview

As a compromise between a conventional full-core and a coreless transformer, partial core transformers have been designed, developed and built at the University of Canterbury since 2002 (Bendre et al., 2008). A partial core transformer has laminated ferromagnetic material in the centre, with the primary and secondary windings wound around it. Having no limbs and yokes can make the partial core transformer a cheaper substitute of the full core transformer. As it is smaller and lighter, it is also easier to transport.

As resonant transformers, partial core transformers have been used for high-voltage testing of hydro-generator stators in New Zealand (Bodger & Enright, 2004; Enright & Bodger, 2004). A further development is to build a partial core transformer as a power transformer. In achieving this, consideration needs to be given to the losses in the windings and core. To improve the efficiency of the partial core transformer, the winding losses can be reduced by using superconducting tape and immersing them in a liquid (Bodger et al., 2002a). A reduction in core losses is also desirable.

The core loss consists of two components: hysteresis and eddy current losses. Hysteresis loss is an energy loss caused by reversing the magnetic field in the core as the AC magnetization rises and falls. Eddy current loss is a result of current flows circulating in the core, which is caused by the emf induced from the magnetizing flux. Using the core loss equations of a full core transformer to calculate the power loss for a partial core transformer is inaccurate. As no appropriate core loss equations have been created for the

partial core, the next technical step is to develop a model to calculate the core losses for the partial core transformer.

1.2 Thesis objectives

The major thesis objective was to develop a mathematical model for partial core transformer core loss calculation. Also, a visualization of the core loss for partial core transformers was developed and represented by the temperature distribution in the core.

In order to achieve the main objectives, the equations for eddy current resistance and power loss were developed and confirmed by experiments for uniform flux conditions. The core loss model was built and tested on cubical partial core transformers, then proved on cylindrical partial core transformers. A generic configuration form has been created which can be applied to partial core power transformer construction and loss calculation.

1.3 Thesis outline

Chapter 2 introduces the conventional full-core transformer and its design methodology. As an alternative design, the advantages and disadvantages of a partial core transformer are also described.

Chapter 3 gives an explanation of eddy currents and skin effect. Because of the complexity of the flux flows in a partial-core transformer, a new flux perspective through three directions is created for a single block. The derivations of eddy current resistance and power losses in different directions are developed under uniform flux conditions. Two algorithms are compared with experimental results that support the validity of the eddy current power loss derivation.

Chapter 4 introduces two experimental apparatus and explains the theory behind the experimental circuit. The power losses in two cubical billets with different orientations are compared and there flux patterns are simulated and displayed. The experimental results from the two sets of apparatus are then presented. The error bands from two measuring instruments are compared. The closeness between the results from the developed theory

and experiments, presented using a scale factor, is discussed and confirmed.

Chapter 5 reviews the flux conditions for a cubical core. Three key factors (L', K_{ec} and β_a) are introduced into the eddy current power loss model which builds up the relationships between the eddy current loss and the physical characteristics of the partial core transformer. L' is a length which indicates the region of the flux spreading at the ends of the core. K_{ec} as a ratio indicates how much of the main flux spreads at the ends of the core. β_a is the ratio of the winding axial length to winding thickness. Side views of the flux out of the partial core in two orthogonal angles are displayed using a finite element modelling program. Eddy current resistance and eddy current power loss models are then built up in equation form. The relationships amongst the three key factors are discussed.

Chapter 6 gives a comparison of the geometries of a cubical and a cylindrical core. Assumptions about the flux spreading from the ends of the cylindrical core are made based on the assumptions of the flux from a cubical core as described in Chapter 5. The flux flow between two adjacent blocks is explained. A mathematical core loss model is created for a cylindrical core composed of ten blocks. The developed core loss model is used to calculate the core loss for three different partial core transformers. The core loss from the third test is also visualized through the temperature distribution in the core, which confirmed the validity of the developed core loss model. An eddy current loss comparison and discussion are made between the conventional method and the developed method. A generic form of the partial-core transformer core design has been created for a stacking factor greater than 0.96.

Chapter 7 discusses possible directions for future research and development.

Chapter 8 presents the main conclusions of this thesis.

Chapter 2

BACKGROUND

2.1 Full Core Transformer History

Transformers have been widely used and developed for different purposes, such as auto-transformers, power transformers, audio transformers, multi-phase transformers, instrument transformers, current transformers, Radio Frequency (RF) transformers, isolating transformers and resonant transformers (Harlow, 2007).

By sharing a common flux through an iron core, a transformer is a device magnetically coupling two circuits together and transferring the electric energy from one circuit to another, under alternating current (AC) conditions. Its operation is based on the principle of induction, which was discovered by Faraday in 1831 (Liew, 2001). The first practical full core transformer was created by Hungarian engineers Károly Zipernowsky, Ottó Bláthy and Miksa Déri in 1885 and named a "Z.B.D." transformer (Del Vecchio et al., 2002). Their device had a closed toroidal core made of iron wire. It was first used to supply electric lighting.

Skin depth is a measure of the depth that an alternating current can penetrate beneath the surface of a conductor. The transformer core is normally composed of a stack of steel laminations. The thickness of a lamination is normally less than twice the skin depth (Liew et al., 2001), to allow a uniform flux density. Laminations are electrically insulated from each other, which limits the power loss caused by eddy currents in the core.

Heat is produced in the core and windings during transformer operation. The generated

heat must be removed to prevent overheating that can cause breakdown of winding insulation. There are four typical cooling systems, as listed in **Table 2.1**.

	O (oil)	A (air)
N (natural)	ON (oil-natural) For small transformers	AN (air-natural) For small transformers
F (forced)	OF (oil-forced) For large transformers	AF (air-forced) For medium sized transformers

Table 2.1: Four typical cooling systems.

With a high breakdown strength, oil is normally used as the insulation material between a transformer's windings and its tank (Liew, 2001). For natural cooling, the heat is passed to the oil which circulates around the tank and external radiators by natural convection. For forced cooling, fans are applied to accelerate the air flowing through the radiators of the transformer, thus increasing the rate of heat dissipation by convection. Cold water may also be passed through pipes immersed in the oil to remove the heat.

2.2 Ideal transformer

A profile of a single phase full core transformer is shown in **Figure 2.1** (Harlow, 2007). The core links one electrical circuit connected to its primary winding to another electrical circuit connected to its secondary winding.

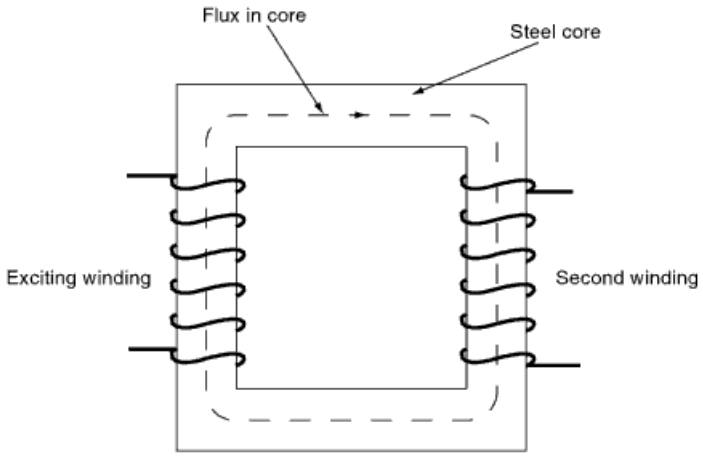

Figure 2.1: Single phase full core transformer (Harlow, 2007).

With an ideal transformer, the power transferred between the electric circuits is unchanged. There are no losses. The equivalent circuit for an ideal transformer is shown in **Figure**

2.2 (Bell, 2008). The two windings and the core are shown symbolically.

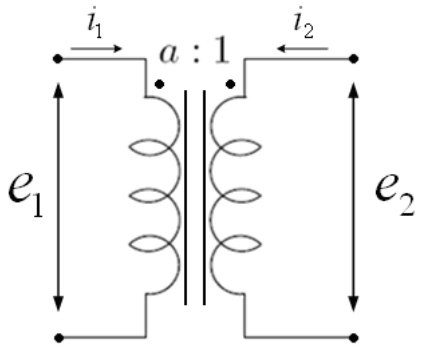

Figure 2.2: Ideal transformer equivalent circuit(Bell, 2008).

In **Figure 2.2**

e_1 is the induced electromotive force (emf) of the primary winding

e_2 is the induced emf of the secondary winding

i_1 is the primary current

i_2 is the secondary current

a is the turns ratio ($\frac{N_1}{N_2}$)

N_1 is the number of turns on the primary

N_2 is the number of turns on the secondary

A changing magnetic flux (ϕ) induces the electromotive forces (emfs) in the circuit. This is proportional to the number of turns linked by the changing flux. Thus the ratio of the emfs is:

$$\frac{e_1}{e_2} = \frac{N_1}{N_2} \tag{2.1}$$

Faraday's law states that the magnitude of an emf is proportional to the rate of change of flux linkage (λ), which in turn depends on the number of winding turns N as

$$\lambda = N \cdot \phi \tag{2.2}$$

Thus

$$e_1 = \frac{d\lambda_1}{dt} = N_1 \cdot \frac{d\phi}{dt} \tag{2.3}$$

and

$$e_2 = N_2 \cdot \frac{d\phi}{dt} \tag{2.4}$$

In general, the flux changes with sinusoidal excitation as

$$\phi = \phi_{max} \sin \omega t \tag{2.5}$$

where $\omega = 2\pi f$, and f is the frequency in Hz. The induced voltage e_1 is

$$e_1 = \omega N_1 \phi_{max} \cos \omega t \tag{2.6}$$

The Root Mean Square (RMS) value of the induced voltage, E is expressed as

$$E = \frac{\omega N_1 \phi_{max}}{\sqrt{2}} = 4.44 f N_1 \phi_{max} \tag{2.7}$$

2.3 Equivalent Circuit and Losses

For non-ideal transformers, the most common representation is the Steinmetz transformer equivalent circuit, as shown as **Figure 2.3** (Paul et al., 1986).

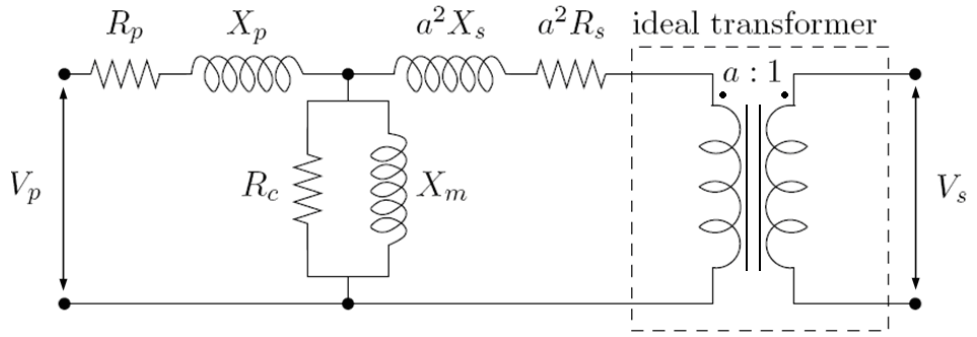

Figure 2.3: The Steinmetz transformer equivalent circuit referred to the primary(Paul et al., 1986).

where

V_p is the primary voltage

V_s is the secondary voltage

R_p is the primary winding resistance

X_p is the primary leakage reactance

X_s is the secondary leakage reactance

R_s is the secondary winding resistance

R_c is the core loss resistance

X_m is the magnetising reactance

For a transformer, the total losses are generally separated into two types, which are load dependent and load independent. The losses produced from both the primary and secondary windings are load dependent losses, which increase when the load current rises. The losses which are independent of the load are the core losses. These are the sum of the hysteresis loss and eddy current losses. They are voltage dependent and hence essentially constant for any constant supply voltages.

2.3.1 Winding Loss

Two components determine the winding loss P_w, which are the winding current I and the winding resistance R. The winding loss is

$$P_w = I^2 R \tag{2.8}$$

The variation of winding current corresponds to the load. A winding resistance depends on the conductor resistivity and its dimensions

$$R = \rho \frac{l_w}{A_w} \tag{2.9}$$

where

ρ is the resistivity of the conductor

l_w is the conductor length

A_w is the cross sectional area of the conductor

The conductor resistivity changes with temperature according to (Davies, 1990)

$$\rho = (1 + \triangle \rho(T - T_0)) \cdot \rho_{20^\circ C} \tag{2.10}$$

where

$\rho_{20^\circ C}$ is the electrical resistivity of the material at 20˚C

T is the operating temperature

T_0 is the reference temperature (20˚C)

$\triangle \rho$ is the thermal resistivity coefficient.

The transformer windings are usually made of copper or aluminium conductor with a low resistivity.

2.3.2 Core loss

The core losses are a combination of eddy current and hysteresis losses. **Figure 2.4** shows the core loss components incorporated into the equivalent circuit in parallel with the magnetising reactance (Paul et al., 1986).

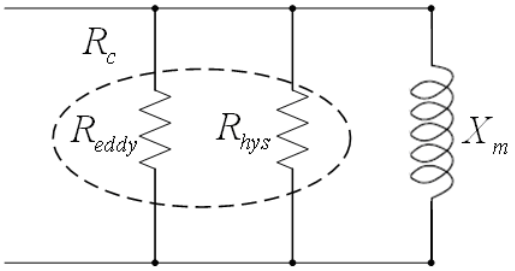

Figure 2.4: Equivalent circuit for the core.

The hysteresis loss is expressed as (Slemon, 1966; Heathcote, 2007)

$$P_{hys} = k_h \cdot f \cdot B_c^x \cdot WT_c \tag{2.11}$$

where

k_h is a constant that depends on the material

B_c is the maximum flux density

x is the Steinmetz factor (between 1.8 and 2.5)

The eddy current loss can be calculated using (Slemon, 1966; Heathcote, 2007)

$$P_{ec} = \frac{c_1^2}{12\rho_c} \cdot \frac{l_c}{N_1^2 \cdot A_c} \cdot e_1^2 \tag{2.12}$$

where

c_1 is the lamination thickness

ρ_c is the core resistivity

l_c is the core flux path length

A_c is the cross sectional area of the core

e_1 is the induced primary winding emf

Based on the expressions of the hysteresis and eddy current losses, with minor modifications, accurate prediction of the core losses has been achieved for a single phase conventional shell core transformer (Sippola & Sepponen, 2002). Another method of (toroidal) core loss prediction has been developed using a feed forward neural network and genetic algorithm. The results give good agreement between calculated and measured values (Kucuk & Derebasi., 2006).

2.4 Regulation and Efficiency

For a given primary winding voltage, the secondary output voltage is at its highest when there is no load applied to the secondary terminals. For all resistive and inductive loads, when a load is applied to the transformer, there is a voltage drop due to the resistance and the leakage reactance of the primary winding, and a voltage drop across similar parameters of the secondary winding. This gives rise to a reduction in the secondary output voltage. However, the output voltage can exceed the no-load voltage when there is a certain level of capacitive load applied to the transformer.

Regulation defines the change in the output voltage that occurs when the load on the transformer is increased from the no-load level to the rated full-load level, while the input voltage is held constant. It is typically expressed as (Harlow, 2007)

$$Voltage\,regulation\,(\%) = \frac{V_{2\_NL} - V_{2\_FL}}{V_{2\_FL}} \times 100\% \tag{2.13}$$

where

V_{2_NL} is the output voltage at no-load

V_{2_FL} is the output voltage at full-load

The efficiency of a transformer is determined as the output real power over the input real power. Since the input real power is always greater than the output real power because of the losses, the transformer efficiency is determined as (Harlow, 2007):

$$Efficiency\,(\%) = [kW\,rating/(kW\,rating + total\,losses] \times 100\% \tag{2.14}$$

The total losses are the sum of the winding losses and the core losses.

2.5 Partial Core Transformer

In between the design of a single phase transformer, with either a full core or an air core, one of the developments has been to make a transformer without the limbs and yokes of the full core model, but retaining the core material inside the windings. This has been named the partial core transformer shown in **Figure 2.5**. The partial core transformer has been successfully developed at the University of Canterbury (UoC) since about the year 2000. Also, without guessing the values of space factors (SF1 and SF2) and window width factor (WWF), as required in conventional modelling of transformers, a reverse design transformer method (Bodger & Liew, 2001) has been developed. This has been applied to partial core transformers (Liew & Bodger, 2001).

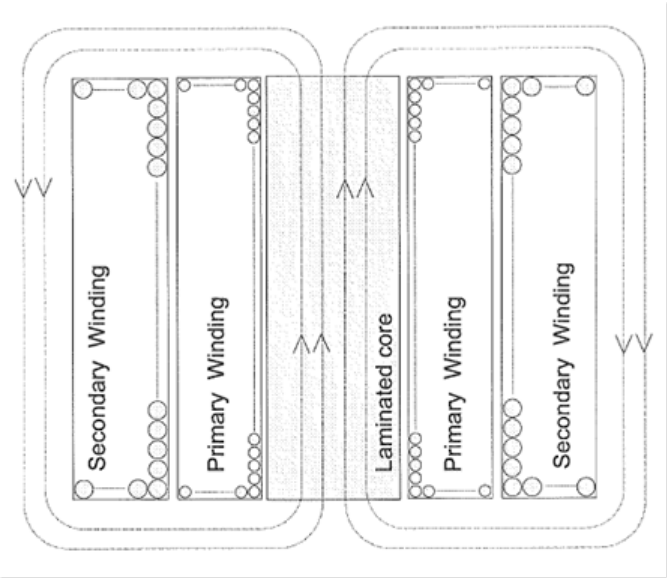

Figure 2.5: Cross sectional view of a partial core transformer(Liew & Bodger, 2001).

The prime purpose for the partial core transformer design at the UoC was to combine an exciter transformer and a tuneable inductor together into a single unit for testing the stator winding insulation at hydro generators in New Zealand power stations (Bodger & Enright, 2004).

The partial core transformer, without yokes and limbs, has a significantly reduced weight compared to a conventional exciter/transformer combination. It also saves on a number of the inductive compensation components (including two transformers and three inductors)

that were previously used, as shown in **Figure 2.6** (Enright & Bodger, 2004). From an environmental point of view, there is no insulation oil. An alternative use of a partial core transformer may be as a power transformer.

Figure 2.6: Manapouri resonant partial core transformer in front of the equipment previously used for generator stator testing at Tekapo power station(Enright & Bodger, 2004).

One of the trade-offs for a partial core transformer as a single phase power transformer is its lower efficiency (about 90% at room temperature) compared with a full core transformer (better than 95% at room temperature (Kubo & Nadel, 2001)). To improve the efficiency, the total losses from the partial core transformer must be reduced.

With the intention of reducing the load dependent losses of a partial core transformer, cryogenic immersion of the entire unit into liquid nitrogen has been investigated (Bodger et al., 2005, 2002a; O'Neill et al., 2000). The winding loss was significantly reduced and the efficiency improved, with a low voltage regulation.

For the load independent losses, the existing core loss models for partial core transformers are known to be inaccurate. In particular, the eddy current loss calculation has been in error. This lack of an accurate core loss model has been a difficulty in the design of a power transformer using a partial core. Therefore, as one of the major objectives of this thesis, a new partial core power loss prediction model has been developed.

Chapter 3

NEW METHOD FOR EDDY CURRENT LOSS COMPUTATION

3.1 Introduction

An eddy current is generated by the induced emf from the flux which is created by an external excitation source. Because of the complexity of the flux flows for a partial-core transformer, a new flux direction perspective is needed. Based on this new perspective, derivations of the eddy current resistance and power losses in different directions are developed using uniform flux conditions. Experimental measurements of eddy current loss are also introduced. Two algorithms are compared with experimental results that support the validity of the eddy current power loss derivation.

3.2 Background

3.2.1 Eddy Current

For a transformer under normal operating conditions, the primary winding is energized by an alternating current source. A fluctuating magnetic field is produced. An eddy current is induced inside a metal by the varying magnetic field inside the material. This eddy current creates an internal magnetic field opposing the excitation magnetic field. This gives rise to skin effect in which the current density near the outside of the conductor is greater than the inside. Hence the eddy current flows in a ring around the outside of the conducting material. **Figure 3.1** indicates the eddy current flow in a block when there is

an external flux passing through it. While the eddy current is depicted as a number of circulating loops in the figure, in actuality, the eddy current is evenly distributed over the entire length of the metal in the direction of the flux.

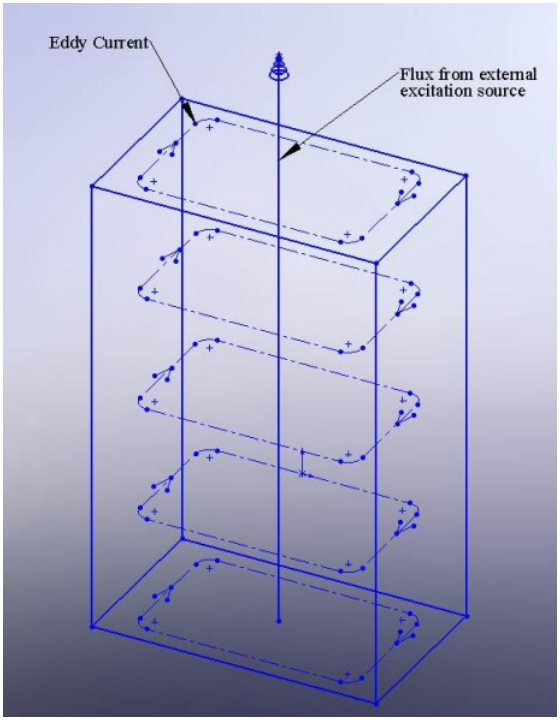

Figure 3.1: Eddy currents inside a metal block.

The eddy current creates a power and hence an energy loss in the metal. In order to reduce the eddy current loss and improve the transformer efficiency, the transformer core is usually laminated. Due to the thin, insulated laminations, the cross-sectional area of the eddy current path is reduced. Hence the resistance of the eddy current pathway is increased and the losses reduced.

3.2.2 Flux Direction Perspective

A partial-core transformer has no yokes and limbs. Existing models of a partial core transformer assume that the flux passes uniformly through the core. At the end of the core, the flux spreads out as shown in **Figure 3.2**(Liew, 2001). However, in reality, the flux is not uniform in the core, but spreads out such that there are radial components of flux through the core laminations. In this case, the eddy current power loss analysis is complicated. In order to generate simple quantitative expressions for the eddy current loss, the flux in a partial core in any rectangular lamination can be represented in three orthogonal directions as shown in **Figure 3.3**.

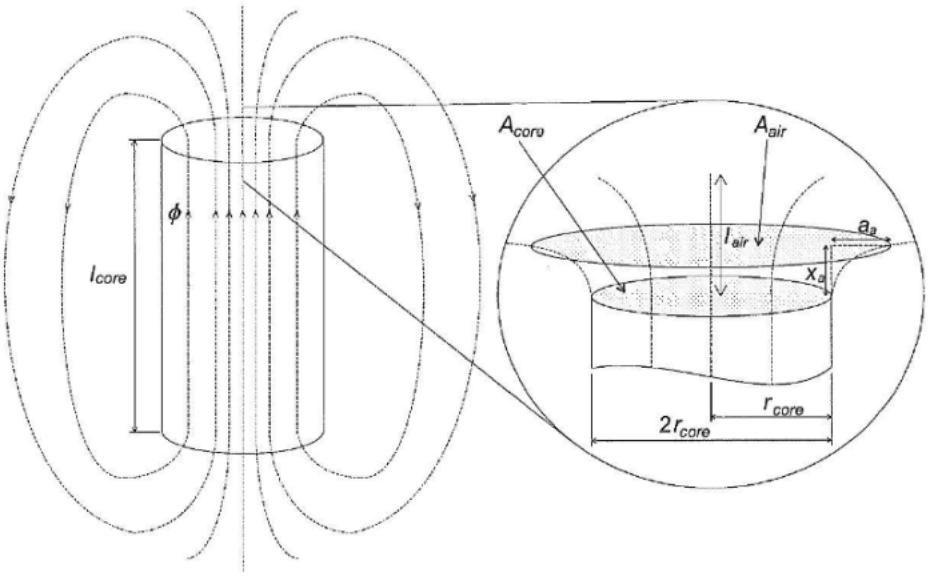

Figure 3.2: Flux view of the partial core(Liew, 2001).

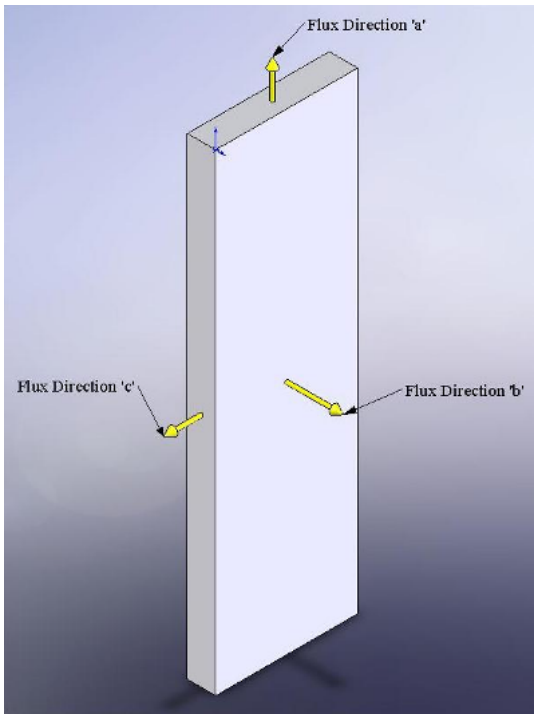

Figure 3.3: Three directions of flux in single lamination.

3.3 Eddy Current Resistance in Each Direction

Since the flux is considered as going in three directions, the eddy current resistance in the three directions can be derived by using the conventional resistance formula:

$$R = \rho \cdot \frac{l}{A} \tag{3.1}$$

where ρ is the resistivity of the conductor, l is the average length of the eddy current pathway and A is the cross sectional area of the eddy current pathway.

3.3.1 In Direction 'a'

In order to get a uniform flux density in direction **'a'**, the thickness of the lamination (T_{core}) is usually thinner than twice the skin depth δ (Liew et al., 2001). **Figure 3.4** displays the eddy current path when the flux comes through the direction **'a'**.

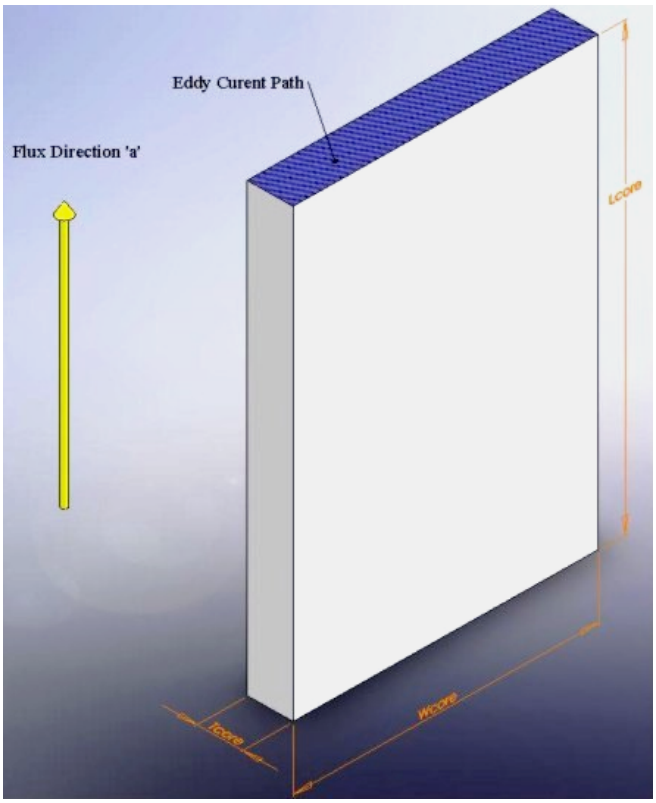

(a) Side view of the lamination

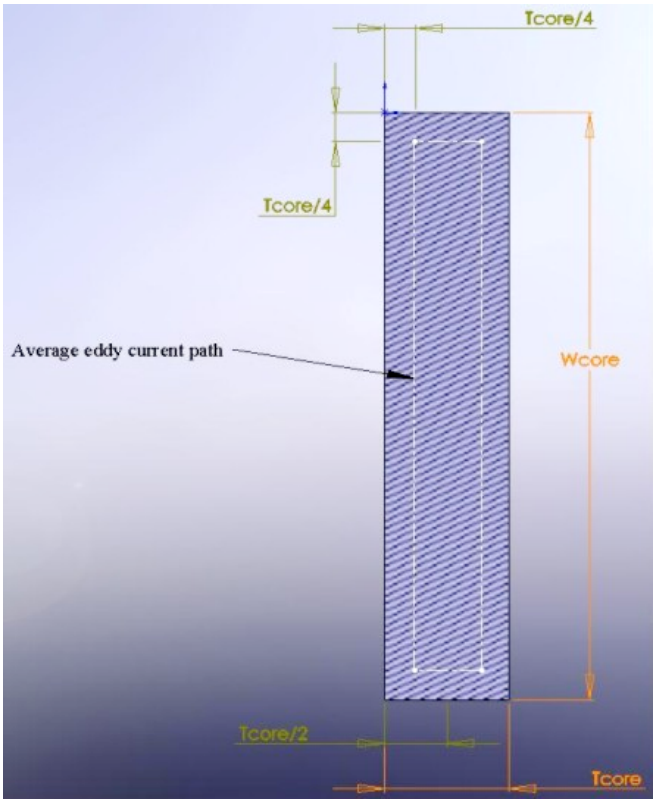

(b) Top view of the lamination

Figure 3.4: Eddy current pathway in direction **'a'**.

From **Figure 3.4**, the average length of the eddy current pathway is $2(W_{core} - {}^{T_{core}}/_{4} \times 2) + {}^{T_{core}}/_{2} \times 2$, and the cross sectional area of the eddy current pathway is $l_{core} \times {}^{T_{core}}/_{2}$. Where

ρ_{core} is the resistivity of the core material, W_{core} is the width, l_{core} is the length, and T_{core} is the thickness of the single lamination.Applying **Eq:3.1**, the eddy current resistance in direction **'a'** is

$$R_{ec_a} = \rho_{core} \cdot \frac{2(W_{core} - \frac{T_{core}}{4} \times 2) + \frac{T_{core}}{2} \times 2}{l_{core} \times \frac{T_{core}}{2}} = \rho_{core} \cdot \frac{4W_{core}}{l_{core} \times T_{core}} \tag{3.2}$$

3.3.2 In Direction 'b'

The eddy current path for when the flux comes through direction **'b'** is shown in **Figure 3.5**. In this case, the width of the eddy current path is one skin depth (δ) and the eddy current flows around the edge of the lamination.

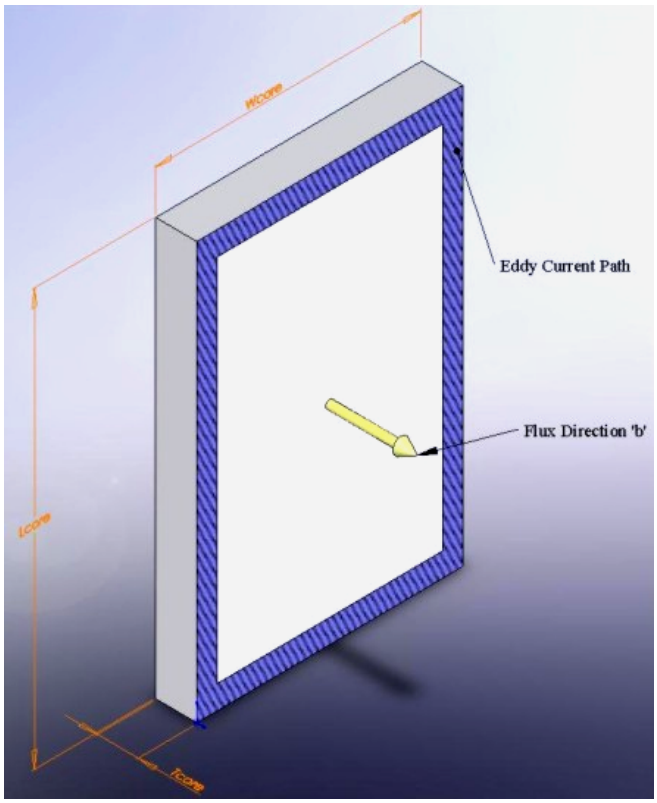

(a) Side view of the lamination

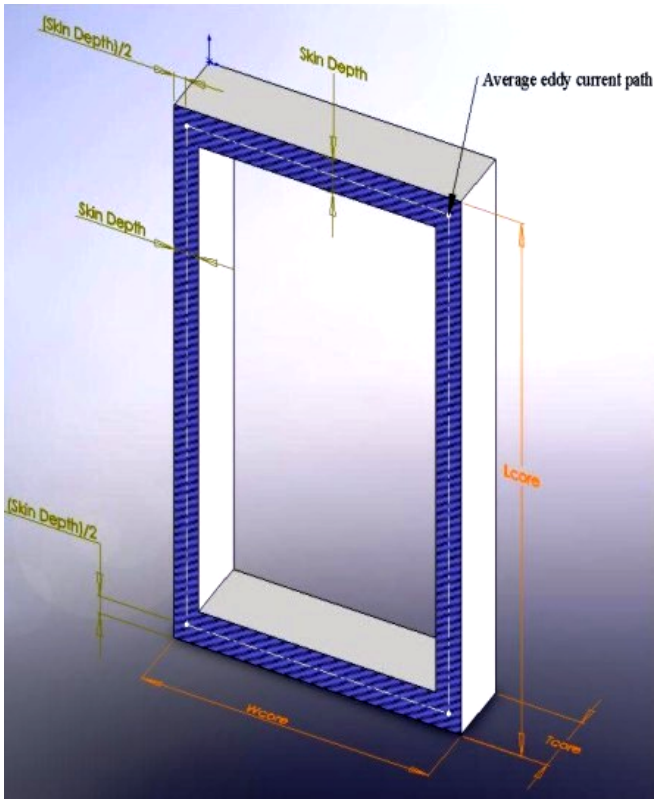

(b) Perspective drawing of eddy current pathway

Figure 3.5: Eddy current pathway in direction **'b'**.

From **Figure 3.5**, the dotted line shows the average eddy current pathway. Its length is $2(W_{core} - {}^{\delta}/_{2} \times 2) + 2(l_{core} - {}^{\delta}/_{2} \times 2)$. The cross sectional area of the eddy current pathway

is $\delta \times T_{core}$. Applying **Eq:3.1**, the eddy current resistance in direction **'b'** is

$$R_{ec_b} = \rho_{core} \cdot \frac{2(W_{core} - \frac{\delta}{2} \times 2) + 2(l_{core} - \frac{\delta}{2} \times 2)}{\delta \times T_{core}} = \rho_{core} \cdot \frac{2W_{core} + 2l_{core} - 4\delta}{\delta \times T_{core}} \quad (3.3)$$

3.3.3 In Direction 'c'

In direction **'c'**, the eddy current path is similar to that for direction **'a'**, where the thickness of the lamination (T_{core}) is thinner than twice the skin depth (δ). **Figure 3.6** shows the eddy current path when the flux comes through direction **'c'**.

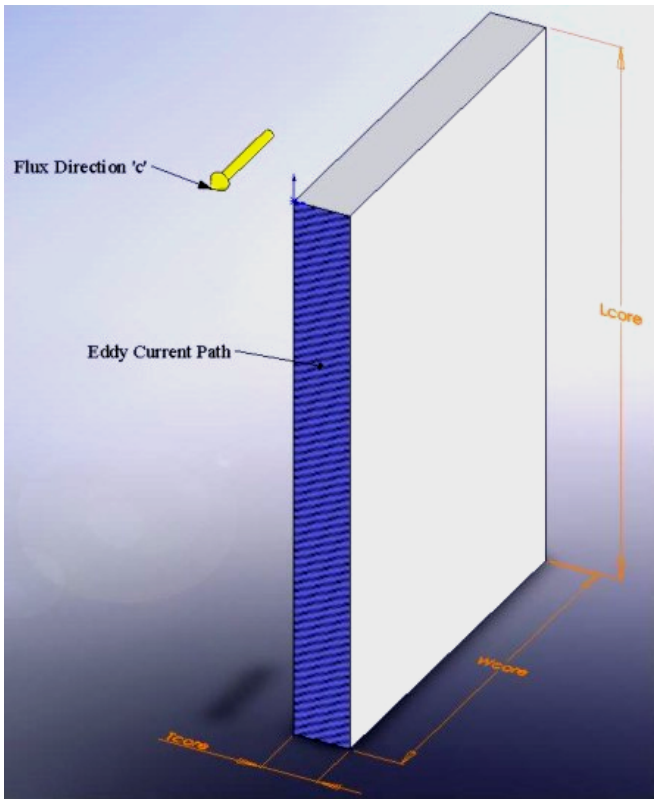

(a) Side view of the lamination

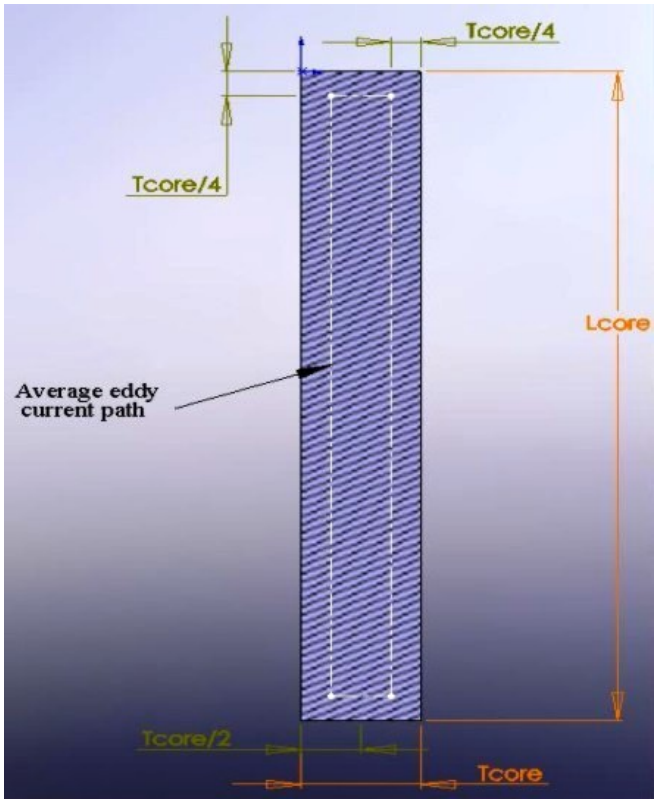

(b) Orthogonal view of the lamination side

Figure 3.6: Eddy current pathway in direction **'c'**.

From **Figure 3.6**, the dotted line indicates the average eddy current pathway which has a length of $2(l_{core} - {}^{T_{core}}/_{4} \times 2) + 2(T_{core} - {}^{T_{core}}/_{4} \times 2)$. The cross sectional area of the

eddy current pathway is $W_{core} \times {}^{T_{core}}/_{2}$. Applying **Eq:3.1**, the eddy current resistance in direction **'c'** is

$$R_{ec_c} = \rho_{core} \cdot \frac{2(l_{core} - \frac{T_{core}}{4} \times 2) + 2(T_{core} - \frac{T_{core}}{4} \times 2)}{W_{core} \times \frac{T_{core}}{2}} = \rho_{core} \cdot \frac{4l_{core}}{W_{core} \times T_{core}} \quad (3.4)$$

3.4 Eddy Current Power Loss under a Uniform Flux Condition

In general, the eddy current power loss can be derived by using the formula:

$$P = \frac{V^2}{R} \quad (3.5)$$

where V is the voltage induced in each lamination and R is the eddy current resistance.

3.4.1 In Direction 'a'

A simple model of the flux distribution in two laminations in direction **'a'** is shown in **Figure 3.7**. Since $\delta \geq {}^{T_{core}}/_{2}$, the uniform flux passing through each piece of lamination is the same. If there are n_{lam} laminations, then the uniform flux passing through each lamination in direction **'a'** is $\frac{\phi_{total\_a}}{n_{lam}}$. Since is the voltage ($e$) induced in the core referred to the primary proportional to the flux, and the number of primary winding turns (N_1), the voltage on each lamination through direction **'a'** is $\frac{e}{N_1 \cdot n_{lam}}$.

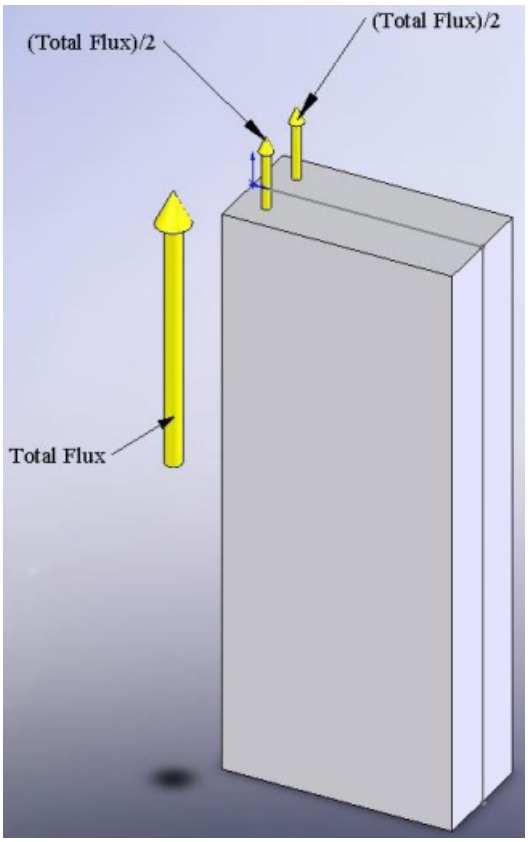

Figure 3.7: Model of flux distribution in two laminations in direction **'a'**.

By applying the **Eq:3.5**, the eddy current power loss in direction 'a' for n_{lam} laminations is

$$P_{ec_a} = \frac{(\frac{e}{N_1 \cdot n_{lam}})^2}{R_{ec_a}} \cdot n_{lam} \tag{3.6}$$

where R_{ec_a} is the eddy current resistance in direction **'a'** which has been presented in **Eq:3.2.**

3.4.2 In Direction 'b'

A model of the flux distribution in two laminations in direction **'b'** is shown in **Figure 3.8**. Since there are no laminations in direction **'b'**, the uniform flux passing through each rectangular plate is the same. This is ϕ_{total_b}. The flux is proportional to the voltage induced in the core (e) referred to the primary, hence the voltage in each lamination in direction **'b'** is $\frac{e}{N_1}$.

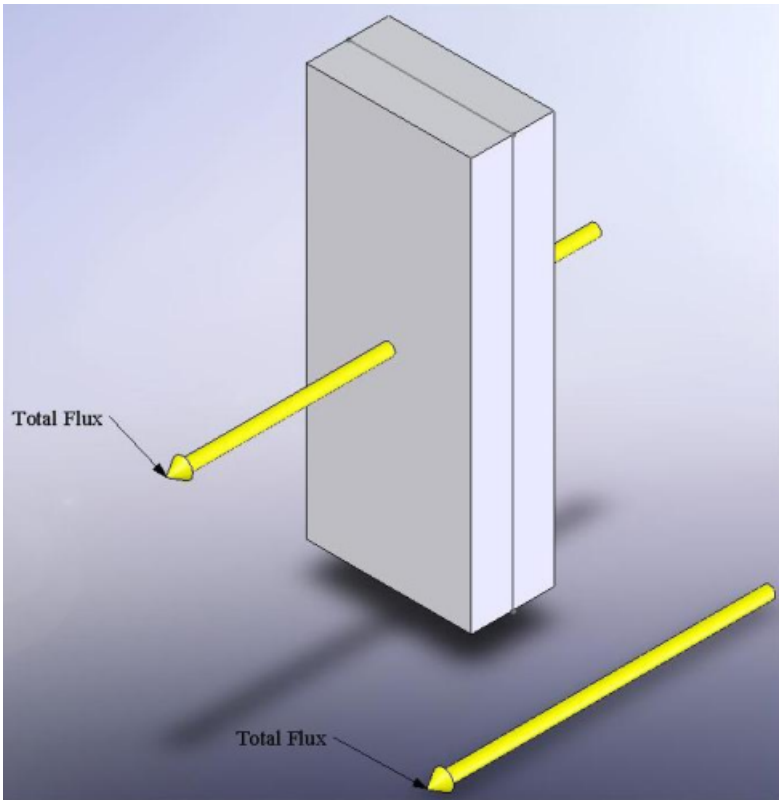

Figure 3.8: Model of flux distribution in two laminations in direction **'b'**.

The eddy current power loss in direction **'b'** for n_{lam} laminations using **Eq:3.5** is

$$P_{ec_b} = \frac{(\frac{e}{N_1})^2}{R_{ec_b}} \cdot n_{lam} \tag{3.7}$$

where R_{ec_b} is the eddy current resistance in direction **'b'** which has been presented in **Eq:3.3.**

3.4.3 In Direction 'c'

A model of the flux distribution in two laminations in direction **'c'** is shown in **Figure 3.9**. The differences is the models between direction **'c'** and direction **'a'** are only on the flux direction and the length of the eddy current pathway. If there are n_{lam} laminations, the flux passing through each lamination is $\frac{\phi_{total\_c}}{n_{lam}}$. By applying the same theory as for direction **'a'**, the voltage distributed on each lamination in direction **'c'** is $\frac{e}{N_1 \cdot n_{lam}}$.

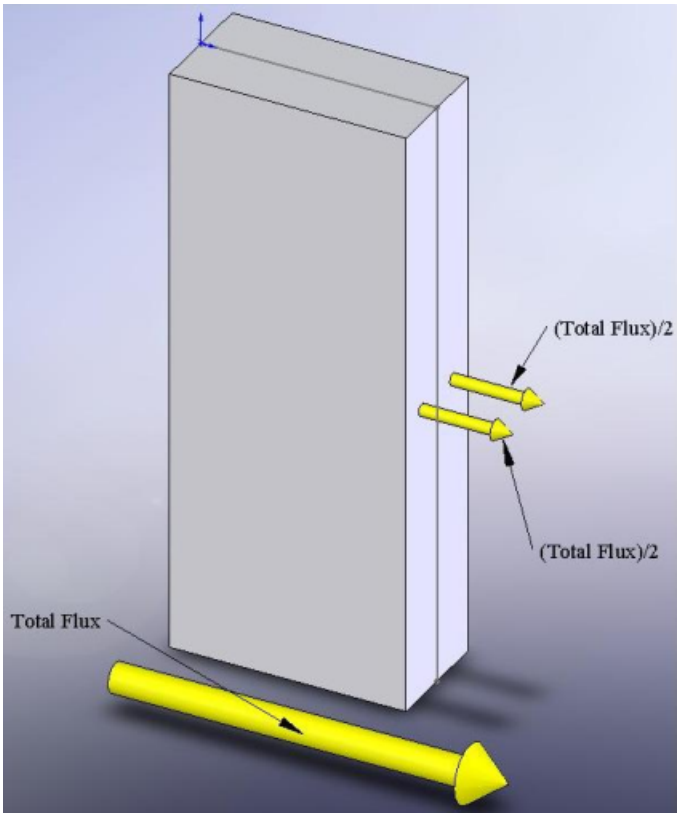

Figure 3.9: Model of flux distribution in two lamiantions in direction **'c'**.

By applying **Eq:3.5**, the eddy current loss in direction **'c'** for n_{lam} laminations can be derived as

$$P_{ec_c} = \frac{(\frac{e}{N_1 \cdot n_{lam}})^2}{R_{ec_c}} \cdot n_{lam} \tag{3.8}$$

where R_{ec_c} is the eddy current resistance in direction **'c'** which has been derived in **Eq:3.4.**

3.5 Experimental Results

In order to prove the validity of the eddy current loss derivation, a magnetic circuit experiment was performed. The purpose of this experiment was to use the uniform flux passing through two rectangular billets with different lamination orientations, to observe the eddy current and hysteresis power losses with each orientation. **Figure 3.10** shows the two rectangular billets with different orientations and **Table 3.1** lists the physical details of each billet.

Billet	**a**	**b**
Length (mm)	115	115
Width (mm)	19.5	30
Height (mm)	30.3	19
Lamination Thickness (mm)	0.3	0.3
Number of Laminations (pieces)	100	65
Weight (g)	480.2	460.2

Table 3.1: Physical dimensions of each billet.

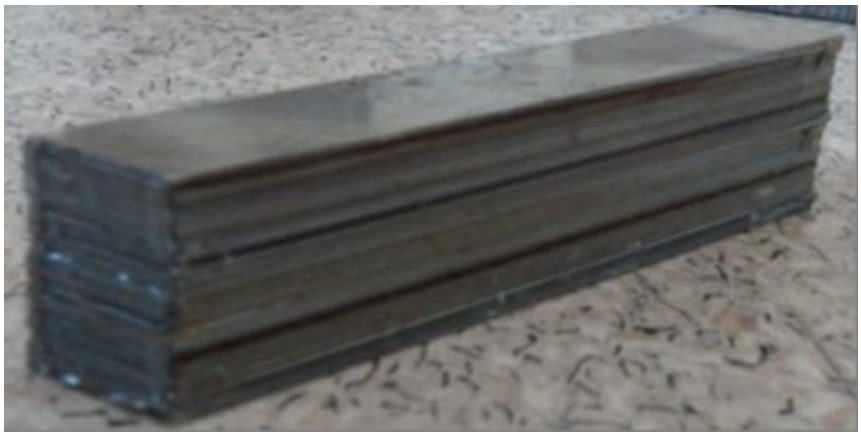

(a) Laminations aligned with main flux

(b) Laminations orthogonal to main flux

Figure 3.10: Two rectangular billets with different lamination orientations.

The C-core uniform flux generator is shown in **Figure 3.11.** This is a form of transverse flux induction heater or trans-heater. There are four windings around the core and each of them has 100 turns. In the experiments, only the two top windings were used in a series connection. During the experiment, input power, input current and input voltage were measured. The results from the experiment are shown in **Table 3.2**. By fitting the different rectangular billets into the gap at the top of the toroidal core, the eddy current

power loss differences for two lamination orientations under different input voltages were calculated.

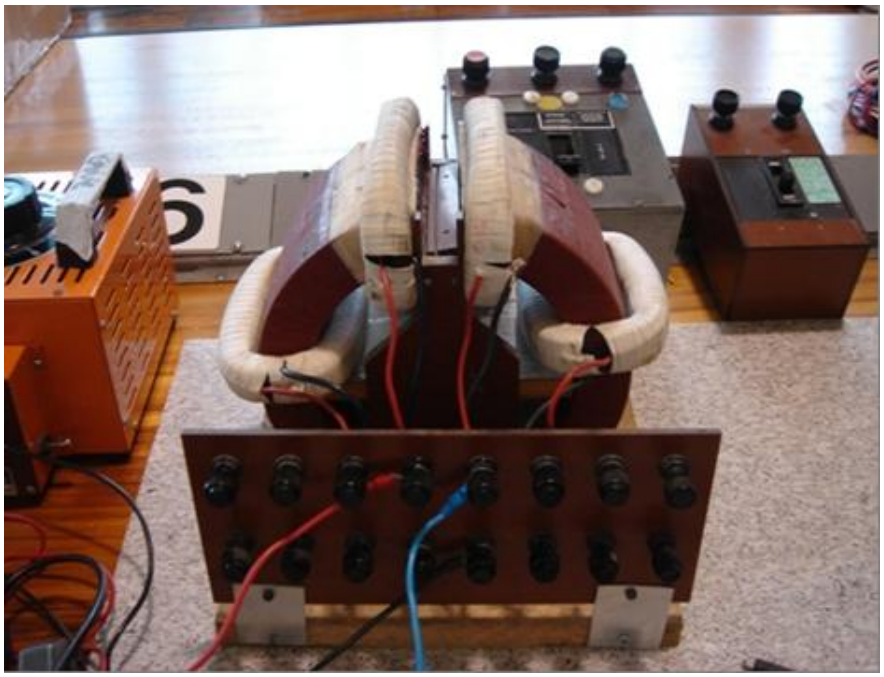

Figure 3.11: Uniform flux generator.

	Input voltage (V)	Input current (A)	Input power (W)
Billet **a**	25	1.37	4
	50	2.72	15
	75	4.09	33
	100	5.48	60
Billet **b**	25	1.51	9
	50	3.01	36.5
	75	4.30	76
	100	5.71	130

Table 3.2: Experimental results from the uniform flux generator.

For any billet, the input power is equal to the sum of the winding loss, hysteresis loss and the eddy current power loss

$$P_{in} = I_{in}^2 \cdot R_w + P_{hys} + P_{ec} \tag{3.9}$$

where P_{in} is the input power, I_{in} is the input current, R_w is the winding resistance, P_{hys}

is the hysteresis loss and P_{ec} is the eddy current power loss.

Since the measured loss also includes the loss in a C-core, a subtraction between the measured power loss from the two billets must be made to calculate the eddy current loss difference. At 25V, the sum of the hysteresis and eddy current losses for Billet **a** (includes C-core loss) was $P_{hys} + P_{ec\_a} = 4W - (1.37A)^2 \cdot 0.79\Omega = 2.52W$. For Billet **b** (includes C-core loss) at 25 V, the sum of the hysteresis and eddy current losses was $P_{hys} + P_{ec\_b} = 9W - (1.52A)^2 \cdot 0.79\Omega = 7.17W$. Therefore, the eddy current loss difference between Billet **a** and **b** at 25V was

$$P_{ec\_b} - P_{ec\_a} = 4.65W$$

By applying the same method, the differences of eddy current loss between Billet **a** and **b** at different input voltages are shown in **Table 3.3**.

V_{in} (V)	$P_{ed\sim b} - P_{ed\sim a}$ (W)
25	4.7
50	20.2
75	41.6
100	68.0

Table 3.3: Eddy currrent loss difference between Billet **a** and **b** at different input voltages.

It can be observed from the results in **Table 3.3** that the eddy current power loss from Billet **b** is more than the eddy current loss from Billet **a**. The thin lamination in Billet **a** reduces the cross-sectional area of the eddy current pathway and consequently increases the eddy current resistance. The voltage induced by the uniform flux in each from Billet **a** was reduced by the number of its laminations, $\frac{e}{n_{lam}}$. However, the induced voltage for Billet **b** was unchanged due to its lamination orientation. Therefore, the different orientations give rise to significant differences in eddy current power loss.

3.6 Theory Identification

In order to prove the concept introduced in this thesis, the eddy current power losses calculated from the formulae of section 3.4 were compared to that proposed by R.M.DEL

and JOHN SEFKO (DEL VECCHIO & SEFKO, 1981).

3.6.1 First Algorithm

Reference (DEL VECCHIO & SEFKO, 1981), introduces the eddy current loss calculation for a thin conducting plate in the presence of a sinusoidal flux directed normal to the lamination plane. The power loss per unit volume is

$$\frac{W}{V} = con \times \frac{f^2 \cdot B_0^2}{\rho} \tag{3.10}$$

where W is the power loss, V is the volume in cm^3, f is the frequency, B_0 is the peak flux density and ρ is the resistivity in units of $\mu\Omega - cm$. The con is a constant given as

$$con = 0.0138 \cdot \frac{a^2 \cdot b^2}{a^2 + b^2} \tag{3.11}$$

where a and b are the length and the width of the core in cm.

In order to assess the validity of **Eq:3.10** using **Eq:3.11**, the results from **Table 3.1**were used. The value of the resistivity and skin depth were not verified, but were assumed to be the same as the parameters of the silicon steel proposed by (Liew et al., 2001), where $\rho = 1.8 \times 10^{-7}\Omega m$ and $\delta = 0.68 \times 10^{-3} m$.

For Billet a

Applying $a = 11.5cm$ and $b = 0.03cm$ to **Eq:3.11**, the factor $con = 1.2 \times 10^{-5}$. The flux density is given as (Paul et al., 1986)

$$B = \frac{V}{4.44 \cdot f \cdot N_1 \cdot A_c} \tag{3.12}$$

where V is the input voltage, f is the frequency, N_1 is the winding turns, and A_c is the cross sectional area. Applying **Eq:3.10** , **Table 3.4** lists the calculated flux density and power loss at different input voltages.

For Billet b

For $a = 11.5cm$ and $b = 3.03cm$, the factor $con = 0.118$. The calculated flux density and power loss for Billet **b** is shown in **Table 3.5**.

Voltage (V)	B_c (T)	Eddy Current Power Loss(W)
25	0.163	2.9×10^{-3}
50	0.326	1.16×10^{-2}
75	0.490	2.62×10^{-2}
100	0.653	4.63×10^{-2}

Table 3.4: Calculated power loss for Billet **a** for different input voltages.

Voltage (V)	B_c (T)	Eddy Current Power Loss (W)
25	0.160	27
50	0.323	108
75	0.485	244
100	0.646	436

Table 3.5: Calculated power loss for Billet **b** for different input voltages.

Because of the uncertainty in the resistivity of the material used in the experiment and the different measuring equipment used in (DEL VECCHIO & SEFKO, 1981), a scale factor was introduced into the verification. At 100V, the difference in the calculated eddy current loss between Billet **a** and **b** was $P_{ec\_b} - P_{ec\_a} = 436 - 4.63 \times 10^{-2} \approx 436W$. The experimental eddy current loss difference was $68W$, hence, the scale factor $sf = \frac{436W}{68W} = 6.4$. Using this scale factor to calculate the eddy current loss at other input voltages, **Figure 3.12** shows a comparison between the experimental results and the calculated values.

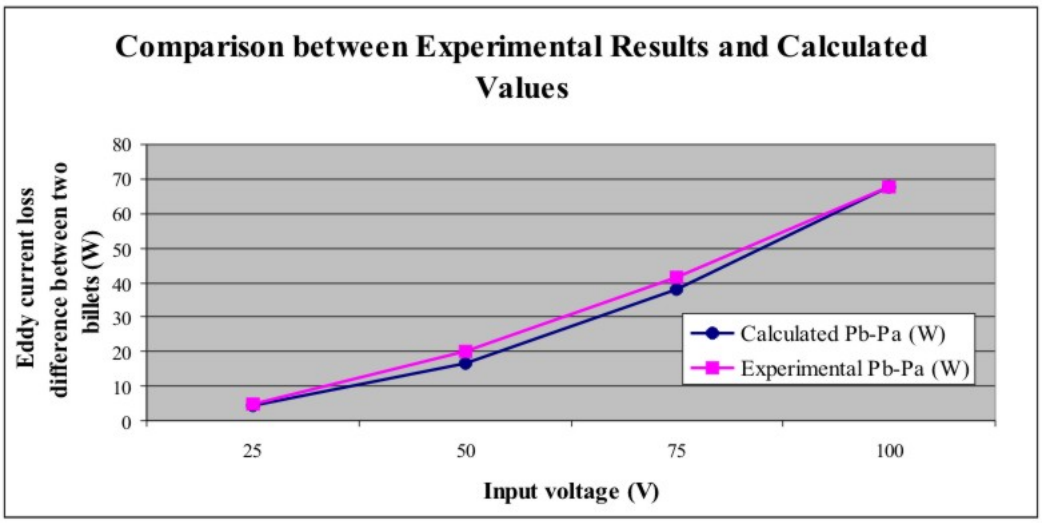

Figure 3.12: Comparison between Experimental results and Calculated values.

The calculated values are fairly close to the experimental results, which confirm the equation proposed by R.M.DEL et al. (DEL VECCHIO & SEFKO, 1981).

3.6.2 Second Algorithm

The second algorithm used the derived method from this chapter.

For Billet a

Applying **Eq:3.4**, the eddy current resistance $R_a = \rho \cdot \frac{4l}{W \cdot T} = 0.0145\Omega$. At 100V, $e = 100V - 5.48A \cdot R_{winding} = 95.6V$. As $N_1 = 200$ and $n_{lam} = 100$, by applying **Eq:3.8**, the eddy current power loss $P_a = 0.16W$. **Table 3.6** lists the induced voltage, eddy current resistance and the eddy current loss for different input voltages.

Voltage (V)	$e\ (V)$	$R_{ec}\ (\Omega)$	$P_a\ (W)$
25	23.9	0.0145	0.01
50	47.9	0.0145	0.04
75	71.8	0.0145	0.09
100	95.6	0.0145	0.16

Table 3.6: Calculated values for Billet **a** for different input voltages.

For Billet b

Following the same procedure, **Table 3.7** shows the calculated values for Billet **b** for different input voltages.

Voltage (V)	$e\ (V)$	$R_{ec}\ (\Omega)$	$P_a\ (W)$
25	23.8	0.254	3.6
50	47.6	0.254	14.5
75	71.6	0.254	32.8
100	95.7	0.254	58.6

Table 3.7: Calculated values for Billet **b** for different input voltages.

The skin depth varies as the inverse square root of the permeability of the conductor. Any differences in the permeability of the conductor can lead to a skin depth variation and change the eddy current resistance. Because of the uncertainty in the permeability of the material used in the experiment, another scale factor was introduced into the verification. At 100V, $P_b - P_a = 58.6 - 0.16 \approx 58.5W$, then the scale factor $sf = \frac{58.5W}{68W} = 0.86$. **Figure 3.13** shows a comparison between the experimental results and the calculated values.

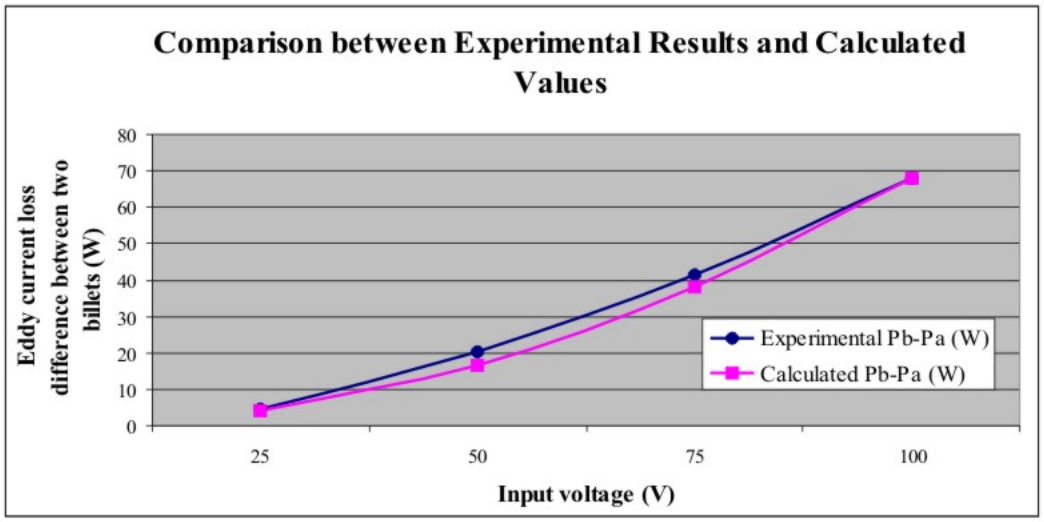

Figure 3.13: Comparison between Experimental and Calculated Values.

The calculated values are close to the experimental results.

3.7 Conclusion

Due to the complexity of the flux distribution in a partial-core transformer, a new perspective of eddy current power loss has been investigated using three orthogonal directions. In order to verify the new perspective, experiments were performed on billets of core material laminated in different directions. The differences in eddy current power loss due to

the different orientations under uniform flux conditions were calculated. The eddy current power loss equations under a uniform flux condition were supported by experimentation. Skin depth variation due to uncertainties in the permeability of the metal, can lead to a different eddy current resistance of the metal; hence, a scale factor was introduced into the model. The scale factor was different for the two algorithms. The improvements in algorithm two compare well to those proposed by R.M.DEL et al. (DEL VECCHIO & SEFKO, 1981).

Chapter 4

FURTHER SUPPORT FOR THE THEORY FOR UNIFORM FLUX CONDITIONS

4.1 Introduction

In this chapter, the theory behind the experimental apparatus and the billets with different orientations are explained. Next, from a current density point of view, a comparison between two cubical billets with different orientations is made. A simulation of the flux patterns of the two billets using Quick Field (Tera Analysis, 2001) is displayed. In order to confirm the validity of the theory developed, two experiments were performed on each of two different uniform flux generator apparatus. The error bands from two measurement instruments are compared, and the scale factor of the developed theory is confirmed.

4.2 Apparatus

4.2.1 Apparatus 1

For the first set of equipment, the arrangement included two billets with different orientated laminations, and a C-core uniform flux generator which was introduced in Chapter 3.

4.2.2 Apparatus 2

The second apparatus has the same configuration as the first but with different dimensions. Both the billets were wrapped with mica tape to hold the laminations together. **Figure 4.1** displays the orientations of the two different billets for the second apparatus. **Table 4.1** shows the weights and geometry of each billet.

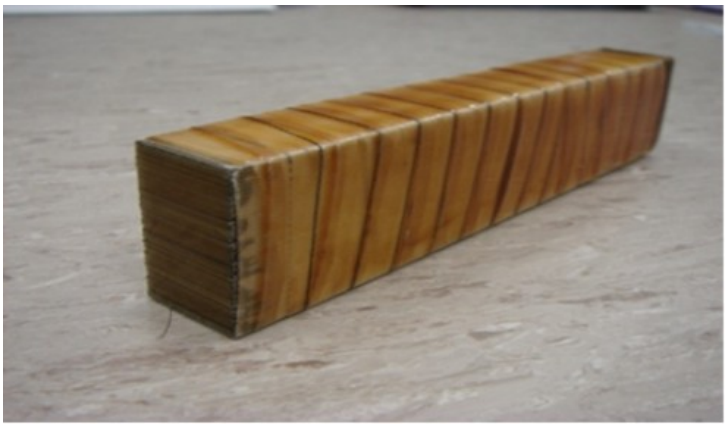

(a) Laminations aligned with main flux

(b) Laminations orthogonal to main flux

Figure 4.1: Two billets of the second apparatus with different orientations.

Billet	**a**	**b**
Length (mm)	150	150
Width (mm)	20	20
Height (mm)	33	33
Lamination Thickness (mm)	0.5	0.5
Number of Laminations (pieces)	66	40
Weight (g)	745.0	746.8

Table 4.1: Geometry and weight for the second set of billets.

Figure 4.2 shows the second C-core uniform flux generator (Dol, 1986). This apparatus

used copper coils wound around the core to reduce the flux leakage. A number of coils were also wound beside the air gap of the core to generate a more uniform flux through the core air gap. The total number of coil turns in series was 400.

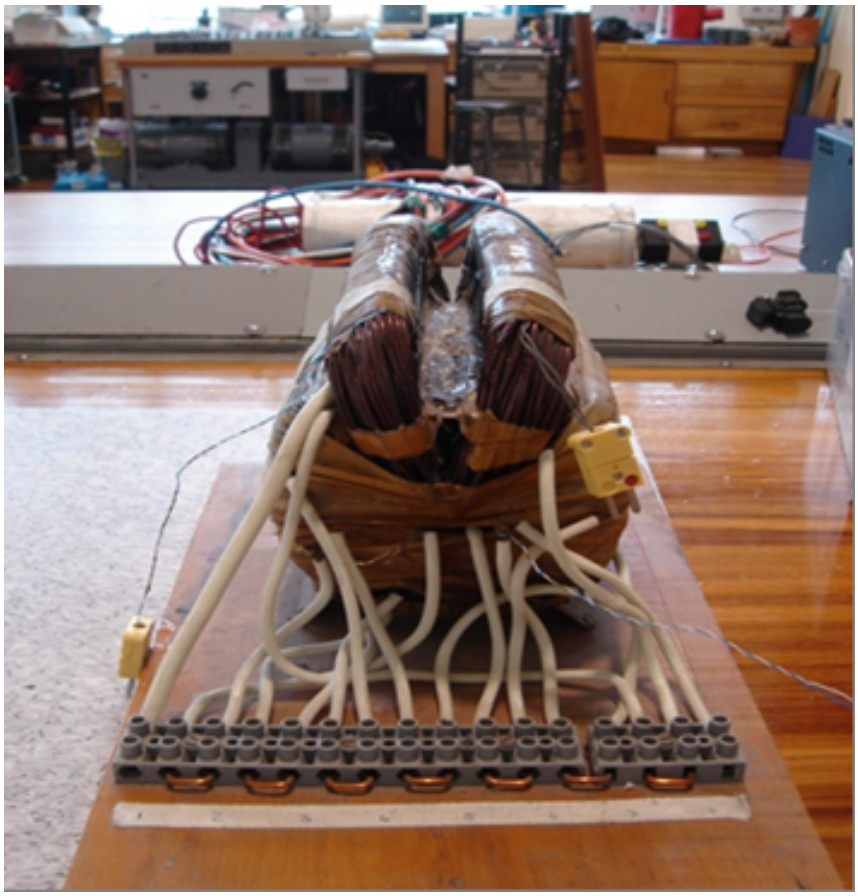

Figure 4.2: The second C-core uniform flux generator.

4.3 Theoretical Background

4.3.1 Model of the experimental apparatus

Both sets of apparatus used in the experiments can be considered as transformers with single turn secondaries, although their initial designs were for use as transverse flux induction heaters. **Figure 4.3** shows the cross sectional view of a generalised C-core uniform flux generator. The billet is placed in the middle of the C-core gap.

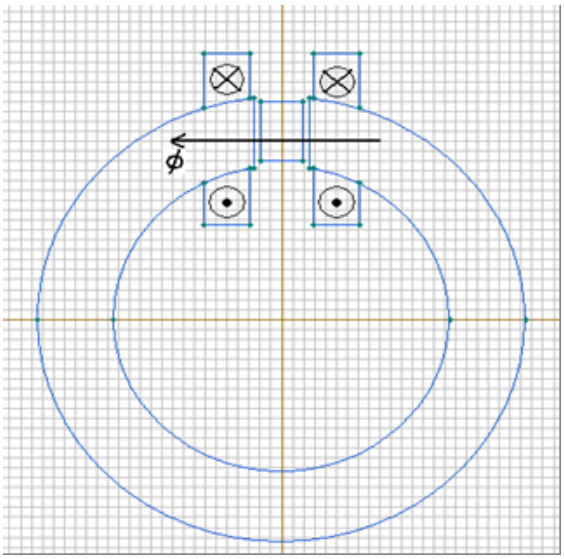

Figure 4.3: Cross sectional view of a C-core uniform flux generator.

As a transformer, the primary windings around the edge of the C-core generate the flux through the billet. The voltage, V_{eddy}, induced from the flux inside the billet, can be considered as the secondary voltage, with the pathway of the eddy current as a one turn winding. The hysteresis and eddy current loss components can be represented independently in a Steinmetz transformer model. Since the research was focused on the eddy current loss, the resistive component of the eddy current loss can be shifted to the secondary side. **Figure 4.4** indicates the equivalent circuit of the apparatus used in the experiments.

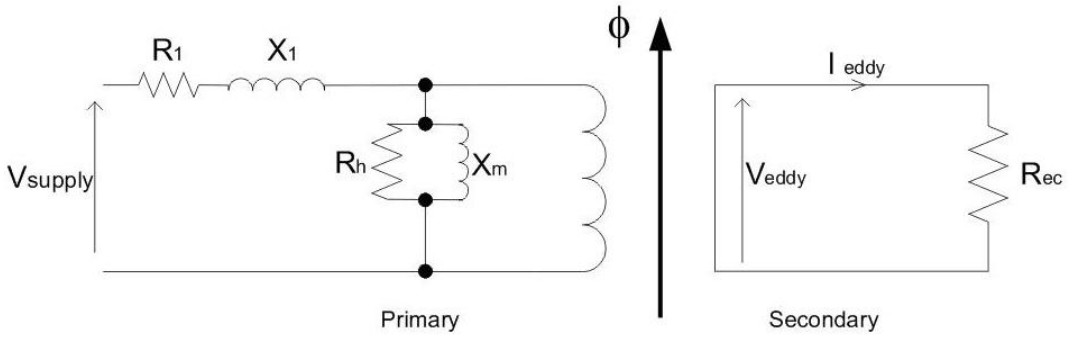

Figure 4.4: Equivalent circuit of a C-core flux generator and billet.

4.3.2 Models of billets with different lamination orientations

Billet a

For the first billet with laminations aligned with the main flux, V_{eddy} is the sum of the emfs from each lamination, and is equal to the supply voltage divided by the number of primary

winding turns, N_1. The flux is distributed evenly in each lamination and the emfs induced by the flux is the same. The emf in each lamination depends on the number of laminations N_{lam}, and is $\frac{V_{eddy}}{N_{lam}}$. Hence, the thinner the lamination and the more laminations there are, the smaller the emf is in each lamination. Because of the identical physical characteristics, the resistance of each lamination is the same, and hence the eddy current induced by the emf flowing in each lamination is also equivalent. The electrical model for the laminations from Billet **a** is considered as a series circuit as shown as **Figure 4.5**.

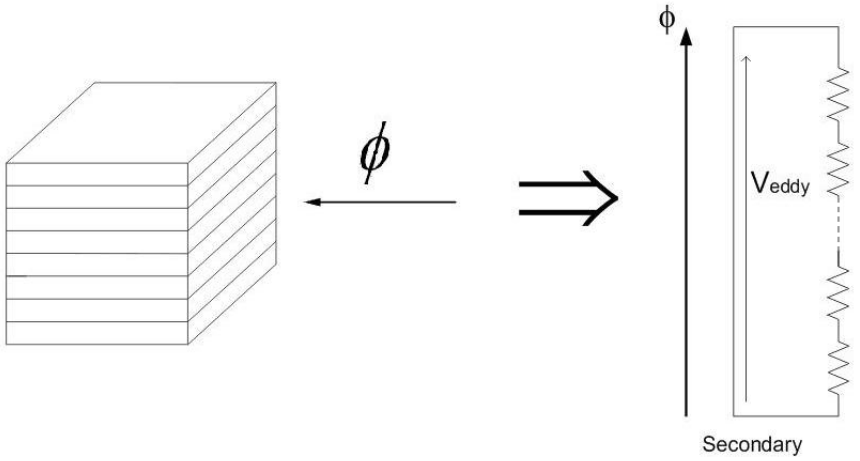

Figure 4.5: Electrical circuit of laminations for Billet **a**.

Billet b

In the second orientation, the flux coming through each lamination is the same, and is the total flux generated by the primary winding. Therefore, the magnitude of the emf in each lamination is V_{eddy}. With the same resistance for every lamination, the eddy current flowing in each lamination is the same. The electrical model for the laminations in Billet **b** is considered as a parallel circuit as shown as **Figure 4.6**.

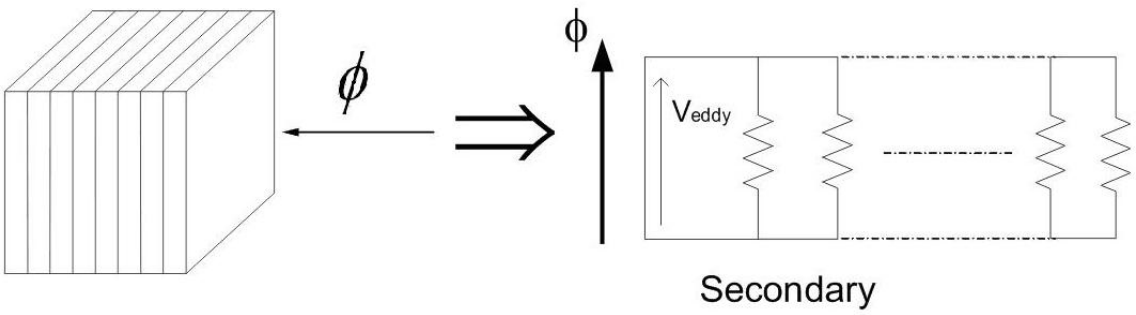

Figure 4.6: Electrical circuit of laminations for Billet **b**.

4.4 Current density comparison of two cubical billets with different orientations under a uniform flux condition

In general, power loss is proportional to current density squared. Since the eddy currents flowing through the billet are converted to heat energy, the current density can be representative of the power loss from each billet.

The dimensions of two cubical billets are shown in **Figure 4.7**.Due to the different lamination orientations, the resistance of each billet is different. Applying **Eq:3.4**, with laminations aligned with the main flux, the resistance of a single lamination of Billet **a** is:

$$R_a = \rho \cdot \frac{4L}{T \cdot W} \tag{4.1}$$

where ρ is the resistivity of the billet, L is the length of the billet, T is the thickness of the lamination and W is the width of the billet.

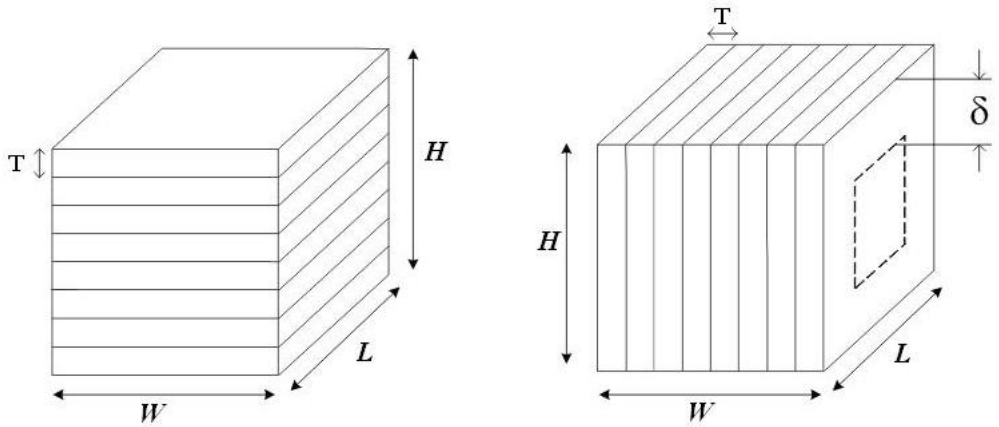

Billet **a** Billet **b**

Figure 4.7: Dimensions of two cubical billets.

Applying **Eq:3.3**, with laminations orthogonal to the main flux, the resistance of a single lamination of Billet **b** is:

$$R_b = \rho \cdot \frac{2H + 2L - 4\delta}{\delta \cdot T} \tag{4.2}$$

where H is the height of the billet and δ is the skin depth.

The edge lengths of a cubical frame in three dimensions are equal, thus $H = W = L$.

Normally, the thickness of a lamination should be less than or equal to twice the skin depth δ (Liew et al., 2001). In this case, it is assumed that $T = 2\delta$. Hence the number of laminations is:

$$N_{lam} = \frac{H}{T} = \frac{H}{2\delta} = \frac{W}{2\delta} \tag{4.3}$$

Under a uniform flux condition, for each orientation, the physical characteristics and the geometry of each lamination are the same. Therefore, the current density for each lamination is the same. Instead of comparing the current density of two whole cubical billets, only the current density for a single lamination is required. The eddy current of a single lamination in cubical Billet **a** is:

$$I_a = \frac{\frac{V_{eddy}}{N_{lam}}}{R_a} = \frac{V_{eddy} \cdot T \cdot W}{\rho \cdot N_{lam} \cdot 4L} \tag{4.4}$$

Since from **Eq:4.3**, $W = N_{lam} \cdot 2\delta$, then

$$I_a = \frac{V_{eddy} \cdot \delta \cdot T}{\rho \cdot 2L} \tag{4.5}$$

Similarly, the eddy current of a single lamination in cubical Billet **b** is:

$$I_b = \frac{V_{eddy}}{R_b} = \frac{V_{eddy} \cdot \delta \cdot T}{\rho \cdot (2H + 2L - 4\delta)} = \frac{V_{eddy} \cdot \delta \cdot T}{\rho \cdot 4(L - \delta)} \tag{4.6}$$

The cross sectional area A_a of the eddy current in a single lamination in Billet **a** is:

$$A_a = \frac{T}{2} \cdot W \tag{4.7}$$

The cross sectional area A_b of the eddy current in a single lamination in Billet **b** is:

$$A_b = \delta \cdot T \tag{4.8}$$

Therefore, the eddy current density J_a for a single lamination in Billet **a** is:

$$J_a = \frac{I_a}{A_a} = \frac{V_{eddy} \cdot \delta \cdot T}{\rho \cdot 2L} \cdot \frac{2}{T \cdot W} = \frac{V_{eddy}}{\rho} \cdot \frac{\delta}{L \cdot W} \tag{4.9}$$

and the eddy current density J_b for a single lamination in Billet **b** is:

$$J_b = \frac{I_b}{A_b} = \frac{V_{eddy} \cdot \delta \cdot T}{\rho \cdot 4(L - \delta)} \cdot \frac{1}{\delta \cdot T} = \frac{V_{eddy}}{\rho} \cdot \frac{1}{4(L - \delta)} \tag{4.10}$$

Taking the ratio of J_a and J_b:

$$\frac{J_a}{J_b} = \frac{\frac{V_{eddy}}{\rho} \cdot \frac{\delta}{L \cdot W}}{\frac{V_{eddy}}{\rho} \cdot \frac{1}{4(L-\delta)}} = \frac{4\delta(L-\delta)}{L \cdot W} \tag{4.11}$$

Since $L \gg \delta$, then $L - \delta \approx L$. Hence, the current density ratio becomes:

$$\frac{J_a}{J_b} = \frac{4\delta}{W} \tag{4.12}$$

As $T = 2\delta$, if $\frac{4\delta}{W} < 1$, then $\frac{2T}{W} < 1$. Therefore

$$W > 2T \tag{4.13}$$

As a result, if the number of laminations is more than 2, the current density of the Billet **b** is larger than that in the Billet **a**. In general, the power loss per unit volume (V) is (Davies, 1990):

$$\frac{P}{V} = \rho \cdot J^2 \tag{4.14}$$

Therefore, for any two cubical billets with different orientations but the same volume, as shown as **Figure 4.7**, and if the number of laminations is more than 2, the eddy current power loss of the billet with the laminations orthogonal to the main flux is larger than the eddy current power loss of the billet with the laminations aligned with the main flux.

4.5 Simulation

Quick Field (Tera Analysis, 2001), as a field simulation software program, applies a finite element analysis method to build up an interactive environment for electromagnetic, thermal and stress analysis. The AC magnetic analysis feature was applied to create two simulation models. The geometry and the size of the two created models matched the apparatus used in the experiments.

4.5.1 Simulation for Apparatus 1

Since the windings were right beside the air gap of the C-core, the flux was generated with low fringing. Under normal operating conditions, the different orientations from

each billet lead to a significant current density difference. Due to the requirements of the Quick Field program, the permeability for each billet and the core was set to 2000 (Liew et al., 2001). The turns ratio is $\frac{N_1}{N_2} = \frac{400}{1}$, and the source voltage V_s is $100V$, hence, the secondary voltage is:

$$V_{eddy} = \frac{V_s \cdot N_2}{N_1} = 0.25V$$

Applying **Eq:4.1**, the single lamination resistance for Billet **a** is $R_a = 0.0145\Omega$. The single lamination resistance for Billet **b**, by applying **Eq:4.2**, is $R_b = 0.254\Omega$. For a single lamiantion, the cross sectional area for Billet **a** is $A_a = 2.85 \times 10^{-6}m^2$, and for Billet **b** is $A_b = 0.204 \times 10^{-6}m^2$. Therefore, the current density for Billet **a** is:

$$J_a = \frac{I_a}{A_a} = 6.04 \times 10^{4\,\mathrm{A/m^2}}$$

Similarly, the current density for Billet b is:

$$J_b = 4.82 \times 10^{6\,\mathrm{A/m^2}}$$

After setting up the current densities for the two billets in Quick Field, **Figure 4.8(a)** and **4.8(b)** display the simulated flux paths and current densities of each billet for the first set of apparatus. The differences between **Figure 4.8(a)** and **4.8(b)** are the colours from the billets and windings. The different colours stand for different current densities corresponding to the list beside the figure. Over all, the flux passing through the billet is reasonably uniform, and the flux leakage around the C-core slot is small.

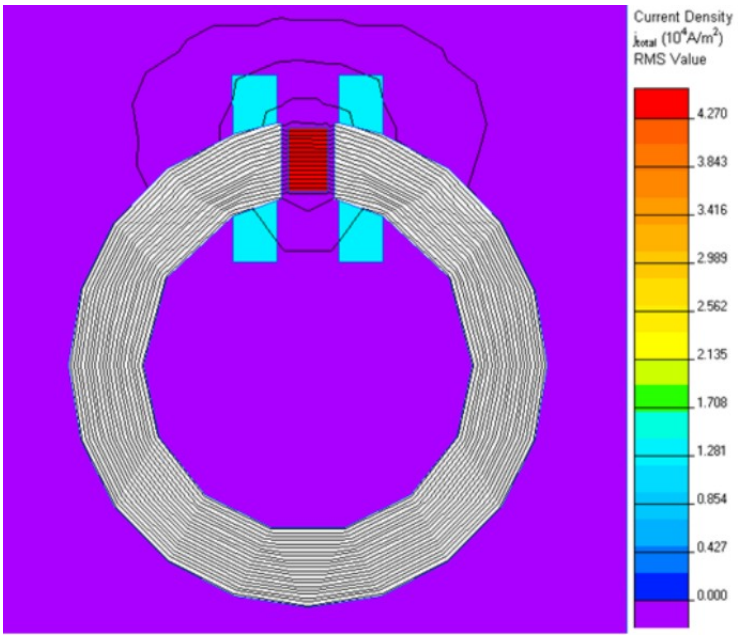

(a) Laminations of billet aligned with the main flux

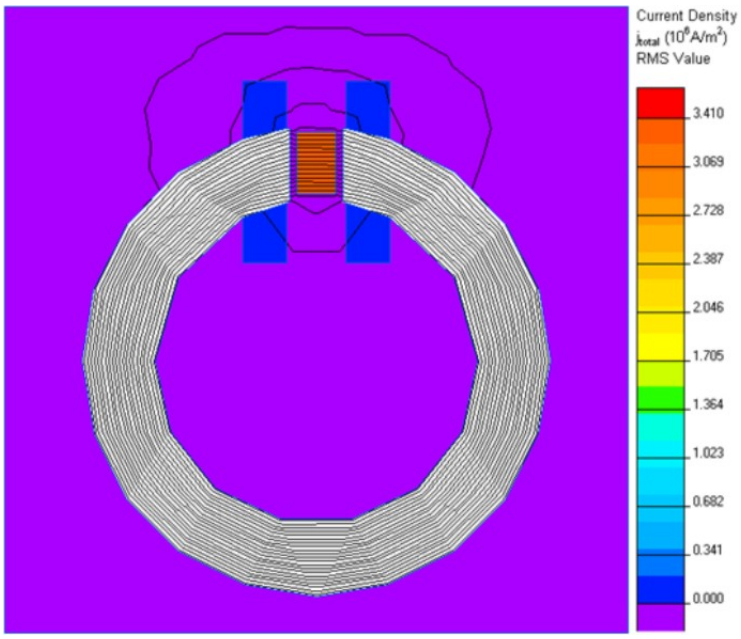

(b) Laminations of billet orthogonal to the main flux

Figure 4.8: Simulations for the first apparatus.

4.5.2 Simulation for Apparatus 2

Since the two billets used in the second apparatus have been manufactured using the same material as used in the billets in the first apparatus, the permeability of each billet and the core was also set to 2000. With the same turns ratio($^{400}/_{1}$) and the source voltage($100V$)

as for the first apparatus, the apparatus 2 secondary voltage through the billet is:

$$V_{eddy} = 0.25V$$

Applying **Eq:4.1**, the single lamination resistance for Billet **a** is $R_a = 0.0108\Omega$. The single lamination resistance for Billet **b**, by applying **Eq:4.2**, is $R_b = 0.0.1923\Omega$. For a single lamination, the cross sectional area for Billet **a** is $A_a = 5 \times 10^{-6} m^2$, and for Billet **b** is $A_b = 0.34 \times 10^{-6} m^2$. Therefore, the current density for Billet **a** is:

$$J_a = \frac{I_a}{A_a} = 7.02 \times 10^{4\mathrm{A}/\mathrm{m}^2}$$

Similarly, the current density for Billet b is:

$$J_b = 3.8 \times 10^{6\mathrm{A}/\mathrm{m}^2}$$

After setting up the current densities for the billets, the simulated flux distributions and current densities for the two billets using the second apparatus are shown in **Figure 4.9(a)** and **4.9(b)**. The difference between **Figure 4.9(a)** and **4.9(b)** is not easy to perceive from the colour of each billet. However, the current density list beside each figure with different scales shows the significant current density difference between the two billets. Due to the changed shape of the C-core and the arrangements of the windings, the flux leakage is much less than for the first apparatus. The flux through the billets is almost uniform.

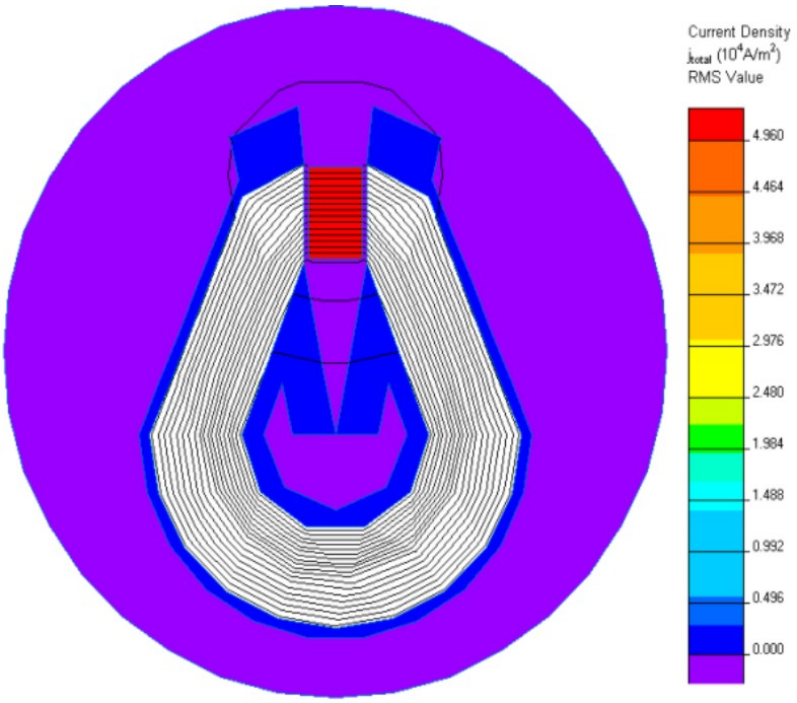

(a) Laminations of billet aligned with the main flux

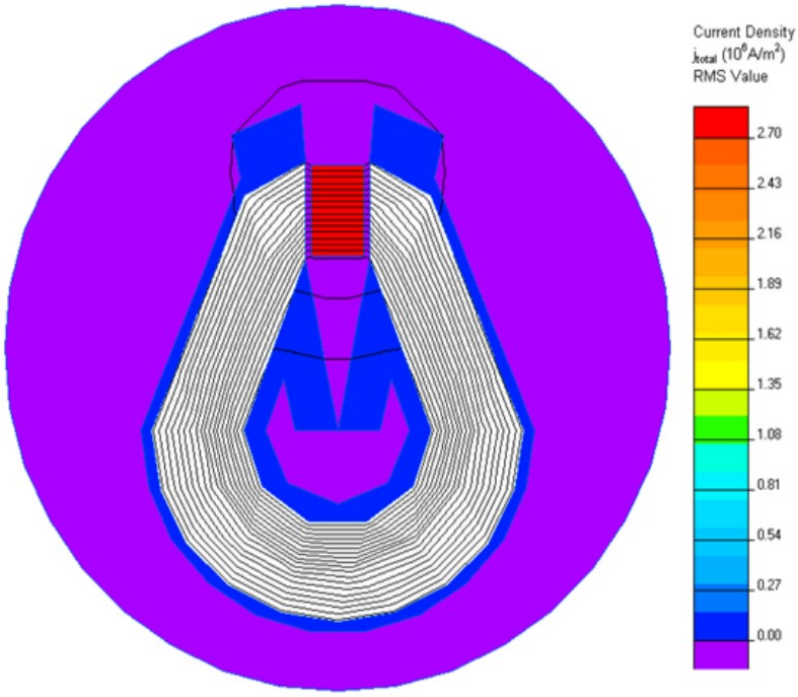

(b) Laminations of billet orthogonal to the main flux

Figure 4.9: Simulations for the second apparatus.

4.6 Experimental Results

In the experiments, the supply voltage for the first set of apparatus was increased from 10V to 100V; and the supply voltage for the second set of apparatus was increased from

10V to 150V. The input power and the input current were recorded. The measurement instruments used in the experiment were a FLUKE41 Power Harmonics analyzer, a current meter (Yokogawa 2433), a variac (VARITRANS TV44) and an oscilloscope (Tektronix TDS220 OC259).

The experiments measure the eddy current power loss and hysteresis power loss together. However, for each apparatus, since the weights of the billets were close to each other, the hysteresis power losses can be considered to be the same (McPHERSON & LARAMORE, 1990). By subtracting the experimental results of Billet **a** from those of Billet **b**, the eddy current power difference can be obtained. This result is then divided by the difference in the calculated values of the eddy currents of the two billets to give a scale factor.

4.6.1 Apparatus 1

Figure 4.10 shows the eddy current losses calculated using the developed theory.

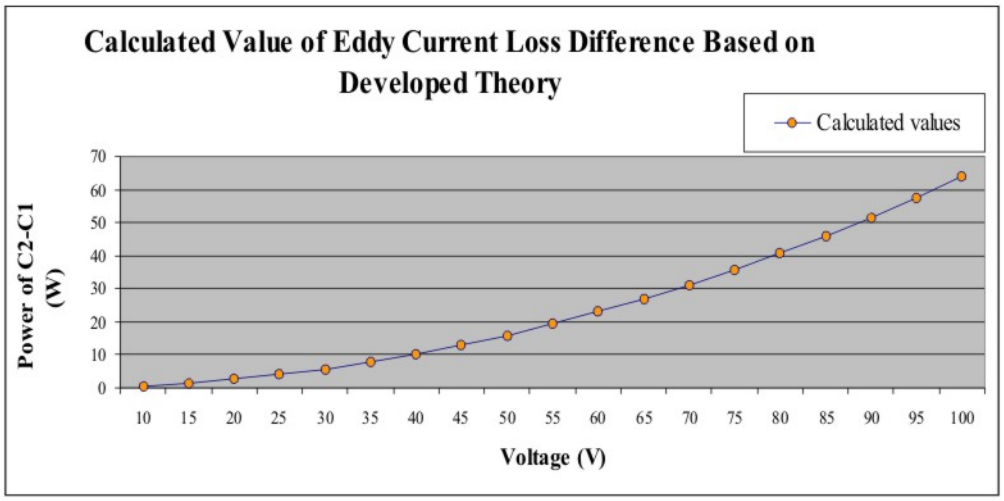

Figure 4.10: Calculated eddy current loss difference for the first apparatus.

Based on the developed theory, $C2$ stands for calculated eddy current loss for the Billet **b** and $C1$ stands for the calculated eddy current loss for Billet **a**.

Figure 4.11 shows the experimental results obtained from the power meter and the oscilloscope. The results show a reasonable match between the two instruments.

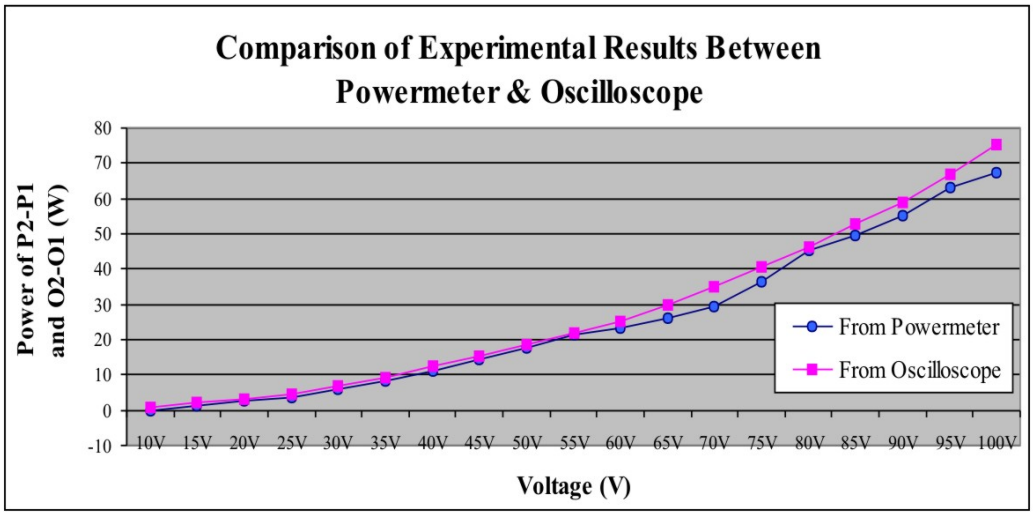

Figure 4.11: Comparison of the experimental results from the power meter & the oscilloscope for the first apparatus.

$P2 - P1$ stands for the difference of the experimental results using Billet **b** and Billet **a**, measured using the power meter. $O2 - O1$ stands for the difference of the experimental results using Billet **b** and Billet **a**, measured using the oscilloscope. Comparing **Figure 4.10** and **Figure 4.11**, the scales of the power loss do not match. However, the shape of the curves from **Figure 4.10** and **Figure 4.11** are comparable. Hence a scale factor can be introduced into the developed equations. **Figure 4.12** gives a comparison of the two scale factors for the power meter $\frac{P2-P1}{C2-C1}$ and the oscilloscope $\frac{O2-O1}{C2-C1}$ separately. The dot line (blue curve) displays a scale factor obtained by dividing the experimental results from the data recorded by the power meter with the calculated values. The square line (purple curve) shows the scale factor obtained by dividing the experimental results from the data recorded by the oscilloscope with the calculated values. Both the results show that the scale factor is about 1.15.

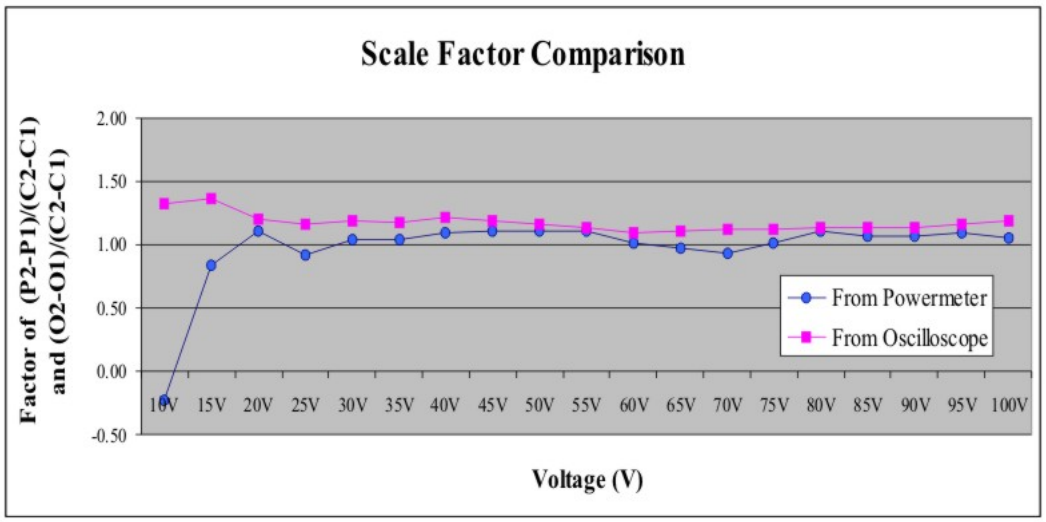

Figure 4.12: Scale factor comparison between using the power meter & the oscilloscope for the first apparatus.

4.6.2 Apparatus 2

For the second set of apparatus, the calculated eddy current differences are shown in **Figure 4.13**.

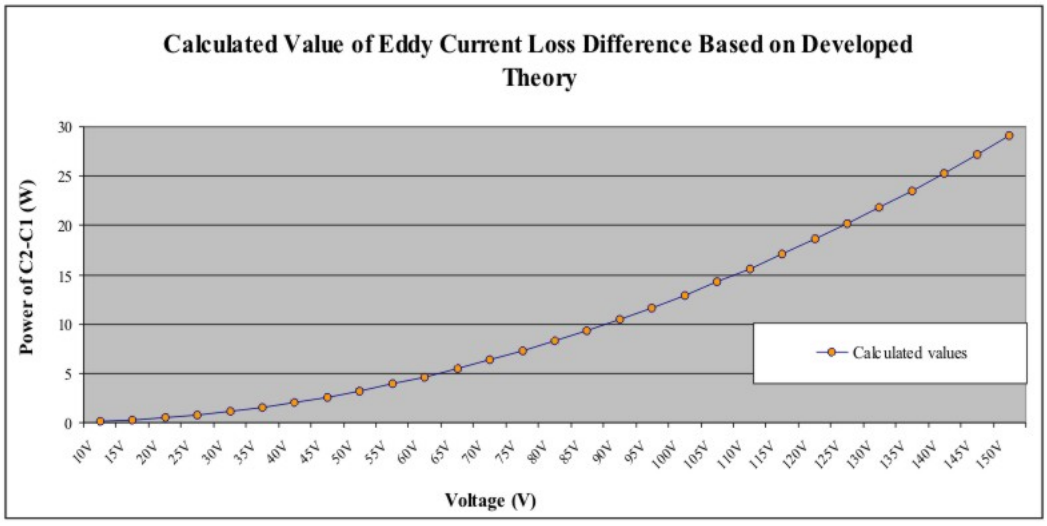

Figure 4.13: Calculated eddy current loss difference for the second apparatus.

Figure 4.14 displays the experimental results from the Power meter and Oscilloscope. The two instruments give a reasonable match over the first 100V, but separate after that.

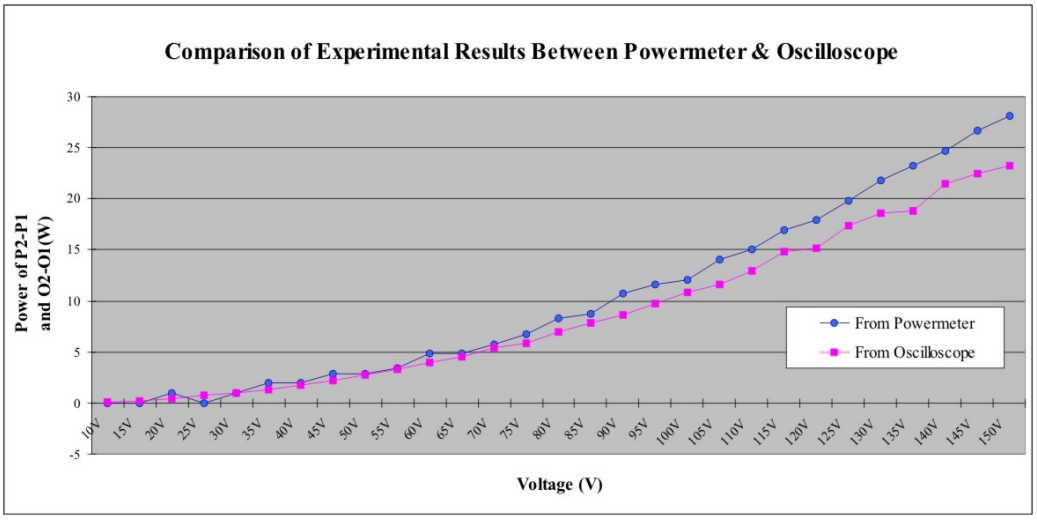

Figure 4.14: Comparison of the experimental results from the power meter & the oscilloscope for the second apparatus.

A comparison between **Figure 4.13** and **Figure 4.14** shows that the shape of the curves and the scale of the power dissipation are similar. **Figure 4.15** shows that using the scale factor from the power meter is more constant after 70V. It is close to unity. The average scale factor from using the oscilloscope is about 0.85.

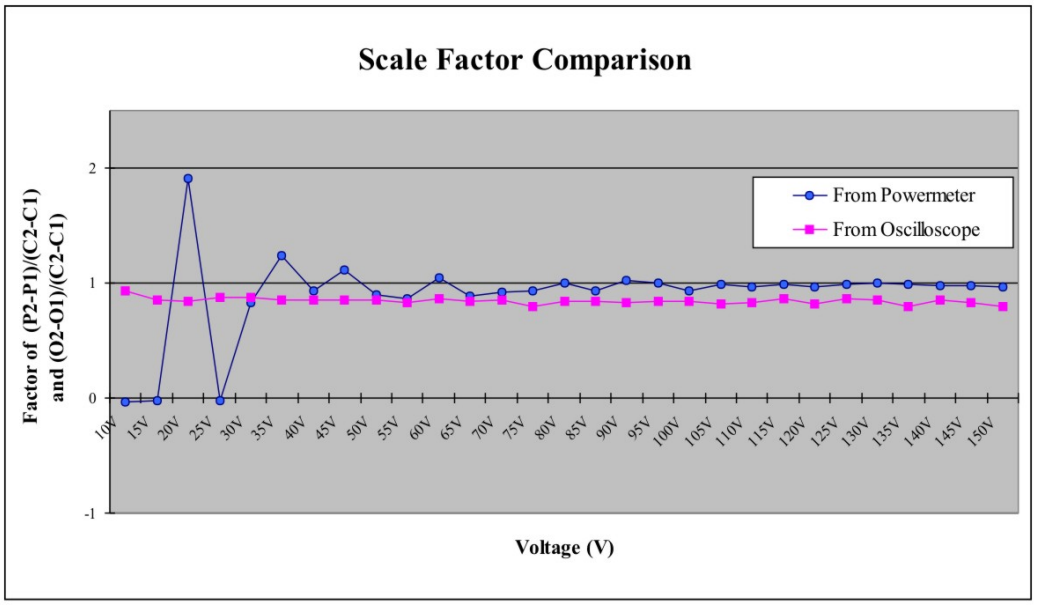

Figure 4.15: Scale factor comparison between using the power meter & the oscilloscope for the second apparatus.

4.7 Discussion

The developed theory has been applied to the uniform flux experiments by using different apparatus. The results return two scale factors close to each other. From a construction point of view, and the flux phenomenon returned from Quick Field, the second apparatus was designed for a low leakage surrounding the C-core and high uniform flux through the slot.

Looking at the scale factor comparison from **Figure 4.15**, because there is a low accuracy issue for the power meter operating at low voltages, a large divergence occurred before 70V. However, comparing the scale factors from the two instruments after 70V, there is always a margin between the two results. Hence the error bands for the two instruments were investigated. **Figure 4.16** displays the scale factor comparison with the error band for both the power meter (PM) and the oscilloscope (OS). At steady state, and higher than 70V, the lower error band from the power meter is almost fully overlapped with the upper error band from the oscilloscope. However, since the power meter is the most common instrument used for measuring experimental data in practice, and the purpose of the oscilloscope is to obtain waveforms and is mostly used in electronics; the scale factor from the power meter can be used. The results from the power meters in the two experiments show the scale factors are close to unity, which means the developed theory can accurately predict the eddy current power loss under uniform flux conditions.

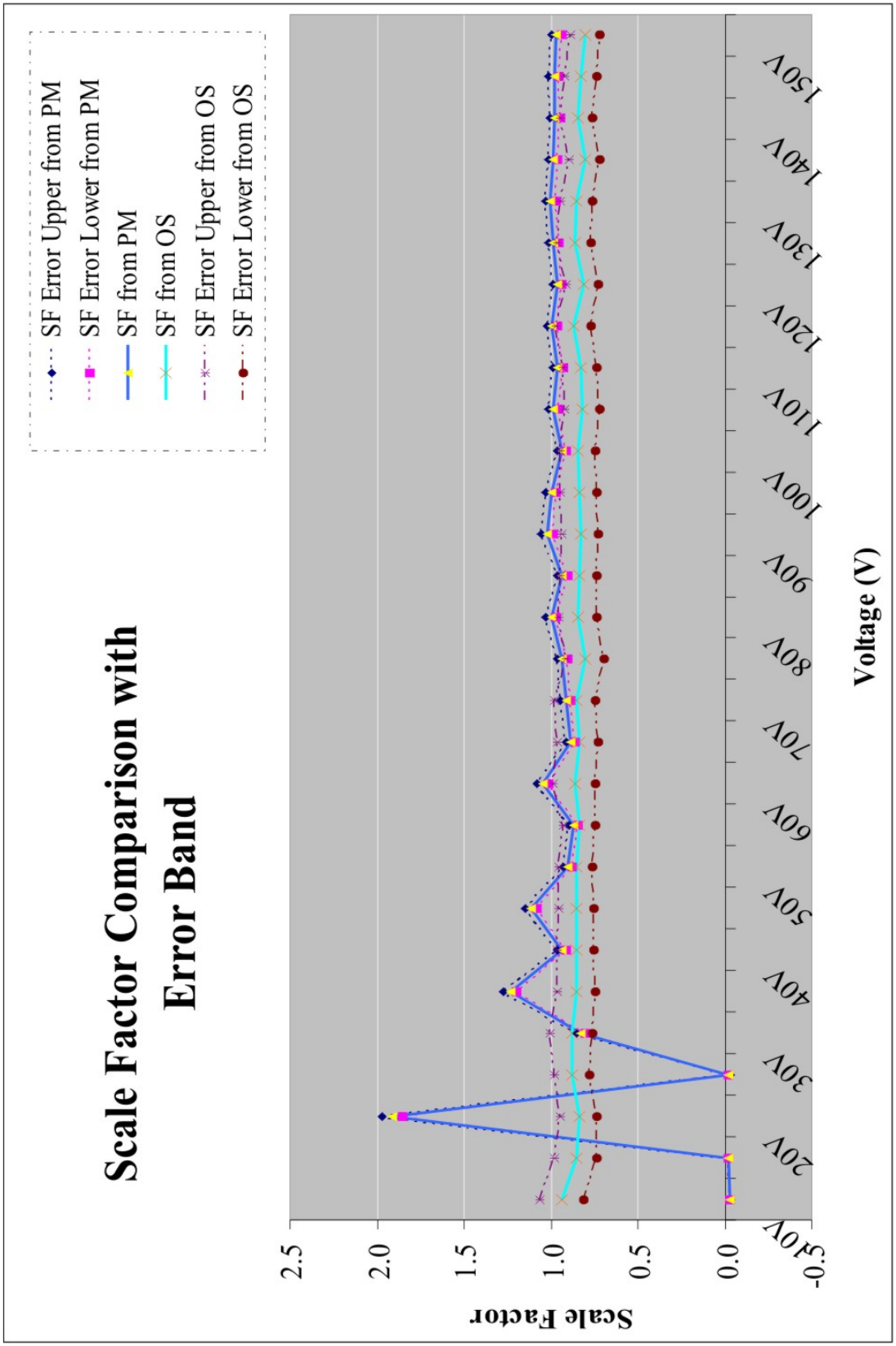

Figure 4.16: Scale factor comparison with error band.

4.8 Conclusion

Two sets of apparatus designed to generate uniform flux density in an air gap have been introduced in this report. The concepts behind the experiment and the electrical models for determining the eddy current losses in the billets have been explained.

The power loss in a cubical billet with the laminations orthogonal to the main flux, has been shown to be larger than that of a cubical billet with the laminations aligned with the main flux, as long as the number of laminations is greater than 2.

Two experiments have been simulated using the Finite Element Analysis (FEA) program Quick Field to show the difference between the two lamination alignments. Experimental results give two scale factors for the developed theory. Due to the poorer construction of the first set of apparatus, the scale factor of measured to calculated losses is 1.15. The scale factor from the second set of apparatus is more reliable and can be taken as unity.

Since the power meter is the most common instrument used for measuring experimental data in practice, the unity scale factor can be used. Several small partial core transformers with rectangular cores could be tested to further validate the developed theory on eddy current losses.

Chapter 5

CORE LOSS OF CUBICAL PARTIAL CORE TRANSFORMERS

5.1 Introduction

After verification of the developed equations for modelling the uniform flux experiments, the focus of the Eddy Current (EC) power loss calculation turned to partial core transformers. Some cubical partial core transformers were available, of different physical sizes. Since the cores were cubical, the developed methods can be applied, which is the first-step in investigating the EC power loss of the partial core transformer.

In this chapter, the background to the flux distribution of the cubical core is reviewed. Three key factors (L', K_{ec} and β_a) are introduced into the EC power loss model. L' is a length which indicates the region of the flux spreading at the ends of the core. K_{ec} as a ratio indicates how much of the main flux spreads at the ends of the core. β_a is the ratio of the winding axial length and winding thickness. Side views of the flux out of the partial core in two orthogonal angles are displayed using MagNet (Infolytica, 2009) simulations. EC resistance and power loss models are built up and the relationships between the three key factors are studied.

5.2 Flux Distribution for Cubical Partial Core

For a partial core transformer under normal operating conditions, going from the middle to the top of the core, the flux starts to spread out. In the middle section of the core, since

the core is laminated, the induced flux is distributed uniformly through the laminations. As soon as the flux starts spreading, the density of the flux induced from the primary winding through the direction **'a'** of **Figure 5.1** (along the laminations) starts to reduce, and at the same time, the flux density increases in directions orthogonal to the direction **'a'**.

As an approximation, the directions for the flux outwards from a cubical partial core can be defined in the directions of the three main axes **'a'**, **'b'** and **'c'**, as shown in **Figure 5.1**.

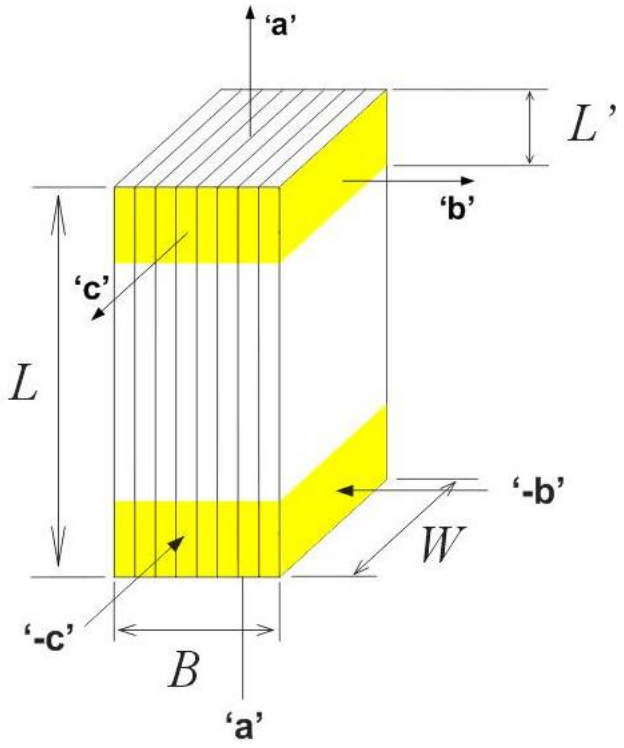

Figure 5.1: An approximation of the flux directions for a cubical partial core.

Figure 5.1 also shows the geometry and dimensions (L is the length, B is the breadth, and W is the width) of the laminated cubical partial core. The shadow area in **Figure 5.1** shows the region of the core through which the flux spreads out.

5.3 Three Key Factors

Three key factors which affect the flux distribution are L', K_{ec} and β_a . Each of these factors is introduced and explained in this section.

5.3.1 Factor L'

L' is a length which indicates the region of the flux spreading at the ends of the core. The flux spreading from the upper and lower ends of the core is symmetrical, hence, L' is the same at both ends. As a result of bringing in the factor L', the partial core is divided into three parts, the top section, the middle section, and the bottom section as shown in **Figure 5.2**.

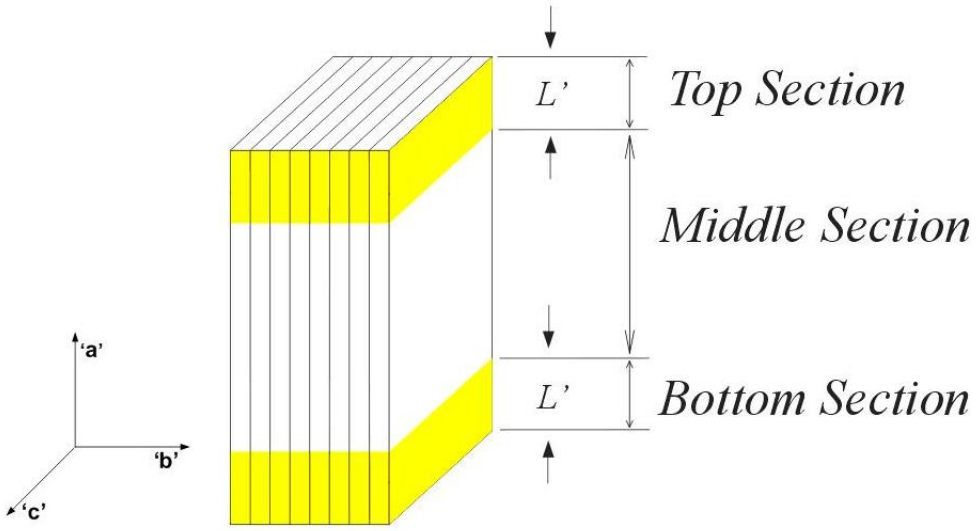

Figure 5.2: The three sections for a cubical partial core.

5.3.2 Factor K_{ec}

When the flux starts to spread out at both ends of a cubical partial core, the spreading flux is evenly distributed through the directions outwards in the plane which is orthogonal to the direction **'a'**. Under the operating conditions, the flux through the core is generated by the primary winding. Due to the spreading conditions of the flux at the core ends, the density of the flux spreading out is relatively smaller than the density of the main flux induced by the primary winding in the middle section of the core. The flux going through the directions **'b'** and **'c'** is proportional to the flux induced by the primary winding.

For the flux within the spreading region of the core, it is assumed that it goes through both directions **'b'** and **'c'** with the same density. The factor that determines how much the flux goes outwards in the directions **'b'** and **'c'** from the direction **'a'** is denoted K_{ec}.

With respect to the electromagnetic force (emf or e) induced by the flux through the core, if the spreading factor is K_{ec}, then the emf in the directions **'b'** and **'c'** at the end sections of the core is $e \cdot K_{ec}$. The rest of the emf due to the flux going through direction **'a'** is thus $e \cdot (1 - K_{ec})$. **Figure 5.3** shows the emf for the three directions for the top section of the core. The factor K_{ec} can vary from 0% to 100%. The greater K_{ec}, the more the flux spreads from the direction **'a'** to the directions **'b'** and **'c'**.

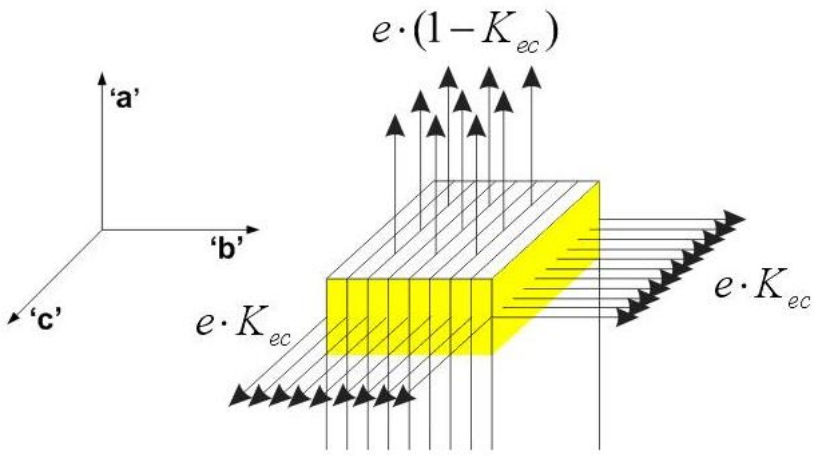

Figure 5.3: Emfs in three directions for a cubical partial core.

5.3.3 Aspect Ratio β_a

The winding aspect ratio β_a (Liew & Bodger, 2001) is given by

$$\beta_a = \frac{l_w}{\tau_{12}} \tag{5.1}$$

where l_w is the axial length of the winding (if the primary and the secondary winding axial length are different, then an average axial winding length of both the primary and the secondary can be taken), and τ_{12} is the winding thickness factor, which includes the thickness of the primary, the secondary and the insulation between the primary and the secondary windings. The smaller the aspect ratio, the greater the leakage; which means the more the flux comes out from the sides rather than from the end of the core.

5.4 Software Simulations Using MagNet

Quick Field (student version) [18] can only support 255 nodes as the mesh-limit in plotting the flux field. Since a higher flux resolution was required, the Quick Field program was insufficient to plot the flux field. Therefore, the simulation software was changed from Quick Field to MagNet (Infolytica, 2009).

2D and 3D models can be built up in MagNet with visualizations. Magnetostatic, time-harmonic, transient, or transient with motion analysis are provided in MagNet. In MagNet, magnetostatic and time-harmonic fields are two different field conditions. The magnetostatic (static) field does not change with time. It is determined by a DC current source or permanent magnet. For the time-harmonic field, since the source current is a sinusoidal alternating quantity and the magnetic materials are linear; then the EC, which is also sinusoidal, is induced in the conducting materials. The generated magnetic field is also sinusoidal. In many applications involving alternating fields, if the eddy-current effects are small, a static field solution gives good results (Infolytica, 2007).

One of the objectives of the research was to develop the equations to calculate the EC power loss in the partial core. Hence, all the simulations that were undertaken were modelled using the time-harmonic setting. Five partial core transformers PC1, PC2, PC3, PC4 and PC6, were built in the year 2000 by M.C.Liew (Liew, 2001), and they were all made with a cubical partial core shape. **Figure 5.4** shows a cubical partial core transformer construction view (Liew, 2001). B_{core} is the breadth of the core and W_{core} is the width of the core.

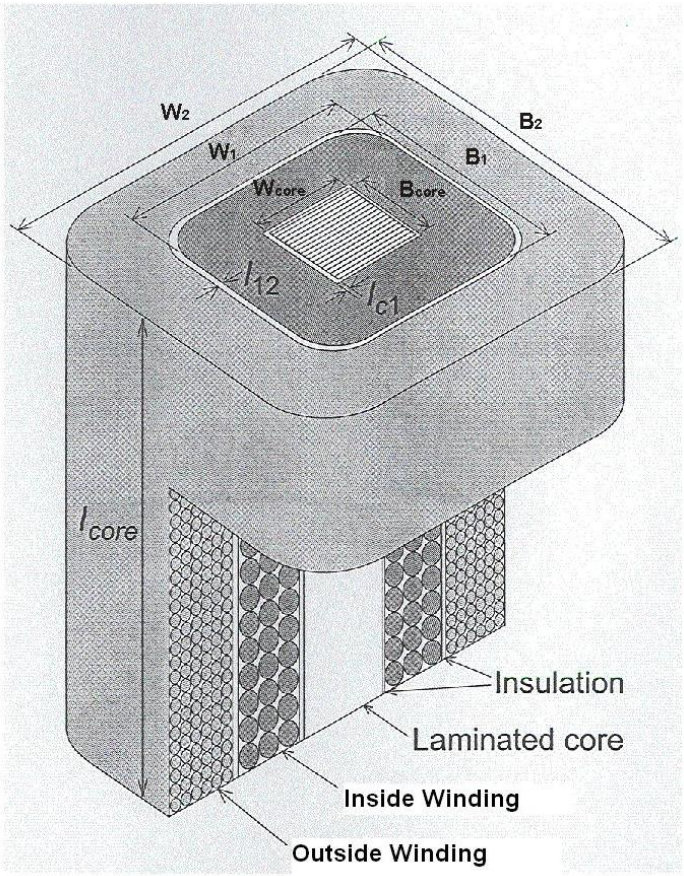

Figure 5.4: A cubical partial core transformer construction view (Liew, 2001).

5.4.1 Flux Perspective from Different angles in Cubical Partial Core

The first simulation was for PC1. Observations from two orthogonal angles have been made. The first angle of view was looking through the width plane, which is the plane parallel to the lamination cut direction. The second angle of view was looking through the breadth plane, which is the plane orthogonal to the lamination cut direction.

The 2-D cubical partial core model in MagNet shows the flux perspective which is viewed from the front plane of the core. In constructing the geometry of the transformer PC1, the parameters required in MagNet include the volume and cross sectional area of the core, the number of winding turns, and the material properties (including magnetic permeability, electric conductivity and mass density) of the core and windings.

The Width Plane Observation

Figure 5.5 shows the PC1 construction as a solid model in MagNet. The winding blocks are linked to each other by the winding settings. With the width plane view, no laminations are observed in that direction, hence, the core modelling used a solid block which achieves the same effect as a single lamination in that direction.

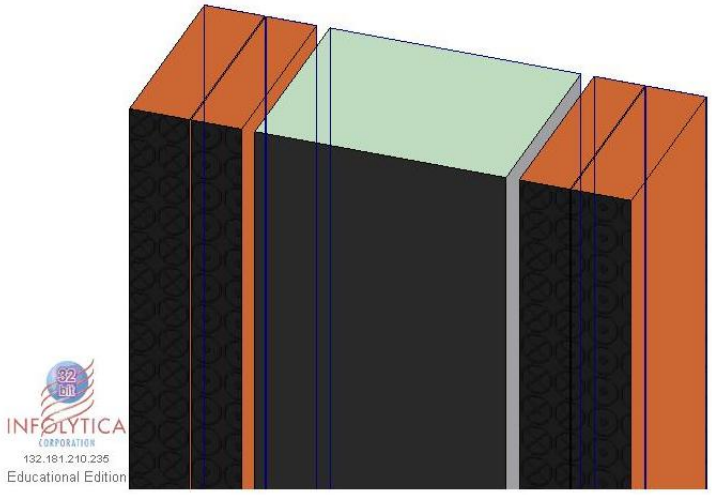

Figure 5.5: Construction of the cross sectional width view for PC1 as a solid model.

After setting up an open circuit condition and the actual geometry size for PC1, the 2-D flux field plot for a cross sectional width view is shown in **Figure 5.6**. The flux is symmetrical on both sides; it goes near the inside rim of the core due to the skin depth. The dots in the top middle section of the core and the asymmetry of the field outside the model are caused by minor computation errors in MagNet.

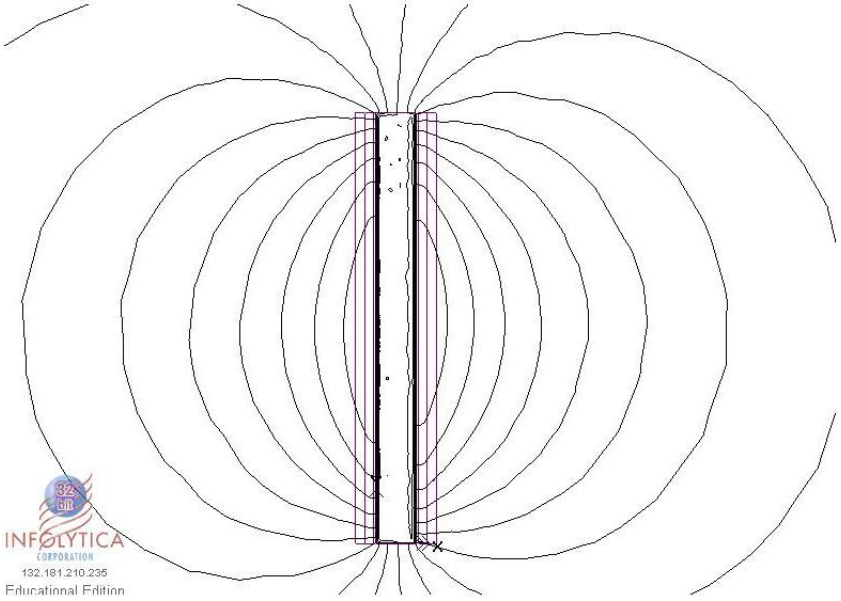

Figure 5.6: Flux plot of the cross sectional width view for PC1.

Figure 5.7 displays the flux density view with flux lines. From this plot, the flux density increases nearer to the sides.

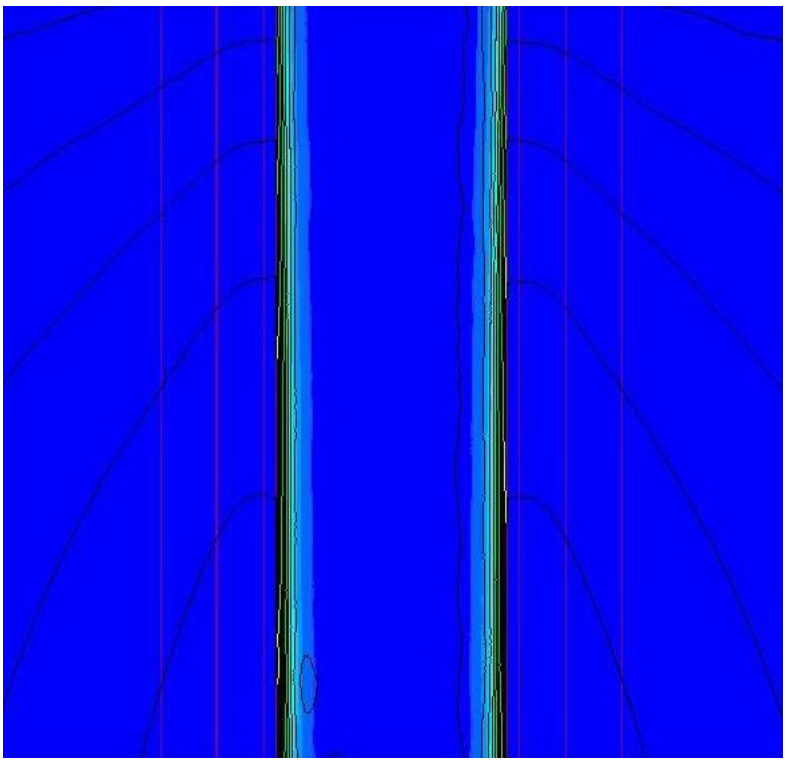

Figure 5.7: Flux density image of the cross sectional width view for PC1.

The Breadth Plane Observation

The core of PC1 consists of 62 pieces of 0.5mm thick laminations, with a stacking factor of 0.95. The laminations can be presented in a wireframe model in MagNet as shown in **Figure 5.8**.

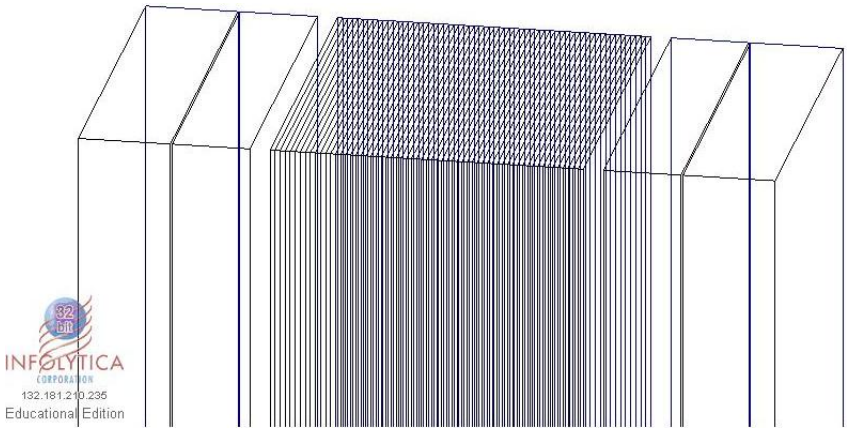

Figure 5.8: Construction of the cross sectional breadth view for PC1 in a wireframe model.

Figure 5.9 shows a 2-D flux plot of a cross sectional breadth view for an open circuit condition.

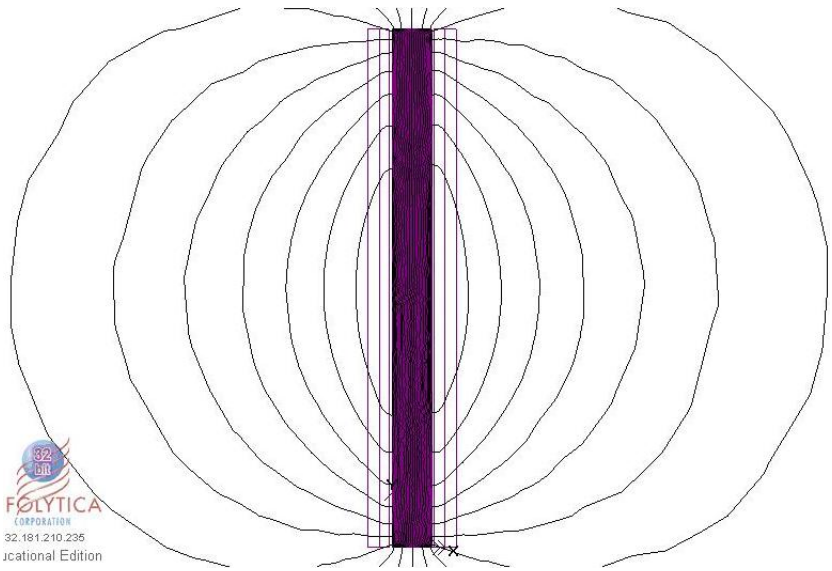

Figure 5.9: Flux plot of the cross sectional breadth view for PC1 for an open circuit condition.

From **Figure 5.9**, due to the laminations of the core, the flux passing through the whole core is approximately uniform. An almost symmetrical flux field has been plotted, and the flux density is slightly higher at the corners of the core. **Figure 5.10** shows a flux density plot with flux lines for the upper section of PC1.

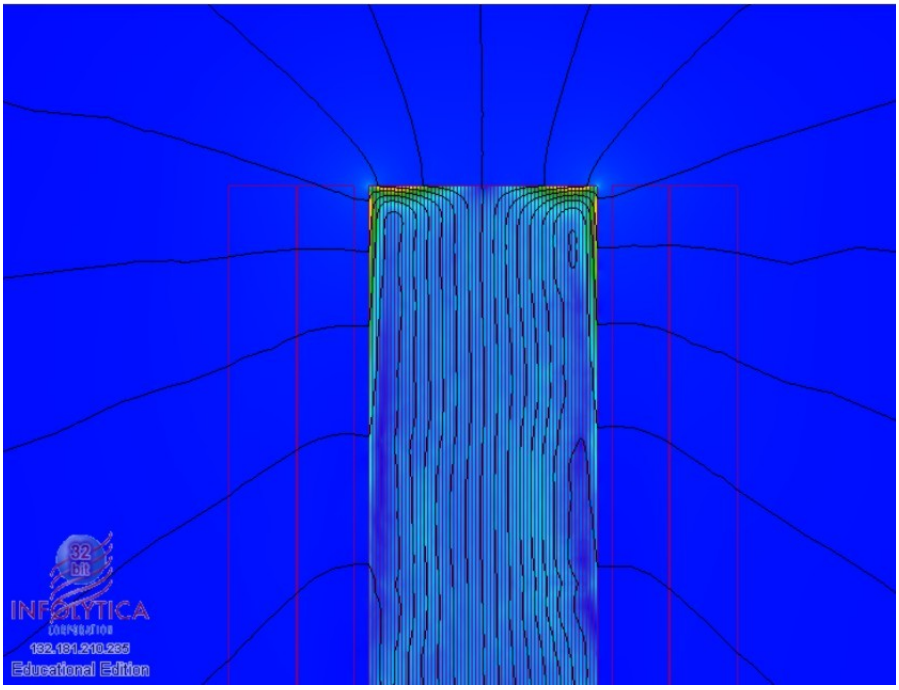

Figure 5.10: Flux density image of the cross sectional breadth view for PC1 for the top section.

5.4.2 Results from MagNet

The 'transformer equation' (Paul et al., 1986) describes the relationship between the voltage and the magnetic flux density B induced by the primary winding:

$$B = \frac{V_1}{(2\pi/\sqrt{2}) \cdot N_1 \cdot f \cdot A_c} \tag{5.2}$$

where A_c is the cross sectional area of the core, f is the frequency and N_1 is number of turns on the primary winding.

Since the Root Mean Square (RMS) value of flux ϕ_{RMS}(Weber) is

$$\phi_{RMS} = \frac{B \cdot A_c}{\sqrt{2}} \tag{5.3}$$

then the RMS flux linkage λ_{RMS} (Weber-turns) can be given as

$$\lambda_{RMS} = \phi_{RMS} \cdot N_1 = \frac{V_1}{2\pi f} \tag{5.4}$$

Referring to the open circuit experiment results from M.C.Liew (Liew, 2001), the returned values from MagNet simulation, and the calculations obtained from **Eq:5.4**; a comparison

of the flux linkage for the 5 cubical partial core transformers is listed in **Table 5.1**.

	PC1	PC2	PC3	PC4	PC6
Flux Linkage from MagNet simulations	-j0.381	-j0.731	-j0.061	-j0.731	-j0.731
Flux Linkage from the experimental results	-j0.379	-j0.737	-j0.065	-j0.741	-j0.730
Flux Linkage calculation from **Eq:5.4**	-j0.382	-j0.732	-j0.064	-j0.732	-j0.732

Table 5.1: A comparison of the flux linkage for the 5 cubical partial core transformers.

The flux linkage from the MagNet simulations, the experiment results and the calculation from **Eq:5.4** are very well matched for all the partial core transformers. This indicates a high degree of confidence in constructing a flux field using MagNet.

The flux fields of PC1 from two directions have been simulated and plotted in MagNet as **Figure 5.6** and **Figure 5.9**. Both these figures show lengths where the flux starts spreading to the end of the core.

5.5 Eddy Current Resistance of Single Lamination

Due to the different flux conditions, the core has been divided into three sections. In each section, due to the different lengths of the EC pathways, the EC resistance due to the flux going through each direction is different. In general, the EC resistance induced by the flux through any direction (**'a'**, **'b'**, or **'c'**) can be represented by

$$R = \rho \cdot \frac{l}{A} \tag{5.5}$$

where ρ is the resistivity of the conductor, l is the average length of the EC pathway and A is the cross sectional area of the EC pathway.

Figure 5.11presents a picture of the EC pathway from the three directions, for a single lamination.

The dotted line indicates the skin depth of the EC pathway in direction **'b'** for a single lamination. It is normal that the lamination thickness is less than twice the skin depth δ.

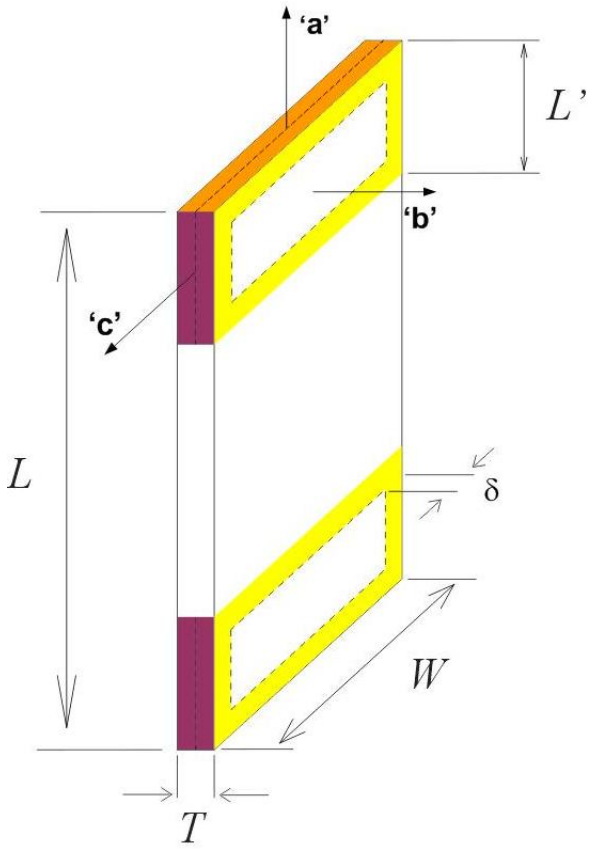

Figure 5.11: EC pathway from three directions for a single lamination.

Hence the EC pathway is restricted and reduced in directions **'a'** and **'c'**. Therefore, the EC resistance in the directions **'a'** and **'c'** is increased, relative to that in direction **'b'**.

5.5.1 Top Section

At the top section of the core, it is assumed that the respective fluxes through the directions **'a'**, **'b'** and **'c'** are uniform. By applying **Eq:5.5**, the EC resistance in direction **'a'** can be represented by

$$R_{ec\_Ta} = \rho \cdot \frac{2\left[W - 2(T/2) - 2(T/2)\right]}{L' \cdot (T/2)} = \rho \cdot \frac{4W}{L' \cdot T} \tag{5.6}$$

where ρ is the resistivity of the lamination material, W is the width of the lamination, L' is the axial length of the top section, and T is the thickness of the lamination.

The EC resistance in direction **'b'** is

$$R_{ec\_Tb} = \rho \cdot \frac{2W + 2L' - 4\delta}{\delta \cdot T} \tag{5.7}$$

The EC resistance in direction **'c'** is

$$R_{ec\_Tc} = \rho \cdot \frac{4L'}{W \cdot T} \tag{5.8}$$

5.5.2 Middle Section

Inside the middle section of the core, it is assumed that there is no spreading flux, and all the flux goes uniformly through direction **'a'**. Therefore, the EC resistance only exists in direction **'a'**, which can be defined as:

$$R_{ec\_Ma} = \rho \cdot \frac{4W}{(L - 2L') \cdot T} \tag{5.9}$$

where L is the length of the lamination.

5.5.3 Bottom Section

Since there is a symmetrical flux distribution for both ends of the core, the EC resistance through the three directions in the bottom section are the same as for the top section. The EC resistances at the bottom section are thus

$$R_{ec\_Ba} = \rho \cdot \frac{4W}{L' \cdot T} \tag{5.10}$$

$$R_{ec\_Bb} = \rho \cdot \frac{2W + 2L' - 4\delta}{\delta \cdot T} \tag{5.11}$$

$$R_{ec\_Bc} = \rho \cdot \frac{4L'}{W \cdot T} \tag{5.12}$$

5.6 Power Loss Model of Cubical Partial Core

When calculating the power loss from a partial core, two components are taken into account. These are the hysteresis loss and the EC loss.

5.6.1 Hysteresis Loss

The formula to calculate the hysteresis loss for a partial core transformer is defined as (Bodger et al., 2000):

$$P_{hys} = k_h \cdot f \cdot B_c^x \cdot WT_c \tag{5.13}$$

where k_h is a constant depending on the material (typically 0.11), f is the operating frequency, B_c is the core maximum flux density, x is the Steinmetz factor (typically 1.85), and WT_c is the weight of the core.

5.6.2 Eddy Current Loss

The EC resistance for a single lamination is divided into three sections due to the factor L'; hence, the EC loss in the core is also divided into three sections. In each section, the EC loss caused by the EC resistance can be defined as:

$$P_{ec} = \frac{e^2}{R_{ec}} \tag{5.14}$$

where e is the emf across the core components, and R_{ec} is the EC resistance.

Since there is a symmetrical flux distribution between the top section and the bottom section, the EC power loss for the whole core can be represented by twice the power loss from the top (or bottom) section, plus the power loss from the middle section.

Power Loss from Top (or Bottom) Section of the Core

As the flux spreads out at the top section, the remained emf due to the flux going up through direction **'a'** is determined as $e \cdot (1 - K_{ec})$. By applying **Eq:5.14**, the EC power loss in direction **'a'** is:

$$P_{ec\_Ta} = \frac{\left(\frac{e \cdot (1 - K_{ec})}{N_1 \cdot n_{lam}}\right)^2}{R_{ec\_Ta}} \cdot n_{lam} \tag{5.15}$$

where e is the voltage generated by the primary winding, N_1 is the number of winding turns referred to the primary, R_{ec_Ta} is the EC resistance in direction **'a'**, and n_{lam} is the number of core laminations.

In direction **'b'**, since the spreading emf is determined as $e \cdot K_{ec}$, then the EC power loss in this direction is:

$$P_{ec\_Tb} = \frac{\left(\frac{e \cdot K_{ec}}{N_1}\right)^2}{R_{ec\_Tb}} \cdot n_{lam} \tag{5.16}$$

where R_{ec_Tb} is the EC resistance in direction **'b'**.

The emf due to the flux passing through directions **'b'** and **'c'** is the same. However, since there are n_{lam} laminations in direction **'c'**, the emf on each lamination in direction **'c'** is $\frac{e}{n_{lam}}$. Then the EC power loss in direction **'c'** is:

$$P_{ec\_Tc} = \frac{\left(\frac{e \cdot K_{ec}}{N_1 \cdot n_{lam}}\right)^2}{R_{ec\_Tc}} \cdot n_{lam} \tag{5.17}$$

where R_{ec_Tc} is the EC resistance in direction **'c'**.

Power loss from the Middle Section of the Core

Due to the core laminations, the flux travelling through the middle section of the partial core is almost uniform; thus, the developed equation for the uniform flux condition can be directly applied. The EC power loss calculation for the middle section is represented as:

$$P_{ec\_Ma} = \frac{\left(\frac{e}{N_1 \cdot n_{lam}}\right)^2}{R_{ec\_Ma}} \cdot n_{lam} \tag{5.18}$$

where R_{ec_Ma} is the EC resistance in direction **'a'**.

Eddy Current Power Loss Model

The developed EC power loss equations for the **'b'** (or **'c'**) direction can only represent the power loss caused by the flux going through in one direction. Normally, through the graphics produced from the flux simulation software (such as QuickField and MagNet), the spreading flux at the ends of the partial core using the vector presentation can be generally represented as shown in **Figure 5.12(a)**. This presentation for the spreading flux has the same effect with respect to magnitude as the flux going through in one direction, as shown as **Figure 5.12(b)**.

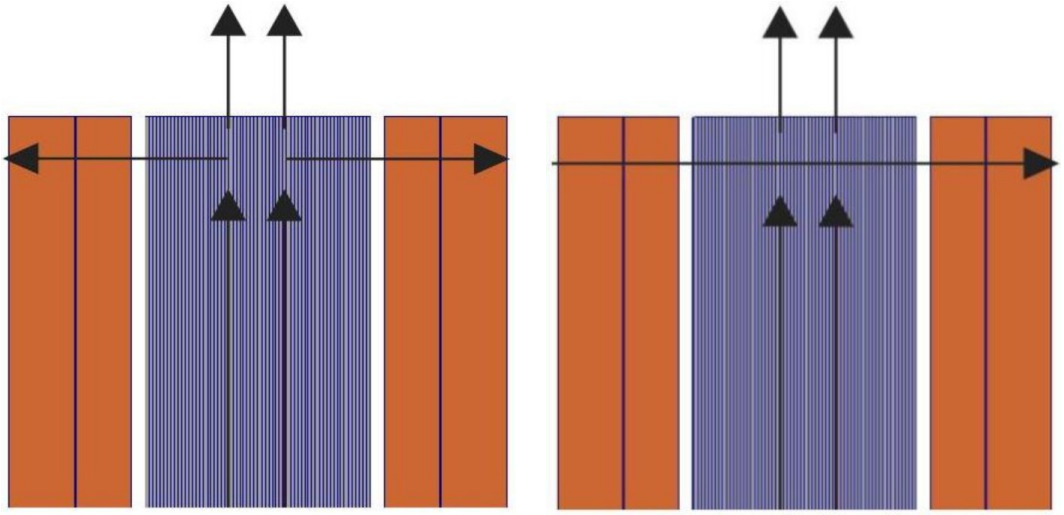

(a) Typical presentation (b) Presentation with equivalent effect

Figure 5.12: Vector presentation of the normalized flux at the end of the cubical partial core.

As an example, the normalized flux presentation side view of three separated laminations of a partial-core transformer has been drawn in **Figure 5.13**. With respect to a single lamination, the flux spreads at the end as shown in **Figure 5.13(a)**. However, over all the laminations the equivalent effect is shown in **Figure 5.13(b)**.

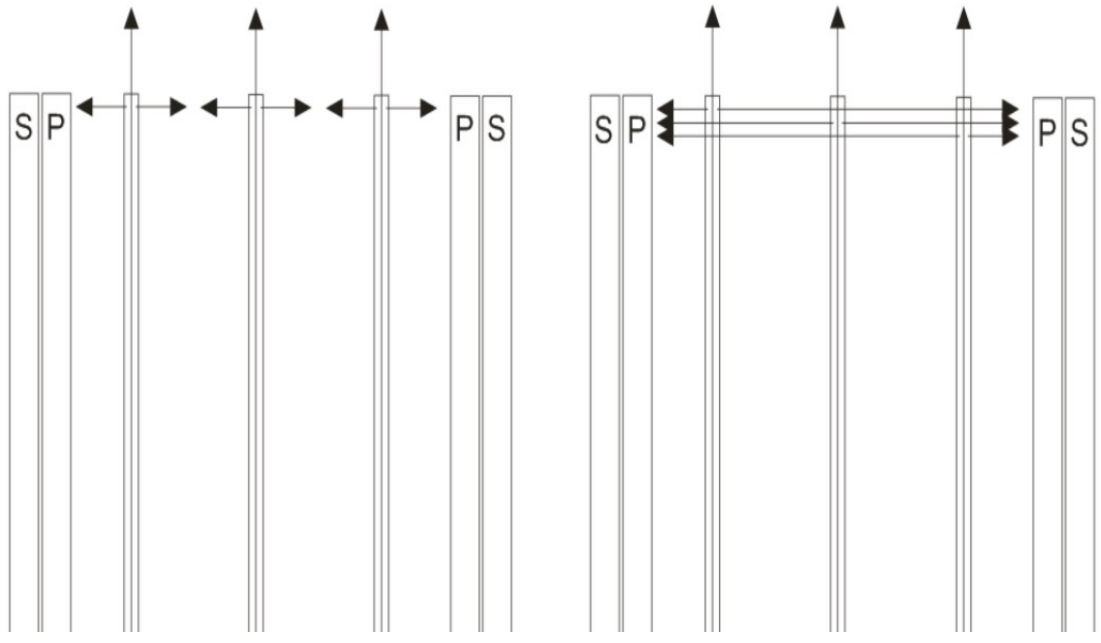

(a) Typical presentation for single lamination (b) Presentation of equivalent effect

Figure 5.13: Normalized flux presentation side view of three separated laminations of a partial-core transformer.

Furthermore, using vector analysis from MagNet, the normalized vectors represent the spreading flux giving a different perspective. **Figure 5.14** shows the normalized flux

vectors for three different core compositions, from MagNet simulations.

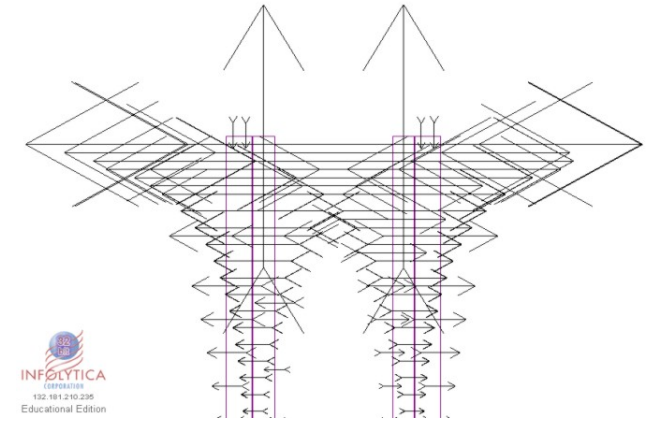

(a) Air core

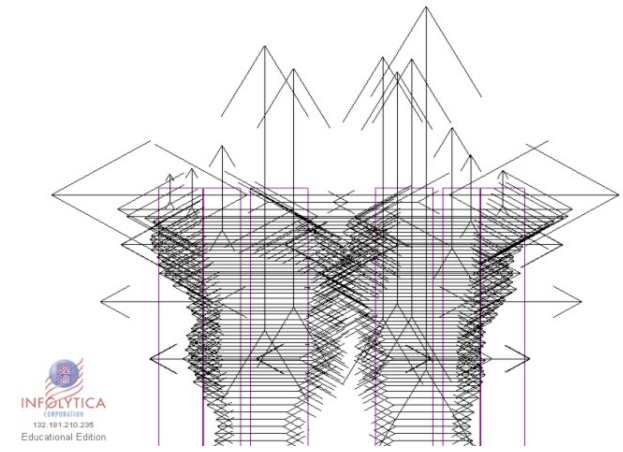

(b) Separated core blocks with space

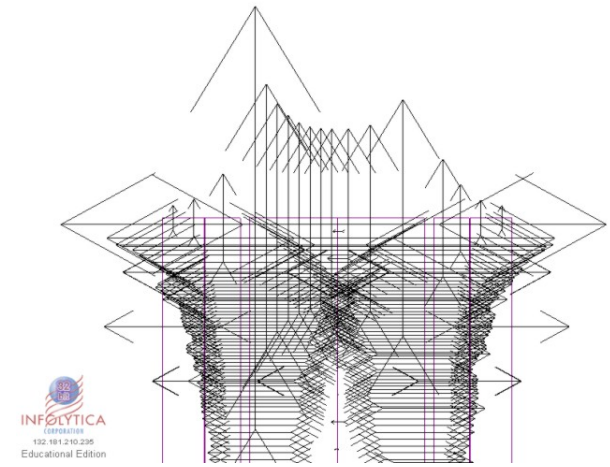

(c) Separated core blocks with no space

Figure 5.14: Normalized flux vectors from the top side with different core compositions.

The size of the arrows (from the head to the tail) in **Figure 5.14** indicates the magnitude of the flux. From the air core to the separated core blocks with no space, there are always some normalized horizontal flux vectors of significant magnitude going across the top in opposite directions. A number of smaller vectors towards the core centre only go across half the side of the core or less, and they do not reach to or cross the other side. Summarizing the effects of the normalized flux arrows from their magnitude and the arrangement at the top section of the core; as an approximation, the equivalent normalized flux presentation is shown as **Figure 5.15**. Hence, the vector presentation of the spreading flux with equivalent magnitude effect can not be represented as **Figure 5.12 (b)**.

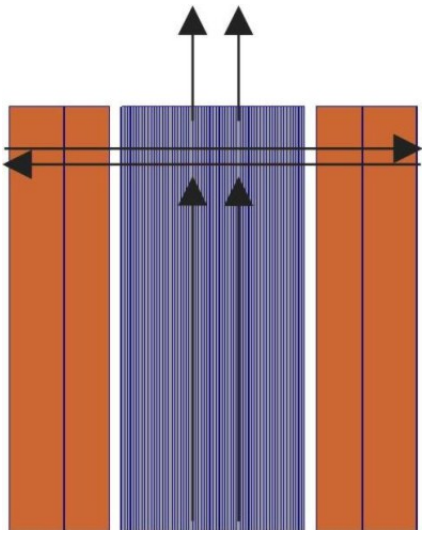

Figure 5.15: Equivalent normalized flux presentation at the end of the cubical partial core.

Due to the spreading flux as shown in **Figure 5.15**, the developed EC power loss equations representing the loss in direction **'b'** (or **'c'**) need to be doubled. Therefore, the EC power loss model for a cubical partial core can be expressed in a 3×3 matrix form by the developed equations:

$$P_{ec} = \begin{bmatrix} 1 & 1 & 1 \end{bmatrix} \cdot \begin{bmatrix} P_{ec\_Ta} & 2P_{ec\_Tb} & 2P_{ec\_Tc} \\ P_{ec\_Ma} & 0 & 0 \\ P_{ec\_Ba} & 2P_{ec\_Bb} & 2P_{ec\_Bc} \end{bmatrix} \cdot \begin{bmatrix} 1 \\ 1 \\ 1 \end{bmatrix} \tag{5.19}$$

The three rows stand for the sections from the top to the bottom, and the three columns stand for the three main directions **'a'**, **'b'** and **'c'**.

The Hysteresis and EC power loss equations for a cubical partial core have been built

up. Because there are 5 cubical partial core transformers with different core and winding sizes, the core losses are different. In order to design a power loss model for a partial core, the relationships among the three key factors is explored in the next section.

5.7 Discussion

The Partial Core (PC) test results from M.C. Liew (Liew, 2001) show that under the same designed voltage ratings, the core losses from PC2, PC4 and PC6 are different. In order to design a power loss model for the partial core, the relationships from the three key factors must be studied.

5.7.1 Between Aspect Ratio and L'

The two factors that define the aspect ratio β_a are l_w and τ_{12}. Therefore, two tests were performed using MagNet to indicate the relationship between β_a and L'.

To change the aspect ratio β_a, l_w is kept constant and the thickness τ_{12} is changed. After testing four PCs (PC1, PC3, PC4 and PC6) using MagNet, the results returned nearly a constant value of L' as a percentage $\left(\frac{L'}{l_c}\right)$ for each partial core as shown as **Figure 5.16**.

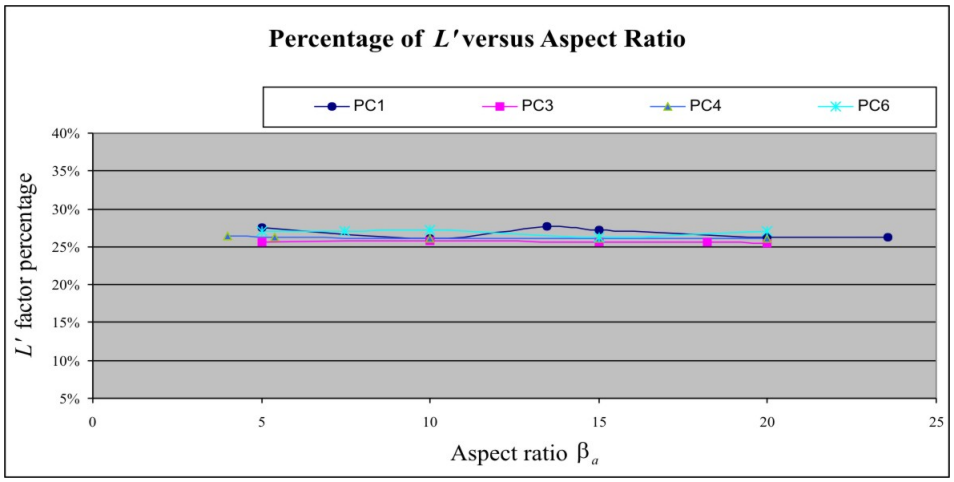

Figure 5.16: A comparison between L' as a percentage of l_c and the aspect ratio β_a.

A constant value from **Figure 5.16** means that the thickness τ_{12} does not affect L'. **Figure 5.17** shows an example of the graphic comparison for PC1 with different winding thicknesses τ_{12}. Although the winding thickness has increased, the region of the spreading flux has not significantly changed.

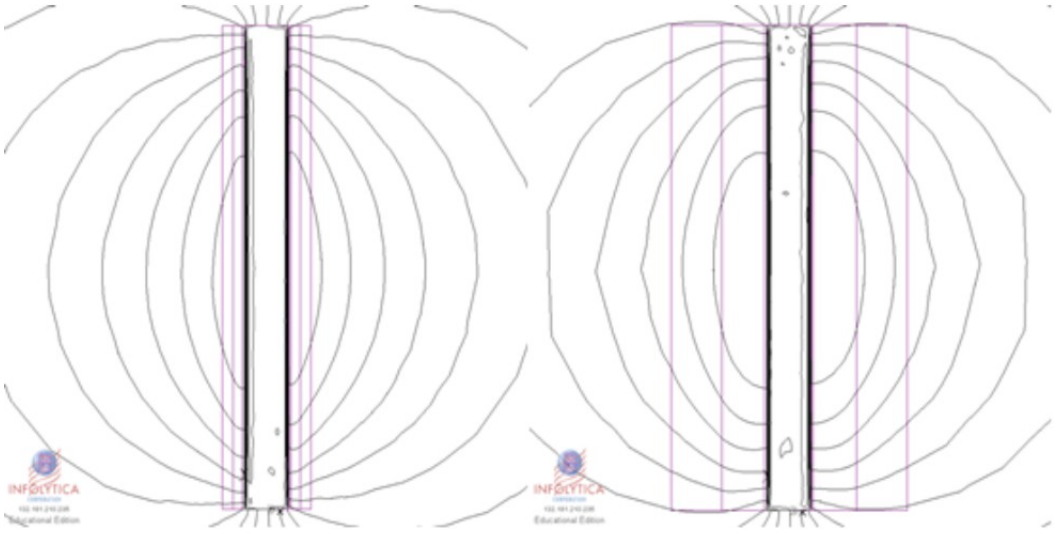

(a) Thin winding thickness (b) Larger winding thickness

Figure 5.17: A flux plot comparison for PC1 with different winding thicknesses.

However, if τ_{12} is kept the same and the winding axial length l_w is changed, then L' as a percentage varies almost linearly as shown as **Figure 5.18**. Hence, the Length Ratio (the ratio between the core length l_c and the winding axial l_w) influences the factor L'.

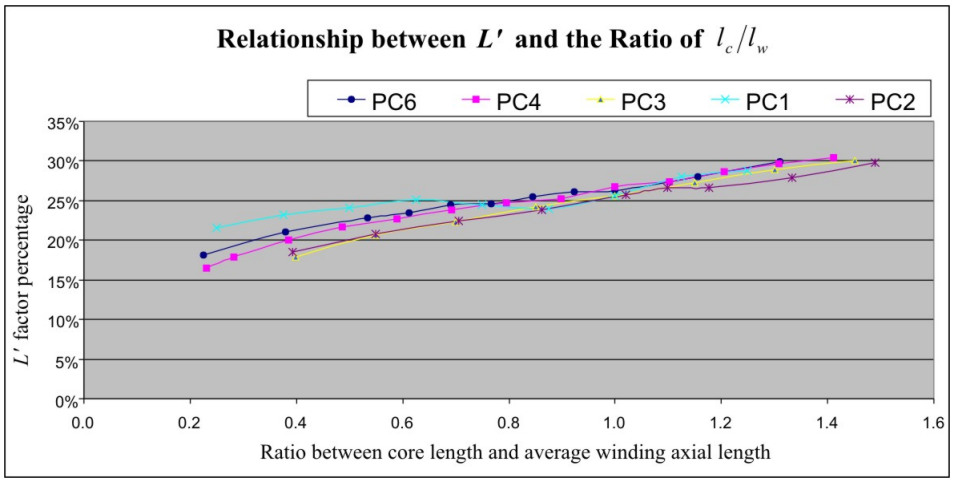

Figure 5.18: Relationship between the L' in percentage and the ratio of $\dfrac{l_c}{l_w}$.

Putting all the data together, **Figure 5.19** shows the linear relationship between L' as a percentage and the Length Ratio. The regression coefficient is $R = 0.94$ for this equation, as a measure of the goodness of fit.

Therefore, the relationship between L' and the ratio of $\dfrac{l_c}{l_w}$ can be expressed as:

$$L' = \left[9.34 \cdot \left(\frac{l_c}{l_w}\right) + 16.83\right] \% \tag{5.20}$$

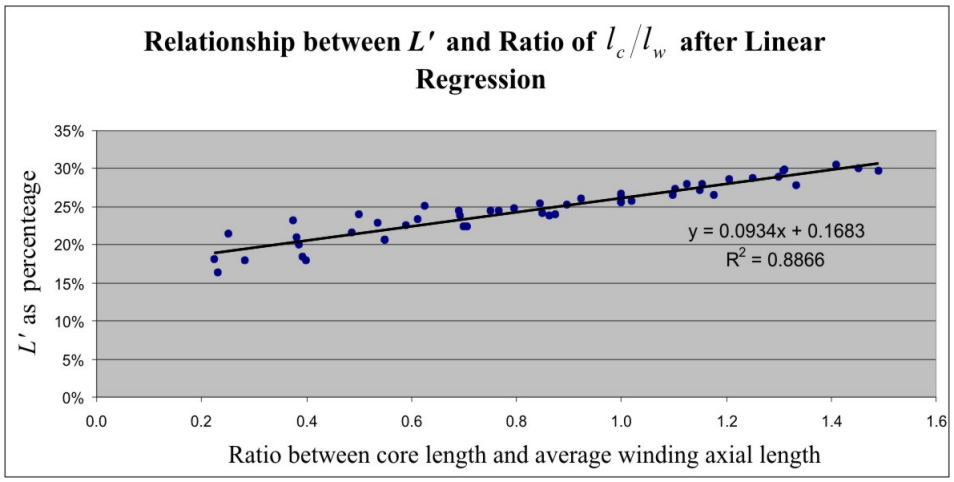

Figure 5.19: Relationship between L' and Ratio of $\frac{l_c}{l_w}$ after linear regression.

5.7.2 Between Aspect Ratio and K_{ec}

As it is difficult to calculate how much the flux spreads out at the end of the core, a spreading factor K_{ec} (which can only be determined through experimentation) has been introduced into the partial core loss modelling. Six cubical core loss models, which now includes PC5, were built in MagNet. By changing the factor K_{ec}, the core losses from the open circuit test results (Liew, 2001) can be matched. **Table 5.2** lists the core losses from each PC and the matching calculation values which give different K_{ec} and aspect ratio values.

	PC1	PC2	PC3	PC4	PC5	PC6
Core losses from experiments (W)	80	183	6	95	160	160
Core losses from calculations (W)	80.2	182.5	6.0	95.1	159.7	160.0
K_{ec}	0.657	0.545	0.758	0.455	0.378	0.447
Aspect ratio β_a	23.56	2.78	18.17	5.40	1.62	7.47

Table 5.2: A comparison between the calculated core losses and the test results with different K_{ec} and aspect ratios for each PC.

From **Table 5.2**, a relationship between the aspect ratio and the factor K_{ec} can be obtained by applying linear regression as shown in **Figure 5.20**.

The regression coefficient R for **Figure 5.20** is about 0.826, which indicates a strong linear correlation between K_{ec} and β_a. Therefore, the factor K_{ec} can be determined as:

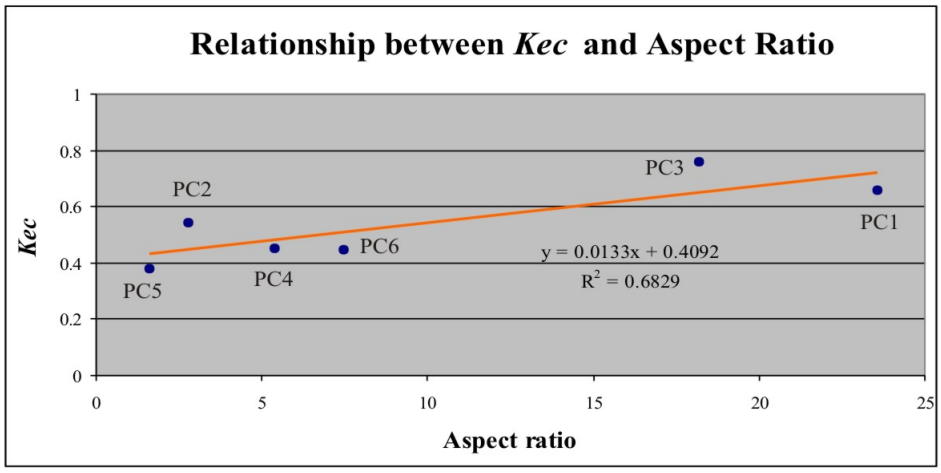

Figure 5.20: Relationship between aspect ratio and factor K_{ec}.

$$K_{ec} = 0.013\beta_a + 0.409 \tag{5.21}$$

The aspect ratio determines the leakage function of the partial core transformer (Liew & Bodger, 2001). As the aspect ratio decreases, the spreading flux though the sides of the core becomes less, which means that the returning flux goes through the ends (top and bottom) rather than the sides of the core. Through the comparisons made in this section, the relationships of the aspect ratio β_a with both L' and K_{ec}, are linear.

5.7.3 Experiment Results

An open circuit test was performed on the cubical partial core transformer PC8. The results showed a 130W power loss at 230V. By putting the data into the derived core loss model, the calculated power loss for PC8 at 230V was 161.3W. If the K_{ec} matching value for PC8 is included in the regression analysis for the relationship between the aspect ratio and the factor K_{ec}, the result changes the coefficients slightly to give

$$K_{ec} = 0.013\beta_a + 0.39 \tag{5.22}$$

The regression coefficient R is changed to 0.805. **Table 5.3** lists the experimental details and the core loss from the derived model.

V_{in} (V)	I_{in} (A)	Power Factor	Experimental power loss(W)	Modelling power loss (W)	Error Percentage
230.8	10.3	0.05	130	155	19%

Table 5.3: Experimental details and the modelling power loss.

The calculated power loss from the derived model shows a 19% deviation from the measured result. For such an inductive device (as indicated by the power factor), the recorded active power for PC8 from the power meter (FLUKE 43B) is comparatively small. However, due to the uncertainties in the power factor measurement, obtained from the manual (± 0.04) (FLUKE Corporation, 2001), a 155W modelling power loss for PC8 is acceptable. Therefore the core loss model and the relationship between the three key factors are verified.

5.8 Conclusion

The flux conditions for a cubical partial core have been reviewed. Three key factors have been introduced to simplify the calculation of the flux conditions of the core. Using simulations from MagNet, a partial core side view with the flux distribution and flux density from two orthogonal angles, was displayed. A flux linkage comparison between the experimental results and the returned values from MagNet verified the high accuracy of the flux plot in MagNet. The EC resistance and power loss models were then built. From the test results, an acceptable core loss model for the cubical partial core transformer has been developed.

Chapter 6

CORE LOSS OF CYLINDRICAL PARTIAL CORE TRANSFORMERS

6.1 Introduction

After building up the core loss model for the cubical partial core transformer in Chapter 5, the three key factors (L', K_{ec} and β_a) were created. The further goal was now to apply the appropriate key factors and build a power loss model for a cylindrical partial core transformer.

Due to the construction differences, a geometry comparison between the cubical and cylindrical core is presented. The spreading flux assumptions for the ends of the cylindrical core are made based on the flux assumptions of cubical core in the Chapter 5. However, between two adjacent blocks, due to the different widths of each block, the flux penetration is different. This is explained.

After creating the cylindrical core loss model (composed of ten blocks), three examples were examined using the developed core loss model. The power loss from the core of one example is visualised by its temperature distribution, which consequently supports the validity of the developed core loss model. An eddy current loss comparison and discussion is made between the previous method and the developed method. Finally, a generic construction form for the core of partial-core transformer is created.

6.2 Background

A cubical core is made by stacking a number of laminations with the same dimensions together as shown in **Figure 6.1(a)**. For a cylindrical core, as shown in **Figure 6.1(b)**, a number of blocks with the same length but different widths and thicknesses are combined together to approximate a circular cross-section. Each rectangular block is similar to a cubical core made of a number of laminations with the same dimensions.

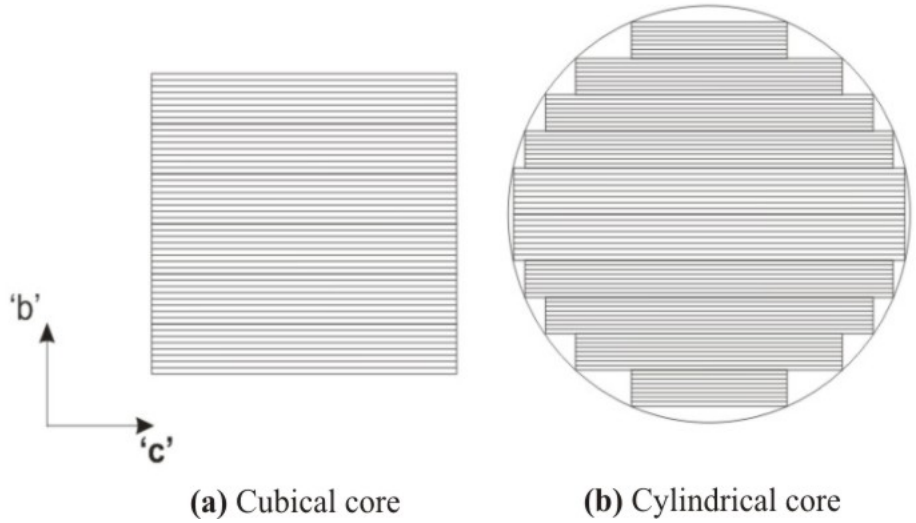

Figure 6.1: Top view of the cubical and cylindrical cores.

It is assumed that the flux goes through the core uniformly, due to the effect of the core laminations. Because each block of the cylindrical core can be regarded as a cubical core, the assumptions made for the cubical core in Chapter 5 can be applied to each single block separately. Therefore, the three key factors L', K_{ec} and β_a, and their relationships, can be applied to the cylindrical core model.

With the different widths and thicknesses from each block, the unchangeable core length and winding thickness lead to a fixed aspect ratio, hence, the K_{ec} for every single block is the same. Overall, for the whole cylindrical core, K_{ec} is the same as for the individual blocks. With the same core length and the winding axial length, L' for the whole cylindrical core is the same for each individual block as well.

The second assumption is that the spreading flux goes through both of the directions **'b'** and **'c'** uniformly. In this case, these spreading fluxes are orthogonal and hence the spreading flux conditions in direction **'b'** and **'c'** for the cylindrical core can be considered

separately.

6.2.1 Flux Assumption in Direction ‘c’

The arrangement of the spreading flux in direction **‘c’** from the top view of the cylindrical core is shown in **Figure 6.2**. The length of each flux vector indicates the magnitude of the spreading flux from each block. The **‘c’** direction is aligned with the direction of the laminations. Hence, the spreading fluxes from the blocks do not affect each other, there is no flux penetration across the blocks, from one block to another.

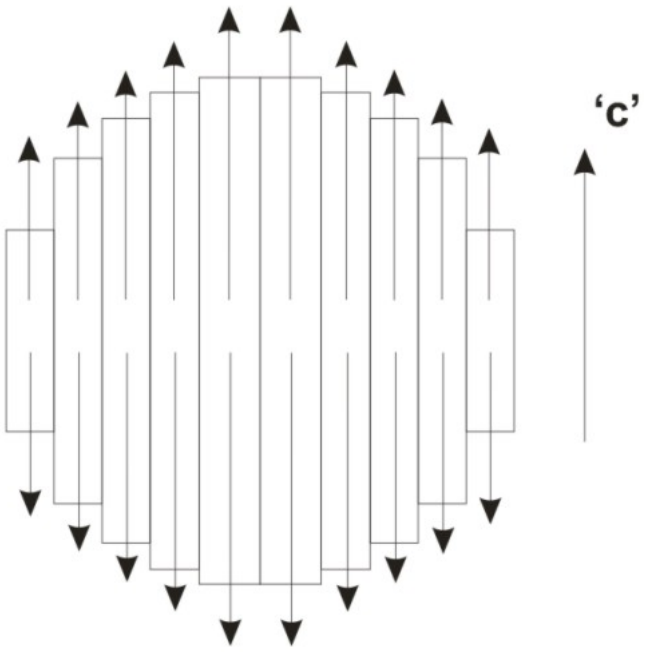

Figure 6.2: Arrangement of the spreading flux in direction **’c’**.

6.2.2 Flux Assumption in Direction ‘b’

Under the uniform flux spreading assumptions for direction **‘b’**, the flux from each block goes in both the positive and negative **‘b’** directions. The effect from each individual block is summarized in **Figure 6.3** which shows the top view of the flux as it spreads across each block from the middle.

As the construction of the core is symmetrical, the block dimensions and the flux distribution are the same for both the upper side and the lower side of **Figure 6.3**. Because of the different widths of each block, when the spreading flux passed from one block to

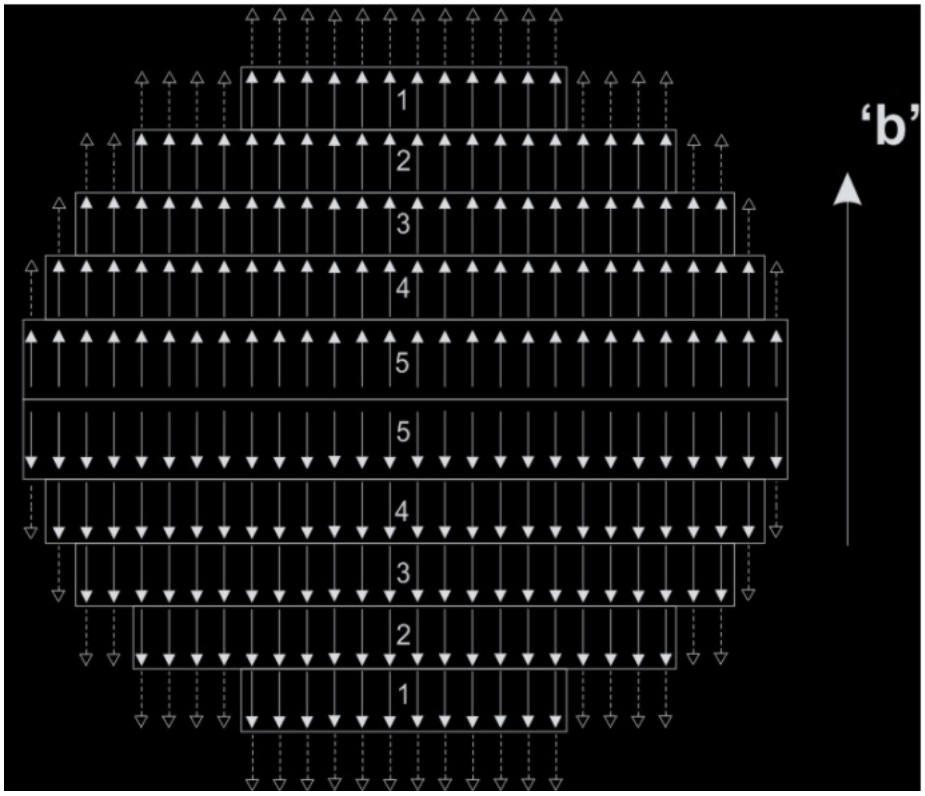

Figure 6.3: Arrangement of the spreading flux in direction **'b'**.

another, not all the flux is entirely passed through. The vectors inside each block represent the self induced spreading fluxes, plus the spreading flux passing through from the block immediately on the inside of it. The hollow arrow heads with dashed tail outside a block display the flux flowing out of the core.

6.2.3 Flux Penetration in Direction 'b'

Figure 6.4 shows an example of flux penetration in direction **'b'** between blocks 5 and 4. Since the flux from block 5 does not pass entirely through block 4, under uniform flux conditions, the flux penetration from block 5 to block 4 can be determined through the spreading area ratio:

$$\frac{\lambda_{5\_b}}{\lambda_{5\_4}} = \frac{A_{5\_b}}{A_{4\_b}} \tag{6.1}$$

where λ_{5_b} is the flux linkage of block 5 in direction **'b'**, λ_{5_4} is the flux linkage from block 5 to block 4 in direcion **'b'**, A_{5_b} is the spreading area from the side of block 5 ($W_5 \times L'$), and A_{4_b} is the spreading area of block 4 ($W_4 \times L'$).

Because the emf is proportional to the flux linkage, then

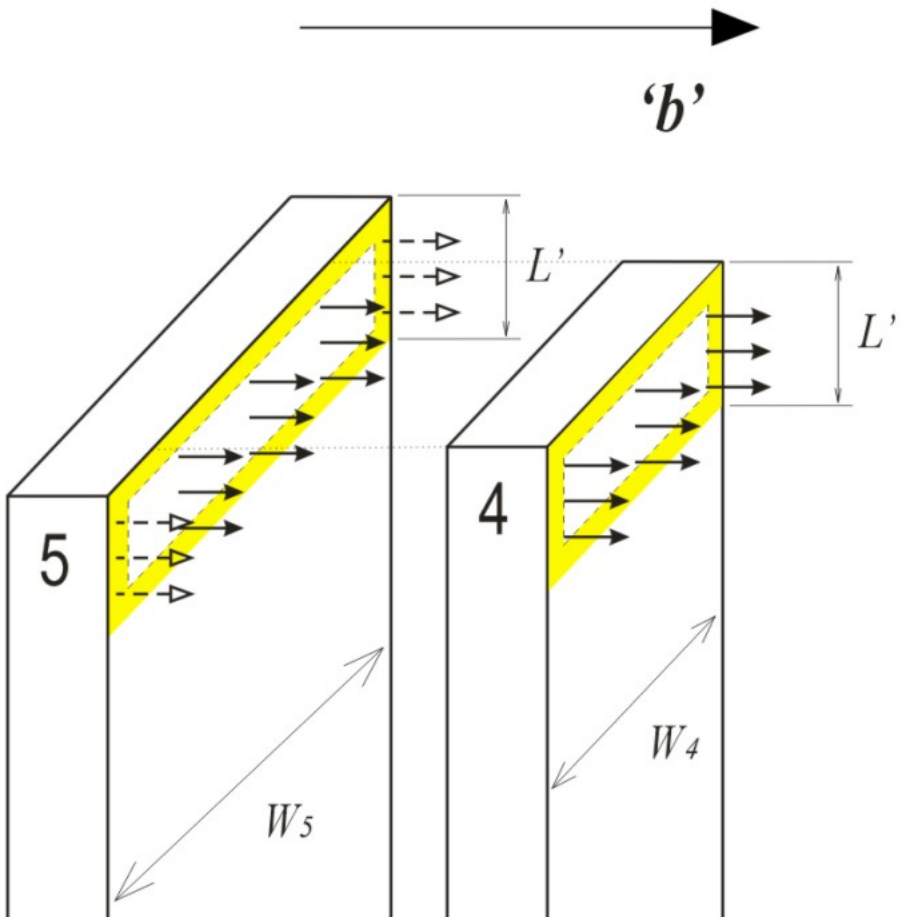

Figure 6.4: Example of the flux penetration between two adjacent blocks .

$$\frac{e_{5\_b}}{e_{5\_4}} = \frac{A_{5\_b}}{A_{4\_b}} \tag{6.2}$$

where e_{5_b} is the induced emf in block 5 in the **'b'** direction ($e_5 \cdot K_{ec}$), and e_{5_4} is the component emf induced in block 4 due to the flux passing from block 5 to block 4.

6.3 Cylindrical Core Loss Model

Due to the different application needs of partial core transformers, the designed core sizes and their composition (such as the number of blocks) are different. A cylindrical partial core with a composition of 10 blocks is shown in **Figure 6.5**. Due to the symmetrical construction of the core, a number from one to five is assigned to every two identical blocks.

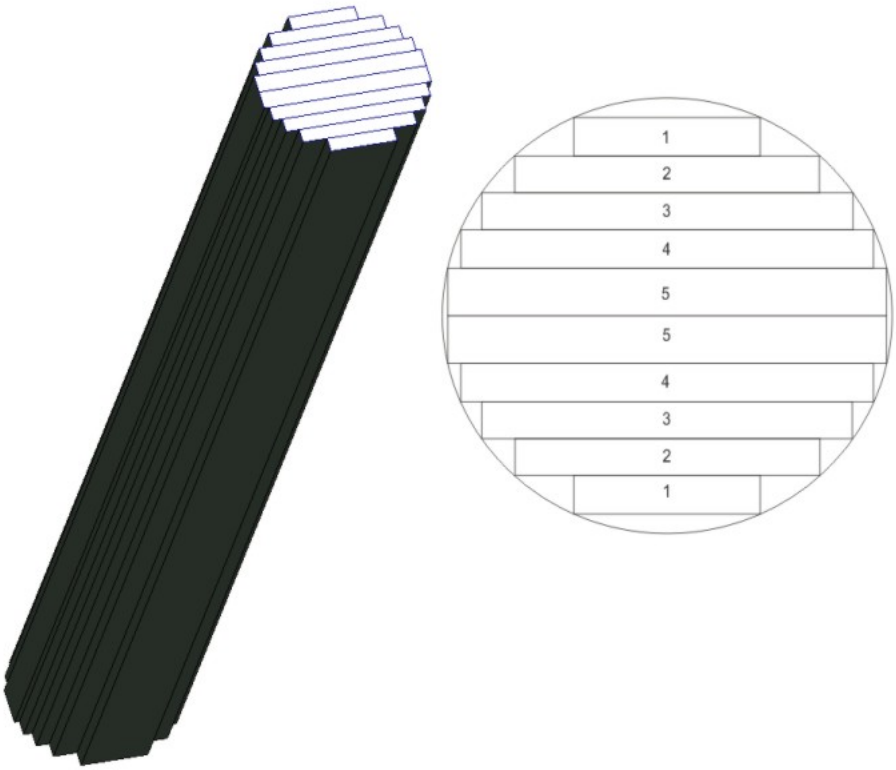

Figure 6.5: A cylindrical core with 10 blocks, and its top view.

6.3.1 Hysteresis Loss

The hysteresis loss for a cubical partial core transformer has previously been defined as:

$$P_h = k_h \cdot f \cdot B_c^x \cdot WT_c \tag{6.3}$$

where k_h is a constant factor depending on the material (typically 0.11), f is the operating frequency, B_c is the core maximum flux density, x is the Steinmetz factor (typically 1.85), and WT_c is the weight of the core. This same formula is used for the calculation of the hysteresis loss of a cylindrical partial core transformer as the expression is independent of the core shape.

6.3.2 Eddy Current Loss

Because the composition of a cylindrical core can be regarded as a number of laminated cubical blocks stacked together, the eddy current loss for the cylindrical core is calculated as the sum of the losses in the cubical blocks.

The different cross sectional areas for each block leads to different flux linkages. A bigger

cross sectional area provides a greater flux linkage under uniform flux conditions. With a linear relationship between the induced emf and the cross sectional area from each block, the emf for each block can be represented by using the total induced emf times the cross sectional area ratio between the block and the cylindrical core:

$$e_n = \frac{A_n}{A_{core}} \cdot e_{total} \tag{6.4}$$

where e_n is the emf induced in the nth block, e_{total} is the emf induced in the entire core, A_n is the cross sectional area for the nth block, and A_{core} is the cross sectional area for the complete cylindrical core.

The three key factors (L', K_{ec} and β_a) stay the same for each block; hence, the eddy current resistance and the power loss model for the cubical core can be applied to each block. As there is a symmetrical construction for the cylindrical core with the 10 blocks as shown as **Figure 6.5**, the eddy current loss model only needs to cover from block 1 to block 5.

Applying **Eq:6.4** to block 5, the induced emf is

$$e_5 = \frac{A_5}{A_{total}} \cdot e_{total} \tag{6.5}$$

Using e_5 and applying the cubical core EC loss model, the EC loss for block 5 is

$$P_{ec5} = \begin{bmatrix} 1 & 1 & 1 \end{bmatrix} \cdot \begin{bmatrix} P_{ec5\_T_a} & 2P_{ec5\_T_b} & 2P_{ec5\_T_c} \\ P_{ec5\_M_a} & 0 & 0 \\ P_{ec5\_B_a} & 2P_{ec5\_B_b} & 2P_{ec5\_B_c} \end{bmatrix} \cdot \begin{bmatrix} 1 \\ 1 \\ 1 \end{bmatrix} \tag{6.6}$$

where the three rows indicate the sections from the top to the bottom, and the three columns indicate the three main directions **'a'**, **'b'** and **'c'**.

For block 4, the induced emf is

$$e_4 = \frac{A_4}{A_{total}} \cdot e_{total} \tag{6.7}$$

Due to the spreading flux penetration from block 5, the emf for block 4 in the **'b'** direction

is

$$e'_{4\_b} = \frac{A_{4\_b}}{A_{5\_b}} \cdot e_{5\_b} + e_4 \cdot K_{ec} \tag{6.8}$$

where A_{4_b} is the spreading area for block 4, A_{5_b} is the spreading area for block 5, and e_{5_b} is the emf induced by the spreading flux from block 5 in direction **'b'**, which is equal to $e_5 \cdot K_{ec}$.

Therefore, in directions **'a'** and **'c'**, the applied emfs for block 4 are $e_4 \cdot (1 - K_{ec})$ and $e_4 \cdot K_{ec}$, but in the **'b'** direction, the total emf for block 4 is e'_{4_b}.

Furthermore for block 3, the emf in directions **'a'** and **'c'** are $e_3 \cdot (1 - K_{ec})$ and $e_3 \cdot K_{ec}$. However, the emf in the **'b'** direction is

$$e'_{3\_b} = \frac{A_{3\_b}}{A_{4\_b}} \cdot e'_{4\_b} + e_3 \cdot K_{ec} \tag{6.9}$$

Due to the flux penetration, the applied emf in the **'b'** direction for block 3 is e'_{3_b} rather than $e_3 \cdot K_{ec}$. Following the same theory, the EC power loss model for the entire core (10 blocks) is expressed as:

$$p_{ec} = 2 \cdot \sum_{k=1}^{5} (P_{eck}) \tag{6.10}$$

The factor 2 in **Eq:6.10** indicates the symmetrical construction of the core, and P_{ec5} to P_{ec1} stand for the eddy current power loss for each block. Overall, the power loss for a cylindrical core consists of the hysteresis loss and the eddy current loss

$$P_{core} = P_h + P_{ec} \tag{6.11}$$

6.4 Example One: Aluminium Winding Partial Core Transformer

The first example looked at the open circuit test result from a partial core transformer proposed by Bodger, P.S, et. al. in 2002 (Bodger et al., 2002a). This transformer was designed as a mock up of a high temperature superconducting transformer. The winding

material was aluminium, and the core was made from laminated silicon steel. From the open circuit test results, there was a major difference between the calculated and measured values for the core loss.

In order to match up the designed dimensions of this partial core, a 14 block core loss model was created. **Table 6.1** gives a comparison between the recorded result (Bodger et al., 2002a) and the value calculated using the new model, for ambient temperature conditions (20 ˚C).

Recorded Results (Bodger et al., 2002a)			Modelling Results	
Calculated Power Loss (W)	Measured Power Loss (W)	Error Percentage	Calculated Power Loss (W)	Error Percentage
114	400	71.5%	358	10.4%

Table 6.1: Comparison between the recorded result (Bodger et al., 2002a) and the modelling result under ambient temperature conditions (20 ˚C).

From consideration of the error percentages for the two calculated values, the new model improves the partial core power loss calculation for this example.

6.5 Example Two: High Voltage Resonating Partial Core Transformer

An open circuit test was performed on a partial core transformer made in 2006 at the University of Canterbury (Tjoa, 2006). This transformer, shown as **Figure 6.6,** was designed to charge up a capacitor bank which supplies a high voltage for long arc research. The voltage ratio for this transformer is 230V to 20kV. The core construction contains 16 blocks which are correspondingly symmetrical on each side.

A partial core power loss model composed of 16 blocks was built up for this core. **Table 6.2** lists the records from the open circuit test, compared to the new core loss model calculations. A power meter FLUKE 43B (FLUKE Corporation, 2001) was used to obtain the input voltage, current, power and power factor. The output voltage was monitored using a FLUKE 41B (FLUKE Corporation, 1995). For the FLUKE 43B, because the power measurement function automatically changes the range from Watts to kilo-Watts, the two decimal places displayed under the kilo Watts unit range was not accurate enough for

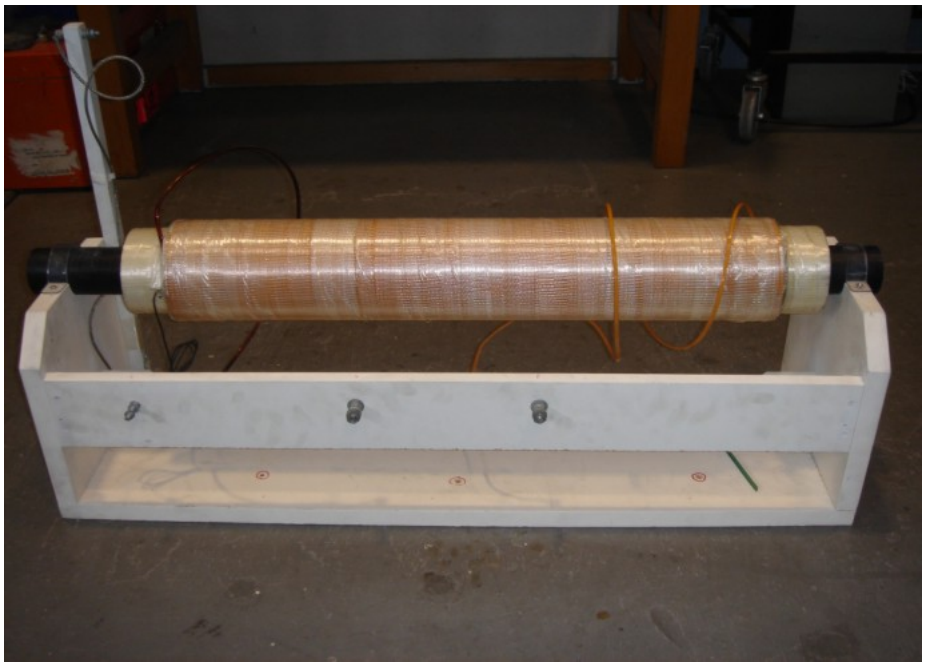

Figure 6.6: High voltage partial core transformer.

such a small power loss. Hence, the measured power loss was represented as a calculated value, $V_{in} \cdot I_{in} \cdot pf$, in **Table 6.2**.

V_{in} (V)	I_{in} (A)	V_{out}(kV)	pf	Power Measurement (W)	Power Calculation (W)	Error Percentage
30.62	2.03	2.94	0.06	3.73	5	28%
60.60	4.00	5.74	0.06	14.54	18	22%
90.20	5.95	8.51	0.06	32.20	38	18%
120.10	7.95	11.33	0.06	57.29	66	15%
150.30	10.02	14.25	0.06	90.36	102	13%
180.60	12.15	17.18	0.06	131.66	147	12%
210.90	15.06	20.14	0.06	190.57	208	9%
231.00	18.35	22.10	0.06	254.33	272	7%

Table 6.2: Comparison between the open circuit test results and the new core loss model calculations.

There is a low accuracy issue for the power meter operating at low voltages; hence, the higher error percentages than at higher voltages. **Figure 6.7** shows the calculated and the measured power loss.

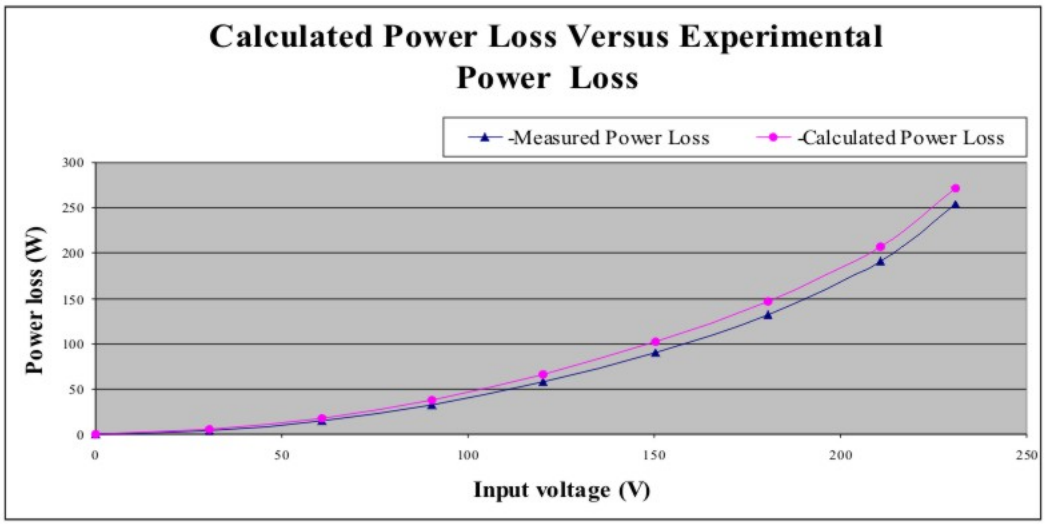

Figure 6.7: Comparison between the computational power loss and the experimental power loss.

The two curves are in reasonable agreement. This result supports the viability of the developed core loss calculation method.

6.6 Example Three: Mock-up Copper Winding Partial Core Transformer

A partial core transformer, as a second mock up of a superconducting transformer (MPCTF) (Poole, 2000), was built in 2004 at the University of Canterbury. With a designed 1:1 turns ratio between the primary and the secondary, the material used 3.5mm thick round copper wire for both windings. The core material was silicon steel and the lamination thickness was 0.5mm. The former was built up of two tubes with a space between. The tube space can be made a vacuum to provide heat insulation of the core from the windings. **Figure 6.8** shows the MPCTF and its core. (The details is given in **Appendix 8**)

6.6.1 Temperature Monitoring Test

The partial core power loss caused by eddy currents can be expressed as a heat loss. Heat represents a form of energy transferred from a system at one temperature to another at a lower temperature (Eastop & Mcconkey, 1986). Hence, as the representation of the heat transfer, the temperature distribution can indicate where the most power loss occurs in

Figure 6.8: Pictures of the MPCTF and its core.

the core. In order to determine the heat generated in the partial core, three temperature sensors and a thermal imager (FLUKE Ti20) (FLUKE Corporation, 2006b) were used to monitor and visualize the temperature distribution on the surface of the core.

A 40 hour temperature monitoring test for the MPCTF was performed under open circuit conditions. The three temperature sensors were attached with heat sink compound onto the core surface at the top, centre and bottom of the core. **Figure 6.9** shows the temperature variation with time for the three positions on the core surface, under open circuit test conditions. During the period, the temperature was sampled every 3 seconds. The open circuit condition (230V on the primary) was run for 24 hours (86400 seconds). The large ripple of the curves was caused by vibration from the core during the operation. After switching off the power, the ripples, and the temperature, for the three positions dramatically decreased. From **Figure 6.9**, the highest temperature was from the middle section, and the lowest temperature was from the top section.

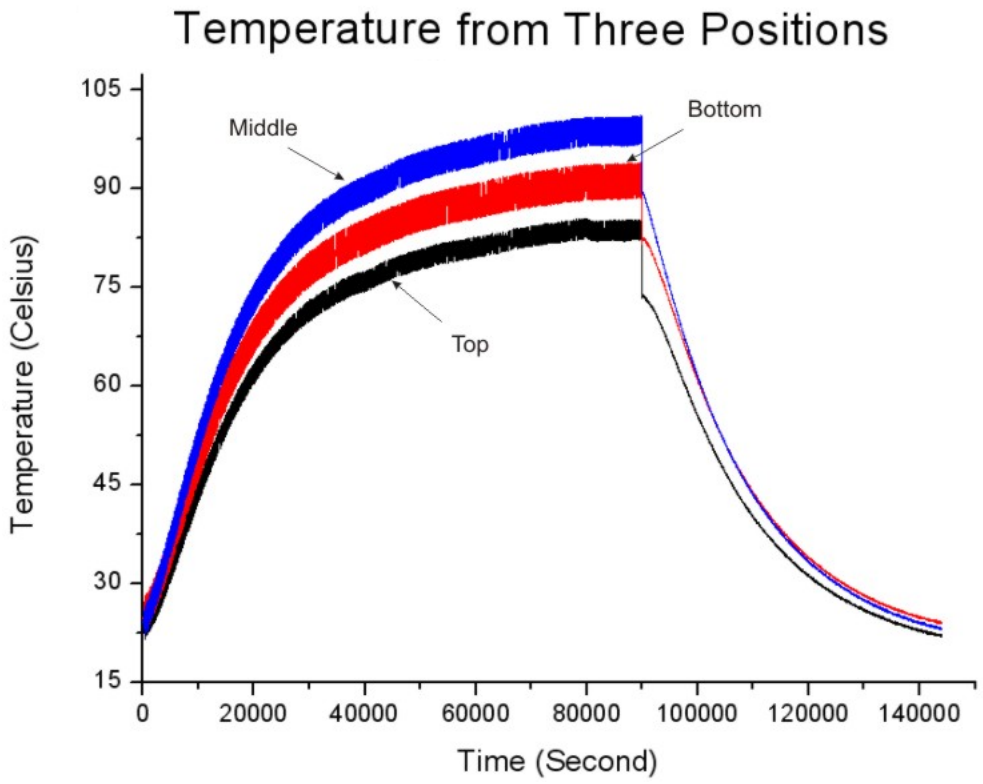

Figure 6.9: Temperature variation with time for the three positions on the core under open circuit test conditions.

Figure 6.10 shows a thermal image of the core, which was briefly extracted from the windings during the open circuit test. From the luminosity and temperature scale, the image correlates with the three temperature curves of **Figure 6.9**.

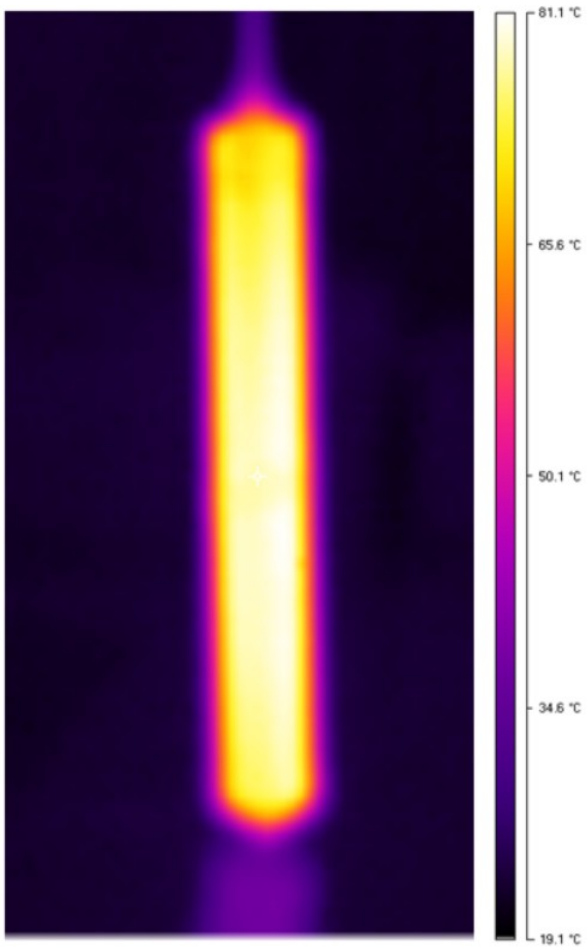

Figure 6.10: Thermal image of the core during the open circuit test.

From the new partial core power loss model, the most power loss should come from the top and bottom sections through direction **'b'**. However, the temperatures from both **Figure 6.9** and **Figure 6.10** indicate that the major power loss appears to occur in the middle section of the core, which is opposite to that assumed for the new model. Three reasons can explain what was observed.

First, due to the high thermal conductivity of the silicon steel, the heat transfer inside the core is relatively fast. Consequently, it is difficult to know where the generated heat comes from. Secondly, the results from the temperature sensors in **Figure 6.9** are affected by heat transfer from the winding at the start of the experiment. **Figure 6.11** shows the higher temperature of the winding relative to the temperature of the middle section of the core surface. Thirdly, the core is enclosed inside the former which has only one end open at the top. This means that heat more easily dissipates from the top of the core than from the middle or bottom.

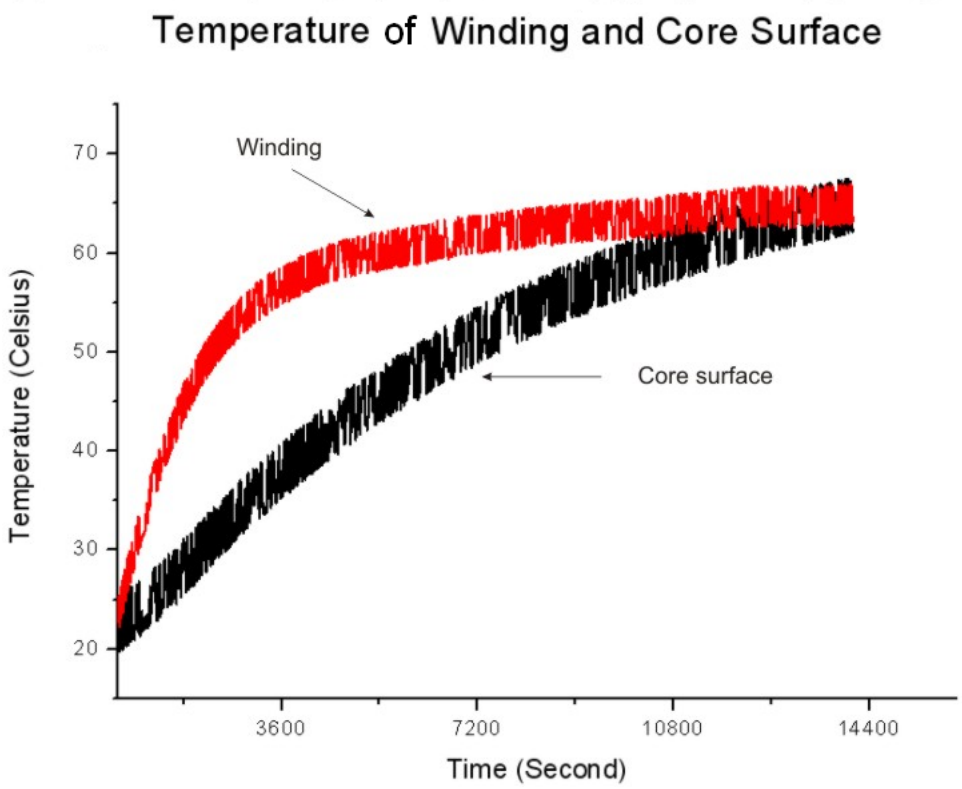

Figure 6.11: Temperature of winding and the core surface.

In order to isolate the core heating effect from the influence of the winding, the inside of the former is a vacuum chamber. Under these conditions, the heat transfer from the winding should be reduced to nearly adiabatic. However, due to the chamber being small, and incomplete vacuum conditions, the rest molecules inside the chamber can still pass heat from the winding to the core. The vacuum condition in the chamber only inhibits the temperatures from the winding to the core by 10˚C, which fails its function.

6.6.2 Core Sectionalisation

The positions of the three temperature sensors were changed to the top, 6cm below the top, and 12cm below the top of the core. As shown in **Figure 6.12**, the temperature at 12cm below the top was lower than the temperature at 6cm below the top during the heating up process. This implies that the heat generation in the core might not come from the middle section.

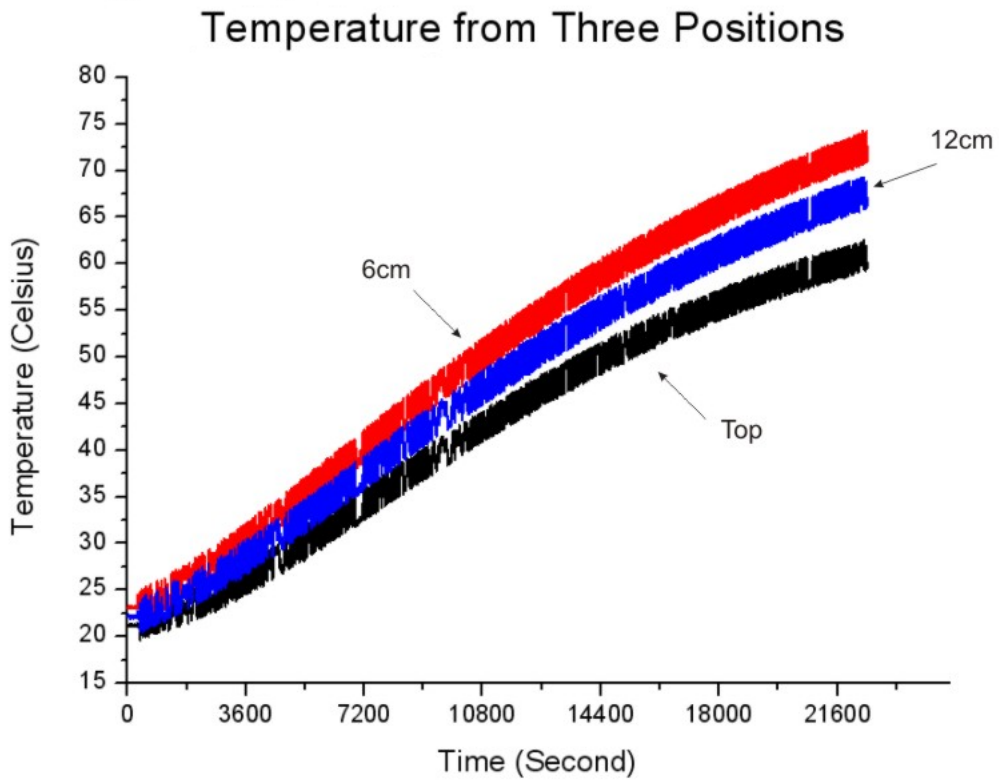

Figure 6.12: Temperature variation for three positions from the top of the core.

In order to investigate the distribution of heat loss from the core further, the core was cut using a water jet into eight sections, as shown as **Figure 6.13**.

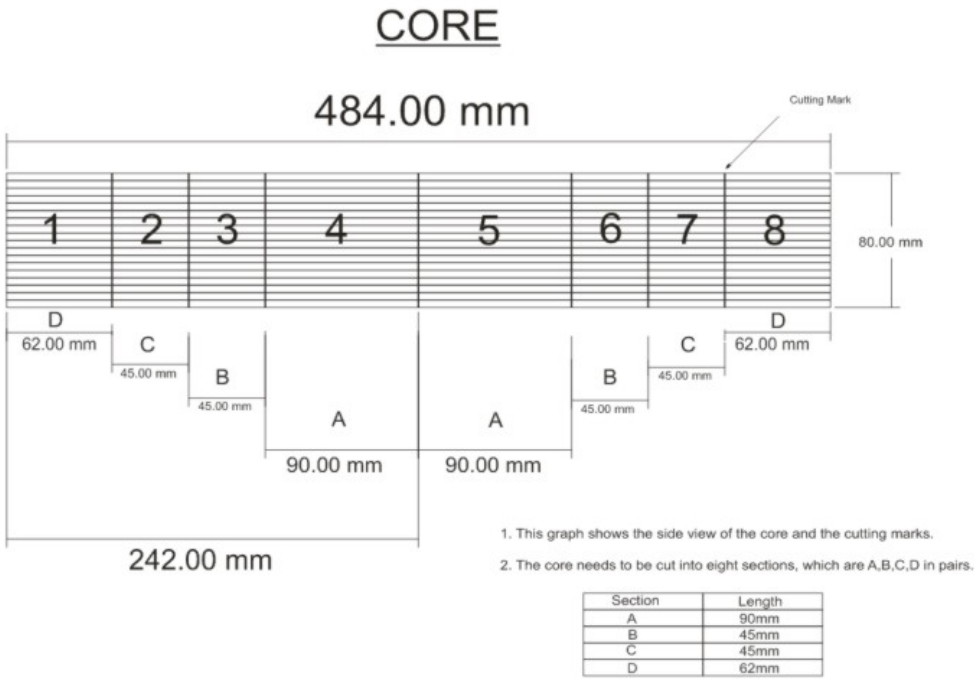

Figure 6.13: The dimensions of the core sections from the side view.

After cutting, the open circuit test for MPCTF was performed again using the same power

meter (FLUKE 41B-FA33 (**FLUKE Corporation, 1995**)) to check for any differences the cuts made. **Table 6.3** compares the results from the open circuit test before and after the cuts.

	In July 2007 (before cutting)	In May 2009 (after cutting)
$R_{winding}$ (Ω)	0.224	0.246
V_{in} (V)	230	230
I_{in} (A)	20	22.5
Power Loss (kW)	0.2	0.2
V_{out} (V)	228	228

Table 6.3: Comparison of the open circuit test results before and after the core was sectionalized.

The power loss from the open circuit test is the sum of the winding loss, the hystersis loss and the eddy current loss. The increases after the cut are in the input current and the winding resistance. The winding resistance increase was caused by the different resistance meter used after two years. With these changes, the winding power loss increases about 21.5W. However, the measurement range from the FLUKE 41B was auto-scaled to kilo Watts during the test, and such a minor change (21.5W) under the kilo Watts scale did not change the measured value. Therefore, the core power loss before and after the cuts is determined as unchanged.

6.6.3 Heat Distribution

A core with length of 270mm was obtained as shown in **Figure 6.14(a)** with a combination of sections 2, 3, 4, 6, and 7. An open circuit test was performed for five minutes. **Figure 6.14(b)** shows a thermal image of the core after the test.

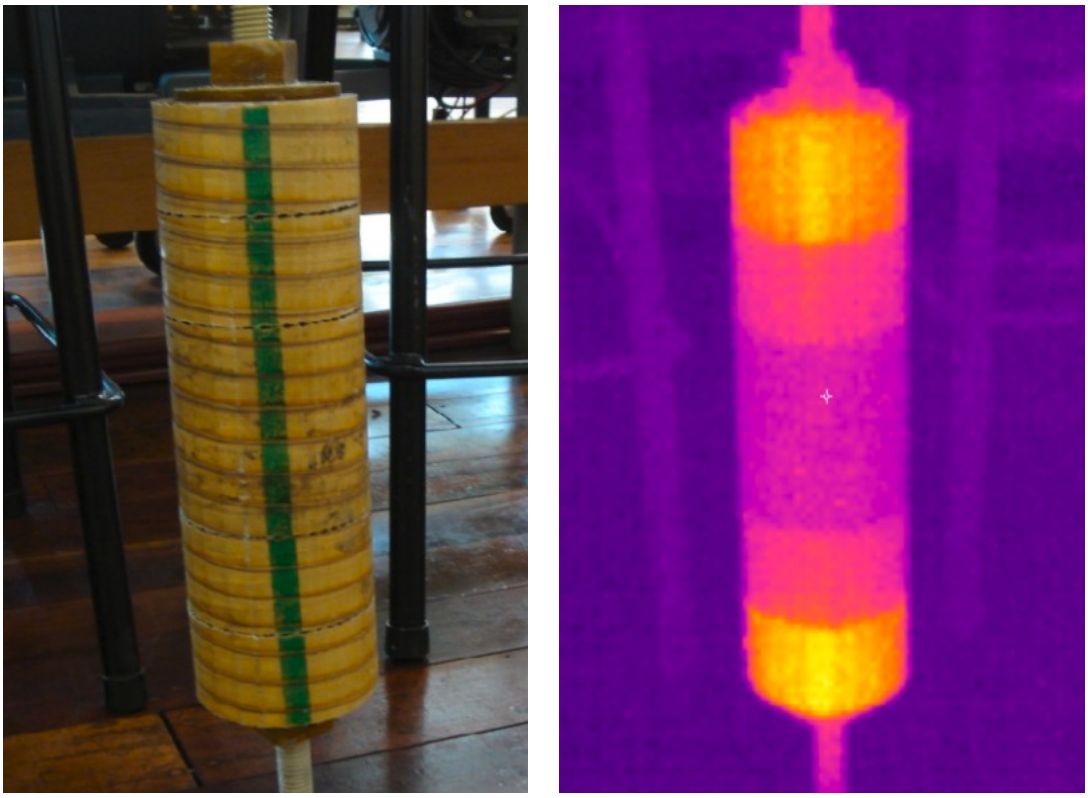

(a) 270mm core (b) Thermal image of the core

Figure 6.14: The 270mm core and its thermal image.

The winding axial length is about 405mm, which can fully cover the 270mm core after locating the core in the axial-middle of the windings. During the open circuit test, the higher temperature winding starts to heat up the core. However, the heating conditions are all the same for each section, as they are all covered by the windings. For a short running time, the temperature of the core is not affected by heat from the windings. The luminosity from **Figure 6.14(b)** shows a lower temperature in the middle of the core and higher temperatures towards the ends. This verifies that most of the heat produced is in the ends of the core rather than the centre.

A further open circuit test was performed on a 360mm core (a combination of sections 2, 3, 4, 5, 6, and 7). The experiment was conducted over eight time periods, with each period running for 10 minutes at rated voltage (230V). With accurate temperature measurements up to 350˚C, the thermal Imager Ti20 (FLUKE Corporation, 2006b) was used to monitor the surface temperature variation from each section at the end of each period. **Figure 6.15** shows a 3-D column chart representing the temperature rise in each section during the open circuit test.

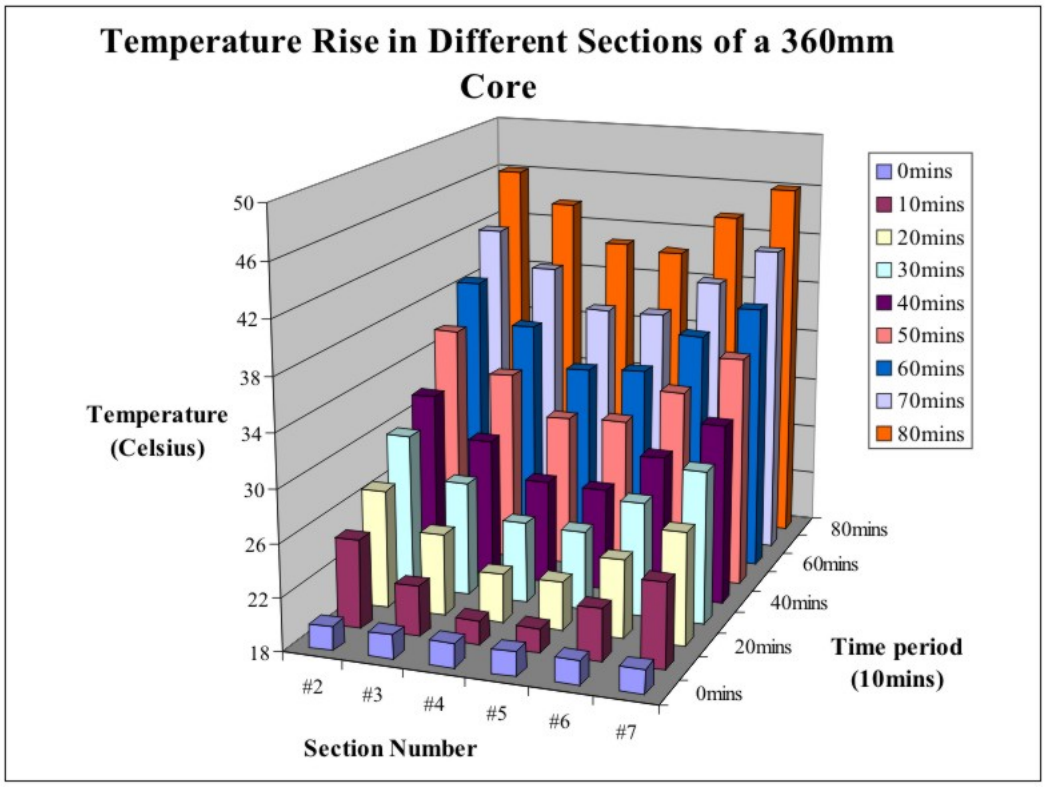

Figure 6.15: A 3-D column chart representation of the temperature rise in each section.

Before the cuts, with a high thermal conductivity, the heat transfer inside the core was relatively fast. Hence, the thermal image from **Figure 6.10** can not indicate the effect from the eddy currents at both ends. After the cuts, with the temperature increasing slower in the middle but faster at both ends, as in **Figure 6.15**, the appropriateness of the key factors (L' and K_{ec}) in the design and the orthogonal flux assumptions for the new core loss model has been supported.

6.6.4 Open Circuit Test with Core Length Variation

As the core has been cut into eight sections, a set of open circuit tests were performed by varying the core length with different sectional combinations (including 484mm, 422mm, 394mm, 360mm, 315mm, 304mm, and 270mm). In order to get comparable results, three power meters, FLUKE 41B, FLUKE 43B, and FLUKE 434 (FLUKE Corporation, 2006a), were used to monitor this experiment. **Table 6.4** lists the open circuit test results obtained from the FLUKE 43B for seven core length combinations.

As the core length is reduced, the current and real power losses increase. There is a small change in the power factor. Due to the unchanged parameters (input voltage, fre-

Core Length (mm)	V_{in} (V)	I_{in} (A)	Real Power (kW)	Power Factor
484	230.0	22.1	0.24	0.05
422	230.0	26.1	0.31	0.05
394	230.1	29.1	0.38	0.06
360	229.7	32.8	0.45	0.06
315	230.2	39.8	0.62	0.07
304	230.2	42.7	0.72	0.07
270	230.3	50.1	0.93	0.08

Table 6.4: Open circuit test results for seven core length combinations obtained from the FLUKE 43B.

quency, winding numbers and across sectional area), according to the transformer equation (**Eq:3.2**), the flux density should be constant (even if the core length is reduced). Hence, for the same flux linkage ($L \cdot i = \lambda$), the increased input current means the inductance decreases and the winding power loss rises.

Winding Resistance Variation with Temperature

A high current flowing through the winding produces more real power losses and hence heat. This heat raises the winding temperature and effectively increases the winding resistivity **(Davies, 1990)**:

$$\rho = (1 + \triangle\ \rho(T - T_0)) \cdot \rho_{20^\circ C} \tag{6.12}$$

where $\rho_{20^\circ C}$ is the electrical resistivity of the material at 20˚C, T is the temperature, T_0 is the reference temperature, 20˚C, and $\triangle\ \rho$ is the thermal resistivity coefficient.

Hence, the resistance of the winding is:

$$R = \frac{l}{A} \cdot (1 + \triangle\ \rho(T - T_0)) \cdot \rho_{20^\circ C} \tag{6.13}$$

From the short circuit test of the MPCTF, the winding temperature was measured against the increasing input current, as shown as **Figure 6.16**. A corresponding winding temperature for each input current level from **Table 6.4** can thus be estimated.

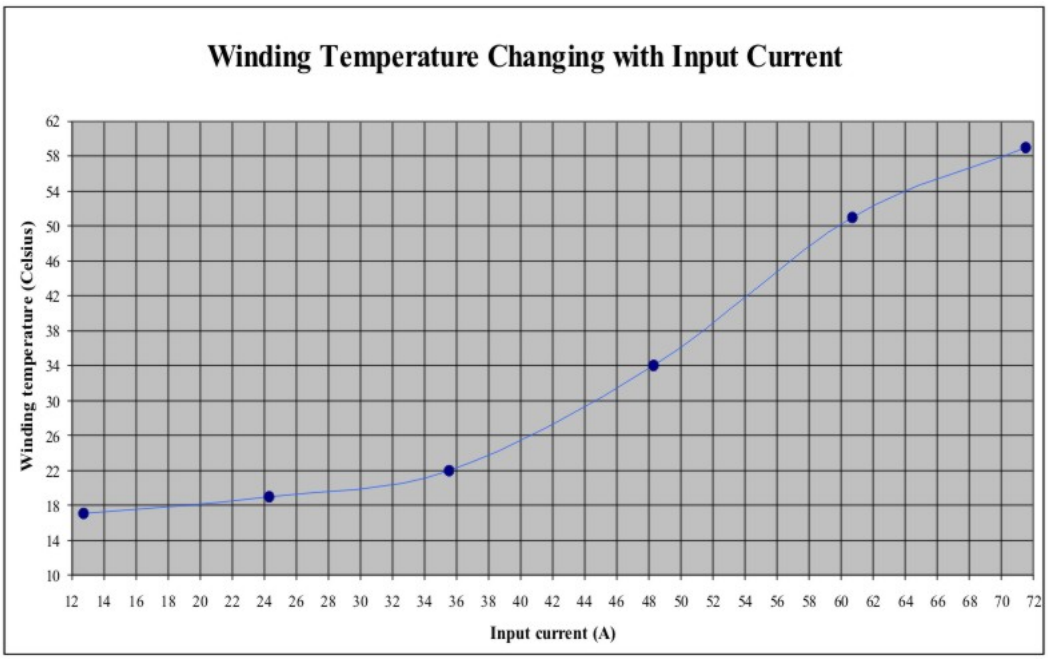

Figure 6.16: Winding temperature variation with input current for the MPCTF.

The winding resistance was measured as 0.244Ω using Micro-Ohmmeter MPH254, at 15˚C. By knowing the temperature of the winding, the winding resistance and the winding power loss can be recalculated under the different current levels (current data from FLUKE 43B) as shown as **Table 6.5**.

I_{in} (A)	$T_{winding}$ (˚C)	$R_{winding}$ (Ω)	Pwinding (W) Caused by temperature effect
22.1	18.5	0.250	122
26.1	19.5	0.251	171
29.1	20.0	0.252	213
32.8	20.8	0.254	273
39.8	25.5	0.262	415
42.7	28.0	0.266	484
50.1	36.1	0.280	703

Table 6.5: Winding power loss due to temperature variation.

The effect of the resistance variation is fairly small when the winding temperature is under 20˚C. Nevertheless, for a high input current, this effect must be considered.

Test Result

In order to match up the designed dimensions of the core, an 18 block core loss model was created (Model details are given in **Appendix 8**). The real power loss is the sum of the core power loss and the winding power loss. By applying the new core loss model and taking the winding temperature variation into account, a comparison of the real power loss from the experimental results and the calculated values can be made, as shown in **Figure 6.17**. The upper error band and the lower error band were calculated from the product $V_{in} \cdot I_{in} \cdot pf$, using the power factor uncertainties from each power meter.

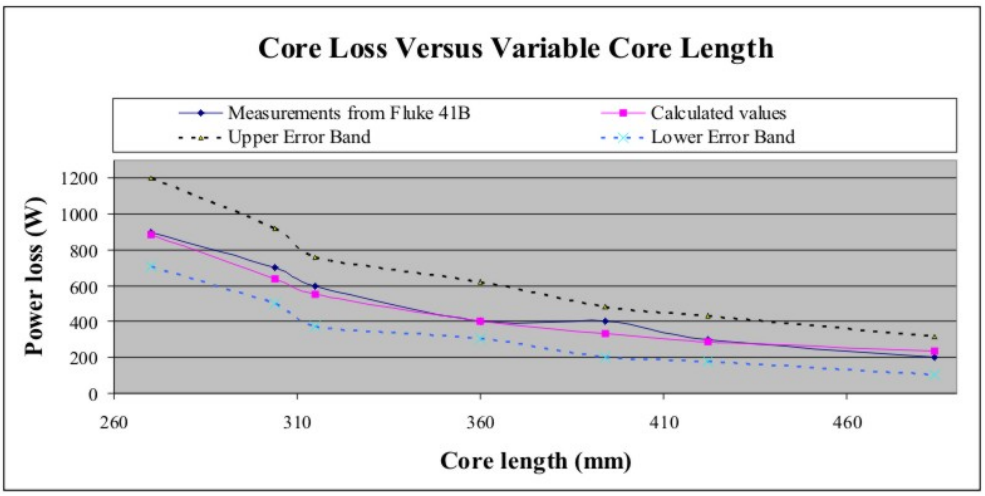

(a) Comparing with FLUKE 41B

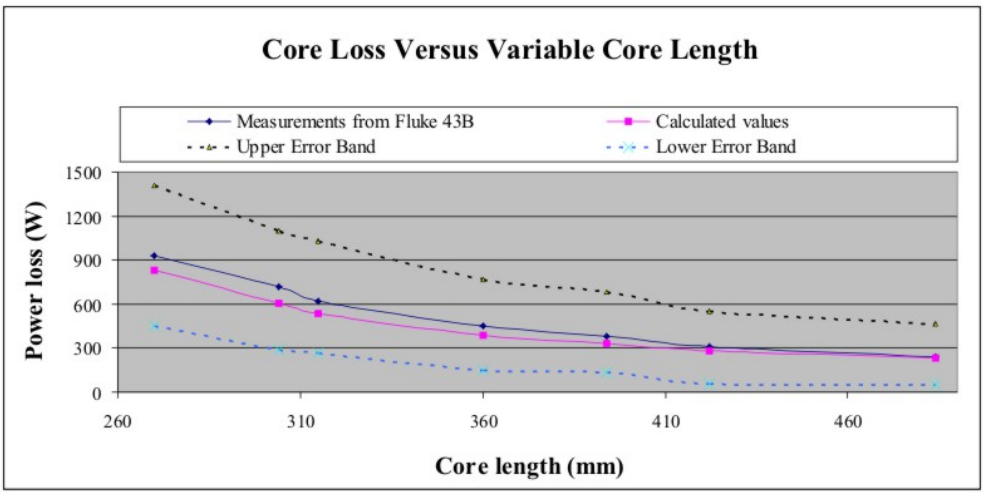

(b) Comparing with FLUKE 43B

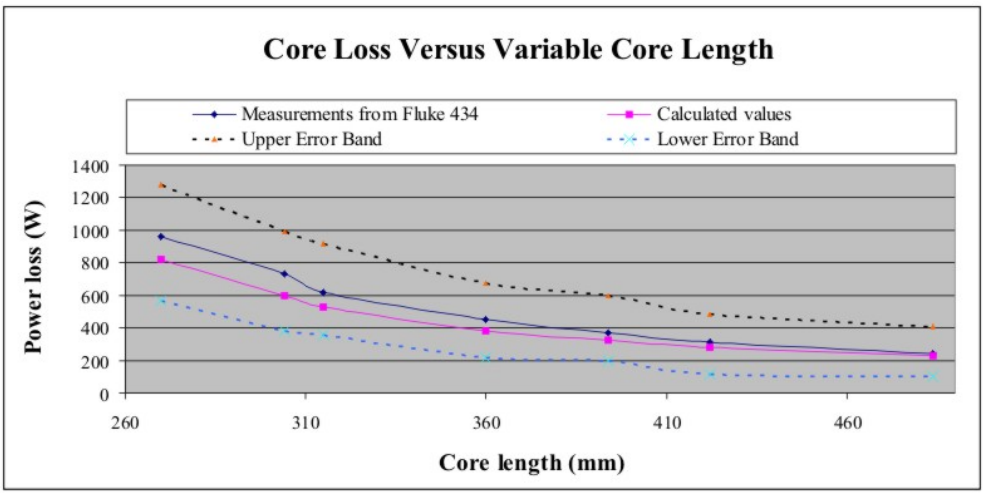

(c) Comparing with FLUKE 434

Figure 6.17: Power loss comparison between the experimental results using three power meters and the calculated values.

From **Figure 6.17**, the calculated values and the experimental results are relatively close. The calculated values are within the error bands of the instrument measurements.

6.7 Discussion

The previous eddy current power loss equation for transformer cores is expressed as **(Slemon, 1966)**:

$$P_{ec} = \frac{c_1^2}{12\rho_c} \cdot \frac{l_c}{N_1^2 \cdot A_c} \cdot e_1^2 \tag{6.14}$$

where

$c_1 =$ lamination thickness

$\rho_c =$ operating resistivity of the core

$A_c =$ cross sectional area of the core

$e_1 =$ induced primary winding voltage

$N_1 =$ primary winding turns

$l_c =$ length of the core

This equation has been used to calculate the eddy current power loss for both full core and partial core transformers. A comparison of the eddy current loss calculations between applying **Eq:6.14** and the new **Eq:6.10** can be made. The data used from the open circuit test with varying core length was measured using the FLUKE 43B power meter. **Table 6.6** and **Table 6.7** list the EC loss calculations using **Eq:6.14** and **Eq:6.10**, and gives a total power loss comparison between experimental results and calculated values.

Core Length (mm)	Calculated EC Power Loss (W) **Eq:6.14**	Calculated Hysteresis Loss (W)	$P_{winding}$ (W)	Calculated total power loss (W)	Measured Power (kW)	Error percentage
484	1.38	42.4	122.1	166	0.24	31%
422	1.20	37.0	171.4	210	0.31	32%
394	1.12	34.4	213.1	249	0.38	35%
360	1.02	31.5	272.6	305	0.45	32%
315	0.90	27.6	415.0	444	0.62	29%
304	0.86	26.5	483.9	511	0.72	29%
270	0.77	23.6	703.1	727	0.93	22%

Table 6.6: EC loss calculation using **Eq:6.14** and the total power loss compared to experimental results.

Core Length (mm)	Calculated EC Power Loss (W) **Eq:6.10**	Calculated Hysteresis Loss (W)	$P_{winding}$ (W)	Calculated total power loss (W)	Measured Power (kW)	Error percentage
484	67.0	42.4	122.1	231	0.24	4%
422	75.7	37.0	171.4	284	0.31	8%
394	80.2	34.4	213.6	328	0.38	14%
360	85.9	31.5	272.6	390	0.45	13%
315	95.3	27.6	415.0	538	0.62	13%
304	97.8	26.5	483.9	608	0.72	16%
270	106.0	23.6	703.1	833	0.93	10%

Table 6.7: EC loss calculation using **Eq:6.10** and the total power loss compared to experimental results.

The calculated total power loss using **Eq:6.14** for the eddy current loss has a larger percent error as compared with the total power loss calculated using the new **Eq:6.10**. The eddy current loss calculation for the partial core using the new core loss model is thus a considerable improvement over the previous model.

6.8 A Generic Form of the Partial-core Transformer Core

The new core loss model is constructed using blocks. Hence, a generic form based on the number of blocks needs to be created for the partial-core design. The net cross sectional

area ($A_c^{'}$) of the core occupied by the magnetic material is less than its gross cross sectional area (A_c). The ratio of the net cross sectional area and gross cross sectional area is determined as the Stacking Factor (SF)

$$SF = \frac{A_c^{'}}{A_c} \tag{6.15}$$

A core construction that allows a stacking factor of a typical level ($SF \geq 0.96$) is shown in **Figure 6.18**.

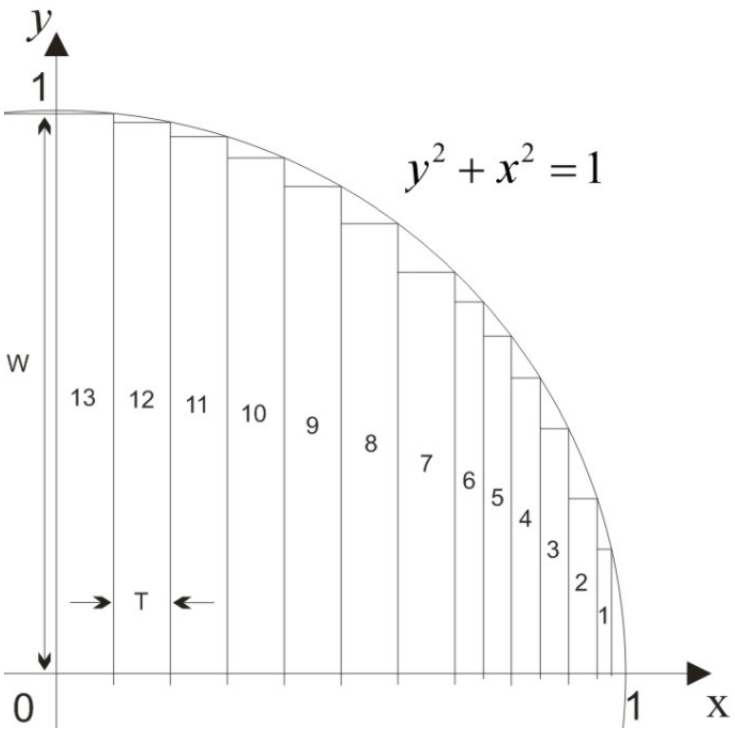

Figure 6.18: Top view of a quarter of a partial core.

The radius of the core was normalized to unity, and 13 blocks were created for a quarter circle. In order to achieve the typical level of stacking factor, the thickness T for each block from 7 to 13 was chosen as 1/10 of the radius, from 2 to 6, chosen as 1/20 of the radius, and for block 1, chosen as 1/40 of the radius. The width W for each block can be determined using $y^2+x^2 = radius$. The stacking factor for this general form is calculated as 0.961, which satisfies the inequality. The new core loss model can be applied to this generic arrangement.

6.9 Conclusion

The geometry and construction differences between the cubical core and the cylindrical core have been compared. The orthogonal flux assumptions for the cylindrical core through two directions **'b'** and **'c'** have been reviewed. The flux penetration between two adjacent blocks in the cylindrical core has been studied, and a cylindrical core loss model has been created. Using experimental results, the validity of the new core loss model has been verified, and a visualization of the core loss, as represented by its temperature distribution, has been presented. An eddy current power loss comparison has been made between the previous model **Eq:6.14** and the new model method **Eq:6.10**. The results confirm that there is a significant improvement using the new core loss model. A generic form of the partial core can be used for designing future models of partial core transformers which have a stacking factor greater than 0.96.

Chapter 7

DISCUSSION: PARTIAL CORE DESIGN FOR LOSS REDUCTION

With the intention of improving the efficiency of a partial core transformer, reducing the core losses is one of the options. The eddy current loss can be reduced by varying the dimensions of the laminations. Applying the different orientated laminations to the core can reduce the eddy current loss in the core. Another option is using a different material to manufacture the transformer core such as amorphous steel, which reduces both of the eddy current loss and the hysteresis loss.

7.1 Changing the Lamination Dimensions

For a single cubical block with a parallel oriented lamination construction, keeping the number of laminations constant keeps the voltage distribution unchanged in each lamination under uniform flux conditions. **Table 7.1** lists the qualitative affects of varying the lamination geometry on eddy current resistance and power loss analysed using the developed model.

$l_{core} \uparrow$			
$R_{ec\_Ta} \downarrow$	$R_{ec\_Tb} \uparrow$	$R_{ec\_Tc} \uparrow$	$R_{ec\_Ma} \downarrow$
$P_{ec\_Ta} \uparrow$	$P_{ec\_Tb} \downarrow$	$P_{ec\_Tc} \downarrow$	$P_{ec\_Ma} \uparrow$
$W \uparrow$			
$R_{ec\_Ta} \uparrow$	$R_{ec\_Tb} \uparrow$	$R_{ec\_Tc} \downarrow$	$R_{ec\_Ma} \uparrow$
$P_{ec\_Ta} \downarrow$	$P_{ec\_Tb} \downarrow$	$P_{ec\_Tc} \uparrow$	$P_{ec\_Ma} \downarrow$
$T_{core}(\leq 2\delta) \uparrow$			
$R_{ec\_Ta} \downarrow$	$R_{ec\_Tb} \downarrow$	$R_{ec\_Tc} \downarrow$	$R_{ec\_Ma} \downarrow$
$P_{ec\_Ta} \uparrow$	$P_{ec\_Tb} \uparrow$	$P_{ec\_Tc} \uparrow$	$P_{ec\_Ma} \uparrow$

Table 7.1: Qualitative eddy current loss effects by varying lamination geometry.

The first three columns of **Table 7.1** indicate the eddy current loss in three directions in the top section of the core, and the fourth column shows the eddy current loss due to flux in the direction **'a'** in the middle section. An up arrow indicates an increase in a parameter, while a down arrow indicates a decrease.

As the lamination length increases, the eddy current resistance drops down in direction **'a'**, but rises in directions **'b'** and **'c'**. Thus the eddy current power loss only increases in direction **'a'** and drops down in directions **'b'** and **'c'**. The width increase makes the eddy current resistance drop in direction **'c'**, and leads to an eddy current power loss increase in this direction. The increase in lamination thickness reduces the eddy current resistance in three directions and increases the power loss in each direction.

Hence, the results indicate two ways to reduce the eddy current loss in most sections, which are increasing the width (W) and reducing the thickness (T_{core}) of the laminations. In practice increasing the lamination width is not realistic, but reducing the lamination thickness can be an option.

7.2 Using Different Core Lamination Constructions

Parallel oriented laminations and radially oriented laminations as shown in **Figure 7.1 (Bell, 2008)** are two constructions used to manufacture the core of partial core transformer.

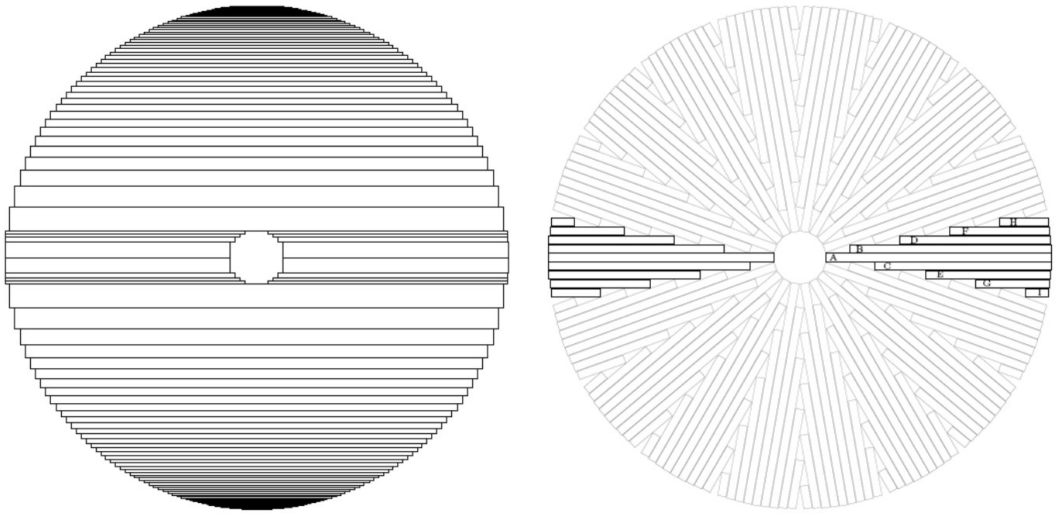

(a) Parallel oriented laminations (b) Radially oriented laminations

Figure 7.1: Two types of lamination orientation(Bell, 2008).

The parallel oriented construction is easier to manufacture than the radially oriented construction. Therefore, the most common structure for a transformer core is the parallel oriented construction. This also gives a higher stacking factor.

However, the heat generated in the core caused by eddy currents is greater for the parallel oriented lamination construction than for the radially oriented core laminations. Because the flux spreads radially from the ends of the partial core, the thin laminations with the radial construction reduce the eddy current loss in each piece. Consequently, for core loss reduction, the radially oriented construction generates much less heat than the parallel oriented construction.

7.2.1 A Proposal of Eddy Current Loss Model for Radially Oriented Laminations

The developed core loss method can be applied to the radially oriented partial core to calculate the core losses. The radially oriented construction shown in **Figure 7.1(b)**, has 18 identical sector shaped blocks (as one of two highlighted). Each sector shaped block combines 9 bundles as ‘A’, ‘B’, ‘C’, ‘D’, ‘E’, ‘F’, ‘G’, ‘H’, ‘I’. Each bundle can be regarded as a cubical core. However, instead of using **‘a’**, **‘b’**, and **‘c’** representing the three directions for the spreading flux, two directions **‘a’** and **‘r’** can be used for each bundle in the radially oriented core. Direction **‘a’** indicates the direction along the axis

of the core, and direction **'r'** stands for the radial direction of spreading flux, where it is assumed that the spreading flux uniformly passes through each bundled block as shown as **Figure 7.2**.

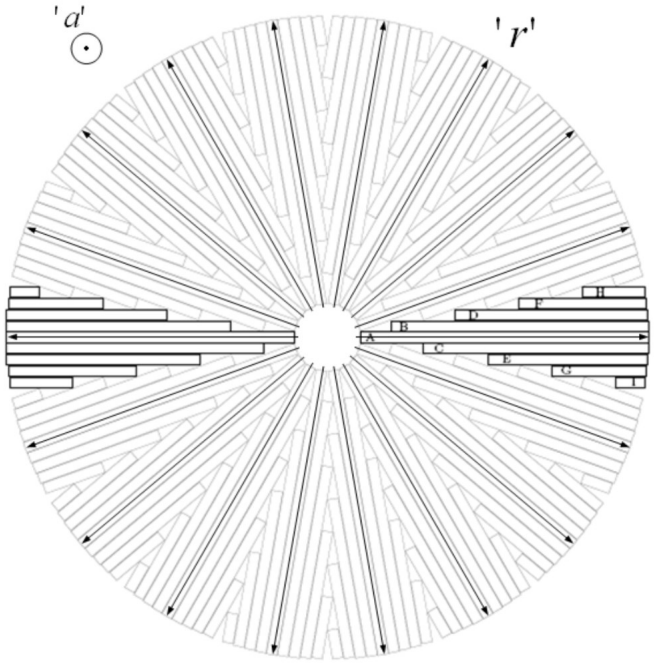

Figure 7.2: Top view of the radially oriented partial core.

Hence, for the radially oriented construction, the eddy current loss equation for a single bundle is changed to

$$P_{ec} = \begin{bmatrix} 1 & 1 & 1 \end{bmatrix} \cdot \begin{bmatrix} P_{ec\_Ta} & 2P_{ec\_Tr} \\ P_{ec\_Ma} & 0 \\ P_{ec\_Ba} & 2P_{ec\_Br} \end{bmatrix} \cdot \begin{bmatrix} 1 \\ 1 \end{bmatrix} \tag{7.1}$$

The three rows indicate the three sections as top, middle, and bottom. The two columns represent the two directions **'a'** and **'r'** in **Figure 7.2**. For one highlighted sector (the 9 bundles from 'A' to 'I'), the eddy current loss equation is

$$P_{EC\_sector} = P_{ec\_A} + P_{ec\_B} + P_{ec\_C} + \cdots + P_{ec\_I} \tag{7.2}$$

The eddy current loss for the entire core is

$$P_{EC} = 9 \cdot P_{EC\_sector} \tag{7.3}$$

The core loss model for a radially oriented core construction can be verified by experiment. With identical physical sizes and materials, a power loss comparison between the two constructions, to determine how much the power loss is reduced by the radially oriented construction can then be made.

7.3 Combined Parallel and Radially Oriented Laminations for Partial Core Construction

The radially oriented construction for the partial core mainly reduces the eddy current loss caused by the spreading flux at both ends. Instead of manufacturing the complete core with a radially oriented construction, a combination between parallel and radially oriented core constructions could be manufactured, as shown in **Figure 7.3**.

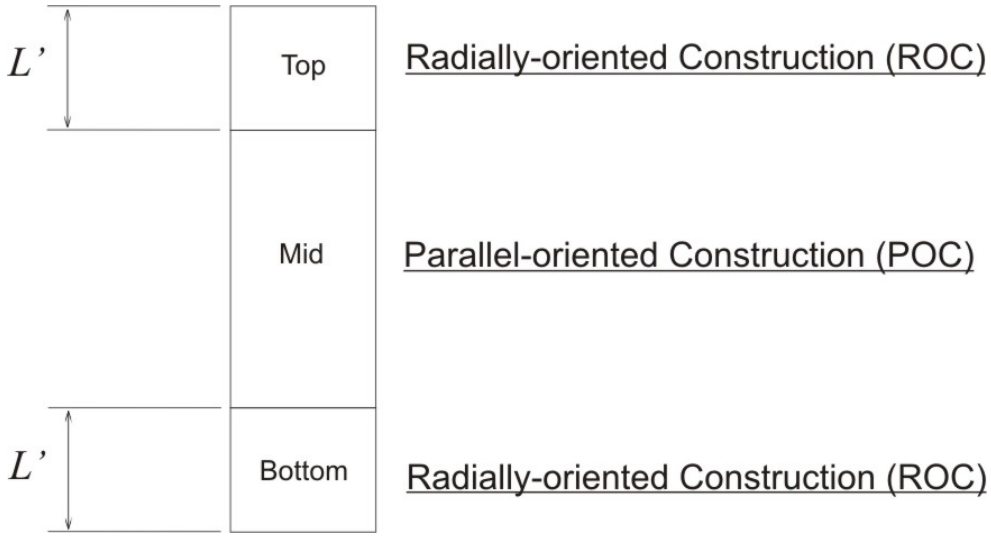

Figure 7.3: Side view of a combined partial core construction.

The top and bottom sections could be made identical with an axial length of L' using the radially oriented construction. The middle section can be a parallel oriented construction since there is almost no spreading flux flowing in that section. The cross sectional view of the partial core transformer that combines parallel and radially oriented laminations for partial core construction is shown in **Figure 7.4**.

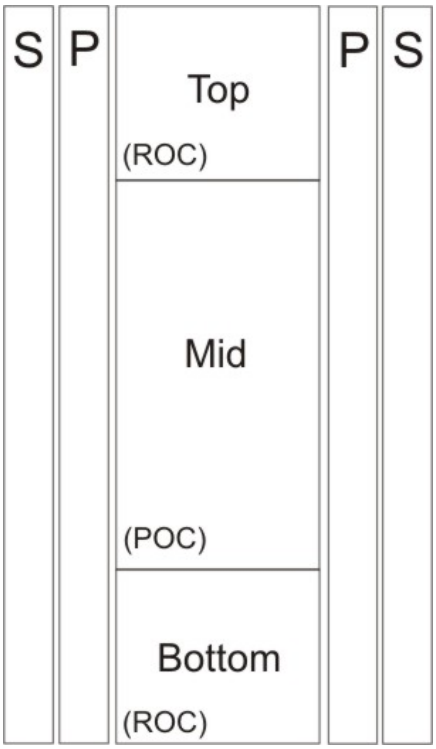

Figure 7.4: Configuration of proposed partial core transformer.

where P and S stand for the primary and the secondary windings.

7.4 Using Amorphous Steel

Amorphous steel is a metallic glass annealed to red heat temperatures, rolled to a specified thickness (0.025mm), then rapidly cooled on a rotating wheel (1,000,000 ˚C/sec) (Unknown, 2009). The result gives a random atomic structure which offers a large increase in resistivity. **Table 7.2** gives a comparison of properties between amorphous steel and CRGO silicon steel (Unknown, 2009).

Properties	Unit	Amorphous Steel	CRGO Silicon Steel
Density	$(^{g}/_{cm^3})$	7.15	7.65
Specific resistance		130	45
Saturation flux density	(Tesla)	1.56	2.03
Typical core loss (at 50 Hz, 1.4 Tesla)	$(^{Watt}/_{kg})$	0.2	0.9
Thickness	(mm)	0.025	0.27
Brittleness		Higher	Lower
Available form		Ribbon/Foil	Sheet/Roll
Annealing temperature	(˚C)	360	810
Annealing atmosphere		Inert gas	Inert gas
Special annealing requirement		Magnetic field annealing	-

Table 7.2: Typical properties of amorphous steel and CRGO steel (Unknown, 2009).

Full core transformers using different core materials (silicon steel and amorphous steel) have been compared using open circuit and short circuit tests in (Bodger et al., 2002b). There was significant core loss reduction when using amorphous steel as the core material, as the amorphous steel gives less hysteresis losses and eddy current losses. The lower core loss reduces heat generation and increases the transformer life. Amorphous core transformers not only reduce the core loss, but also decrease CO_2 emissions and transformer noise (Hasegawa & Azuma, 2008). Amorphous steel is more expensive than silicon steel. However, with a significantly lower power loss, amorphous steel could be used in partial core transformers as the core material.

Overall, the different lamination orientations (parallel oriented and radially oriented) can be combined with amorphous steel to improve the efficiency of the partial core transformer and minimize leakage.

Chapter 8

CONCLUSION

This thesis started with a new perspective of eddy current loss in a single lamination of a transformer under uniform flux conditions. An experiment using a uniform flux generator was then performed on two billets of core material laminated in different directions, to measure the total (billet and winding) power dissipated. The differences in eddy current power loss due to the different lamination orientations were calculated and compared. The eddy current power loss equations under a uniform flux condition were supported by experimentation.

Under uniform flux conditions, the power loss in a cubical billet with the laminations orthogonal to the main flux, has been mathematically shown to be larger than that of a cubic billet with the laminations aligned with the main flux, as long as the number of laminations is greater than 2. The experiments simulated using a FEA program showed the flux pattern from each apparatus and the difference between the two lamination alignments. Experimental results give two scale factors for the developed theory. With better construction and more uniform flux generation (shown from the simulations), the scale factor from the second set of apparatus was more realistic and can be taken as unity.

The flux pattern for a cubical core was reviewed. Three key factors were introduced to simplify the calculation of the flux conditions of the core. Using simulations from MagNet, a partial core side view with the flux patterns from two orthogonal angles was displayed. A flux linkage comparison between the experimental results and the returned values from MagNet reflected the high accuracy of the flux plot in MagNet. An eddy current resistance and eddy current power loss model was then built. The relationships

between three key factors were discovered using the open circuit test results from six cubical partial core transformers. Applying the developed core loss model associated with the key factors, an open circuit test was performed on the cubical partial core transformer PC8. The test results support applying the core loss model to a cubical partial core transformer.

The geometry and construction differences between the cubical core and a cylindrical core were compared. Orthogonal flux assumptions for the cylindrical core through two directions 'b' and 'c' were made. The flux penetration between two adjacent blocks in the cylindrical core was studied, and a cylindrical core loss model was built. Three examples were examined using the developed core loss model. Experimental results determined the validity of the developed core loss model. Visualization of the core loss was represented by the temperature distribution on the surface of the core. An eddy current power loss comparison was made between the previous method and the developed method. The results confirmed a significant improvement using the developed core loss model.

Possible future developments for partial-core loss reduction were presented.

Bibliography

Bell, S. C. (2008). *High-voltage partial-core resonant transformers*. Phd thesis, University of Canterbury.

Bendre, V., Bodger, P., & Wood, A. (2008). Towards a practical partial core transformer - compensation of reactive power requirements with a vsc. In *IASTED Africa Conference on Power and Energy Systems*, (pp. 32–37). Gaborone, Botswana.

Bodger, P., & Enright, W. (2004). A resonant transformer for high voltage testing of generator stators. *Australian Journal of Electrical and Electronics Engineering*, *1(3)*, 179–185.

Bodger, P., Haper, D., Gazzard, M., O'Neill, M., & Enright, W. (2002a). Towards a usable mains frequency partial core transformer. In *Australasian Universities Power Engineering Conference (AUPEC)*. Melbourne, Australia.

Bodger, P., Harper, D., Gazzard, M., O'Neill, M., & Enright, W. (2002b). Testing full-core and partial core transformers at ambient and cryogenic temperatures. In *Electricity Engineers Association Conference (EEA)*, (pp. 21–23). Christchurch, New Zealand.

Bodger, P., & Liew, M. (2001). Reverse as-built transformer design method. *International Journal of Electrical Engineering Education (IJEEE)*, *39(1)*, 42–53.

Bodger, P. S., Enright, W. G., & Ho, V. (2005). A low voltage, mains frequency, partial core, high temperature, superconducting transformer. *Australasian Universities Power Engineering Conference (AUPEC)*, *1*, 73–78.

Bodger, P. S., Liew, M. C., & Johnstone, P. T. (2000). A comparison of conventional and reverse transformer design. In *Australasian Universities Power Engineering Conference (AUPEC)*, (pp. 80–85). Brisbane, Australia.

Davies, E. J. (1990). *Conduction and Induction Heating*. London, U.K.: P. Peregrinus Ltd, 1st ed.

DEL VECCHIO, R., & SEFKO, J. (1981). Experimental test of loss calculations for thin laminations in the presence of normal sinusoidal flux. *IEEE Transactions on Magnetics*, *17 (2)*, 1248–1250.

Del Vecchio, R. M., Poulin, B., Feghali, P. T., Shah, D., & Ahuja, R. (2002). *Transformer Design Principles with Applications to Core-Form Power Transformers*, vol. Chapter 1.1. USA: Taylor & Francis.

Dol, M. J. (1986). Rapid through- transheating of copper. Tech. rep., Third Professional Year Project, University of Canterbury.

Eastop, T. D., & Mcconkey, A. (1986). *Applied Thermodynamics for Engineering Technologists*, vol. Chapter 17. New York: Wiley.

Enright, W. G., & Bodger, P. S. (2004). Short time rated and protected high voltage ac testing of generator stators using parallel resonant circuits. In *Electricity Engineers Association Conference (EEA)*. Christchurch, New Zealand.

FLUKE Corporation, F. (1995). *FLUKE 41B Power Harmonics Tester Users Manual*. FLUKE Corporation.

FLUKE Corporation, F. (2001). *FLUKE 43B Power Quality Analyzer Users Manual*. FLUKE Corporation.

FLUKE Corporation, F. (2006a). *FLUKE 434 Three Phase Power Quality Analyzer Users Manual*. FLUKE Corporation.

FLUKE Corporation, F. (2006b). *FLUKE Ti20 Thermal Imager Users Manual*. FLUKE Corporation.

Harlow, J. H. (2007). *Electric power transformer engineering*, vol. Chapter 2. CRC Press (Taylor & Francis Group), 2nd ed.

Hasegawa, R., & Azuma, D. (2008). Impacts of amorphous metal-based transformers on energy efficiency and environment. *Magnetism and Magnetic Materials*, *320, Issue 20*, 2451–2456.

Heathcote, M. J. (2007). *The J&P Transformer Book*. Elsevier Ltd, 13th ed.

Infolytica, C. (2007). *Magnetostatic Time-Harmonic Transient 2D & 3D Tutorials*. Inforlytica Corporation.

Infolytica, C. (2009). Magnet trial edition. [Online].
URL `http://www.infolytica.com/en/products/trial/magnet.aspx`

Kubo, H., T.and Sachs, & Nadel, S. (2001). Opportunities for new appliance and equipment efficiency standards: Energy and economic savings beyond current standards programs. In *American Council for an Energy-Efficient Economy*, (p. 39). Washington, D.C., USA.

Kucuk, I., & Derebasi., N. (2006). Prediction of power losses in transformer cores using feed forward neural network and genetic algorithm. *Measurement*, *39 (7)*, 605–611.

Liew, M., & Bodger, P. (2001). Partial-core transformer design using reverse modelling techniques. *Electric Power Applications, IEE*, *148 (6)*, 513–519.

Liew, M. C. (2001). *Reverse design transformer modelling technique with particular application to partial core transformers*. Phd thesis, University of Canterbury.

Liew, M. C., O'Neill, M. B., & Bodger, P. S. (2001). Operating partial core transformer under liquid nitrogen conditions. *IEE Proc. Electric Power Applications*, *148 (4)*, 293–298.

McPHERSON, G., & LARAMORE, R. D. (1990). *An introduction to electrical machines and transformers*. Wiley.

O'Neill, M., Enright, W., & Bodger, P. (2000). The green-transformer: a liquid nitrogen filled power transformer. In *Electricity Engineers Association Conference (EEA)*, (pp. 71–75). Auckland, New Zealand.

Paul, C. R., Nasar, S. A., & Unnewehr, L. E. (1986). *Introduction to Electrical Engineering*. Singapore: McGraw-Hill, 1st ed.

Poole, C. (2000). *Handbook of Superconductivity*. Academic Press.

Sippola, M., & Sepponen, R. (2002). Accurate prediction of high-frequency power-transformer losses and temperature rise. *IEEE Transactions on Power Electronics*, *17 (5)*, 835–847.

Slemon, G. R. (1966). *Magnetoelectric Devices: Transducers, Transformers, and Machines*. USA: John Wiley and Sons, Inc.

Tera Analysis, L. (2001). Students' quickfield 4.2t. [Online].
URL `http://www.quickfield.com/free_soft.htm`.

Tjoa, A. (2006). Partial core resonating transformer for arc sign. Third professional year project, University of Canterbury.

Unknown, N. (2009). Energy efficient distribution transformers. *Australian Power Technologies, Transmission & Distribution*, *Issue 5*, 54.

APPENDICES

Appendix 1: Copper Mockup – MPCTF Configuration Data

Core	
Length	484mm
Inner radius	8.2mm
Outer radius	40mm
Number of laminations	348
Lamination thickness	0.23mm
Stacking Factor	0.95
Former	
Winding former radius	53mm
Inter-layer insulation	
NMN thickness	0.35mm
Reinforcing tape	0.13mm
Windings	
Two windings of 3.5mm copper wire	
Inside winding (secondary)	
Layers	3
Turns per layer	103
Winding window length	380mm
Outside winding (primary)	
Layers	3
Turns per layer	103
Winding window length	380mm

Table A.1: Physical details for Mockup partial core transformer.

Appendix 2: New Core Loss Model Data for MPCTF

A sample layout of new core loss model worksheets for MPCTF in this thesis is presented here.

DC Resistance Test (ohm) @ 15degree

RA1A2 2.44E-01

Ra1a2 2.02E-01

Winding details	N1=N2 (turns)	w1=w2	w12	Ly1	I1=I2	Ly2	Winding axial length (m)
	309	3.50E-03	0	3	0.00063	3	0.405

Core details	Lc (m)	Tc (m)	Weight of Core (kg)	SFc	Core Radius (m)	CrossSectionArea (m^2)	ρ (ohm m) @ 20C
	0.484	0.00023	**15.366**	0.96	0.0398	4.78E-03	1.68E-08

Three Key Factors **Aspect Ratio βa** **Kec** **L' Factor**

t_{12} (m) β_a 0.62 27.99%

2.48E-02 16.344

$$\beta_a = \frac{l_w}{\tau_{12}} \qquad K_{ec} = 0.013\beta_a + 0.409 \qquad L' = \left(9.34 \cdot \left(\frac{l_c}{l_w}\right) + 16.83\right)\%$$

Input voltage (V) 230.000

Frequency (Hz) 50

Open Circuit Test

Vin (V) rms	Iin (A) rms	Pmeasured(W)	Vout(V)=e1
230.00	22.10	240.00	228.00

Calculations

Pwinding (W)	Phys (W)		Peddy (W)		Total Loss (W)
122.103	43.898	Peca1 (W)	Pecb (W)	Pecc (W)	232.994
		2.463	63.966	0.565	

Figure A.1: Physcial details of the core, test results for $l_c = 484mm$ and the corresponding calculated result.

Kh	x	V1 (V)	N1 (turns)	f (Hz)	Ac (m^2)	Core Weight (kg)
0.110	1.850	230.000	309.000	50.000	4.78E-03	15.366

Flux Density	Bc (T)
	0.702

$$P_h = W T_c \cdot K_h \cdot f \cdot B_{core}^{x}$$

Hysteresis Loss	Phys (W)
	43.898

Figure A.2: Hysteresis loss data.

Block A

Lamination (piece)	Block Thickness (m) Single	Ac (m^2)	Kec	N1
3.40E+01	7.82E-03	4.78E-03	0.62	309

e1 (V)	Voltage distribution in Block A (V)	e1/Nlam in Block A (V)
230	3.01E+01	8.86E-01

Side Area (m^2)	Induced voltage in direction 'b' & 'c' in this block (V)
1.08E-02	1.87E+01

Frequency (Hz)	Uo	Ureq
50	1.25664E-06	2.00E+03

ρc (ohm.meter) @20?C	Wc (m)	Lc (m)	Tc (m)	δ (m)	L' (m)
0.00000018	8.00E-02	0.484	2.30E-04	6.75E-04	0.135480682

Middle

Resistance of Single Lamination	Recam (ohm@20?C)	$R_{ec_{am}} = \rho_{core} \bullet \frac{4W_{core}}{(l_{core} - 2L') \times T_{core}}$
	1.18E-03	
Power of Single Lamination	P'ecam (W@20?C)	
	6.68E+02	
Power of Single lamination refered to the primary	Pecam (W@20?C)	$P_{ec_{am}} = \frac{\left(\frac{e_1}{N_1 \cdot n_{lam}}\right)^2}{R_{ec_{am}}} \cdot n_{lam}$
	6.99E-03	
Total power loss from the middle section	Pecam (W@20?C) Tot	
	2.38E-01	

Figure A.3: Calculated data of Block A using developed method.

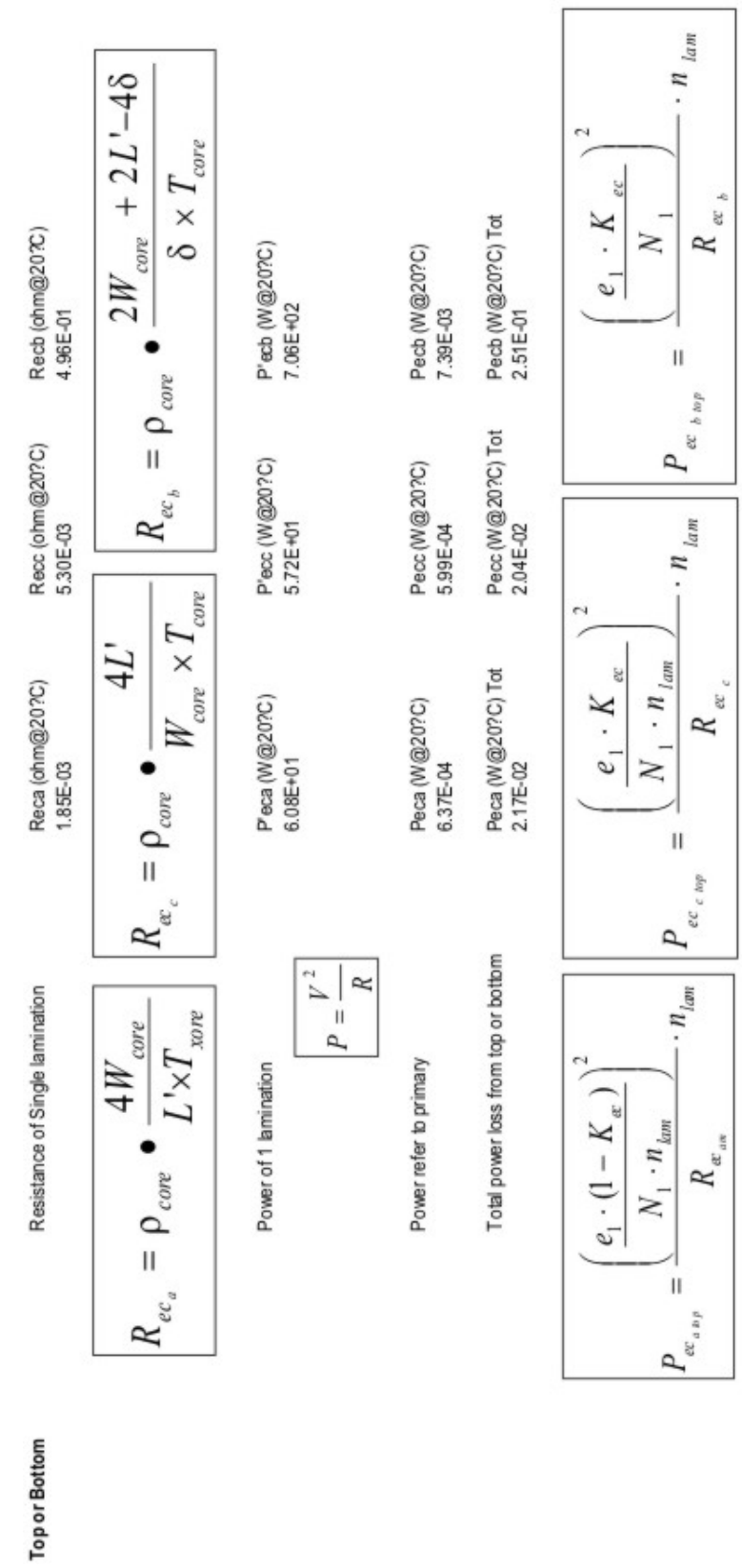

Figure A.4: (Continued) Calculated data of Block A using developed method.

Block B

Lamination (piece)	Block Thickness (m)	Ac (m^2)	Kec	N1
3.40E+01	7.82E-03	4.78E-03	0.62	309

e1 (V)	Voltage distribution in Block B (V)	e1/Nlam in Block B (V)
230	2.94E+01	8.64E-01

Side Area (m^2)	Induced voltage in direction 'b' & 'c' in this block (V)	Total Induced voltage in direction 'b' & 'c' (V)
1.06E-02	1.82E+01	3.65E+01

ρc (ohm.meter) @20?C	Wc (m)	Lc (m)	Tc (m)	δ (m)	L' (m)
0.00000018	7.80E-02	0.484	230E-04	6.75E-04	0.135480682

Middle	Resistance of Single Lamination	Recam (ohm @20?C)	$R_{ec_{am}} = \rho_{core} \bullet \frac{4W_{core}}{(l_{core} - 2L') \times T_{core}}$	
		1.15E-03		
	Power of Single Lamination	P'ecam (W@20?C)		
		6.51E+02		
	Power of Single lamination refered to the primary	Pecam (W@20?C)	$P_{ec_{am}} = \frac{\left(\frac{e_1}{N_1 \cdot n_{lam}}\right)^2}{R_{ec_{am}}} \cdot n_{lam}$	
		6.82E-03		
	Total power loss from the middle section	Pecam (W@20?C) Tot		
		2.32E-01		

Figure A.5: Calculated data of Block B using developed method.

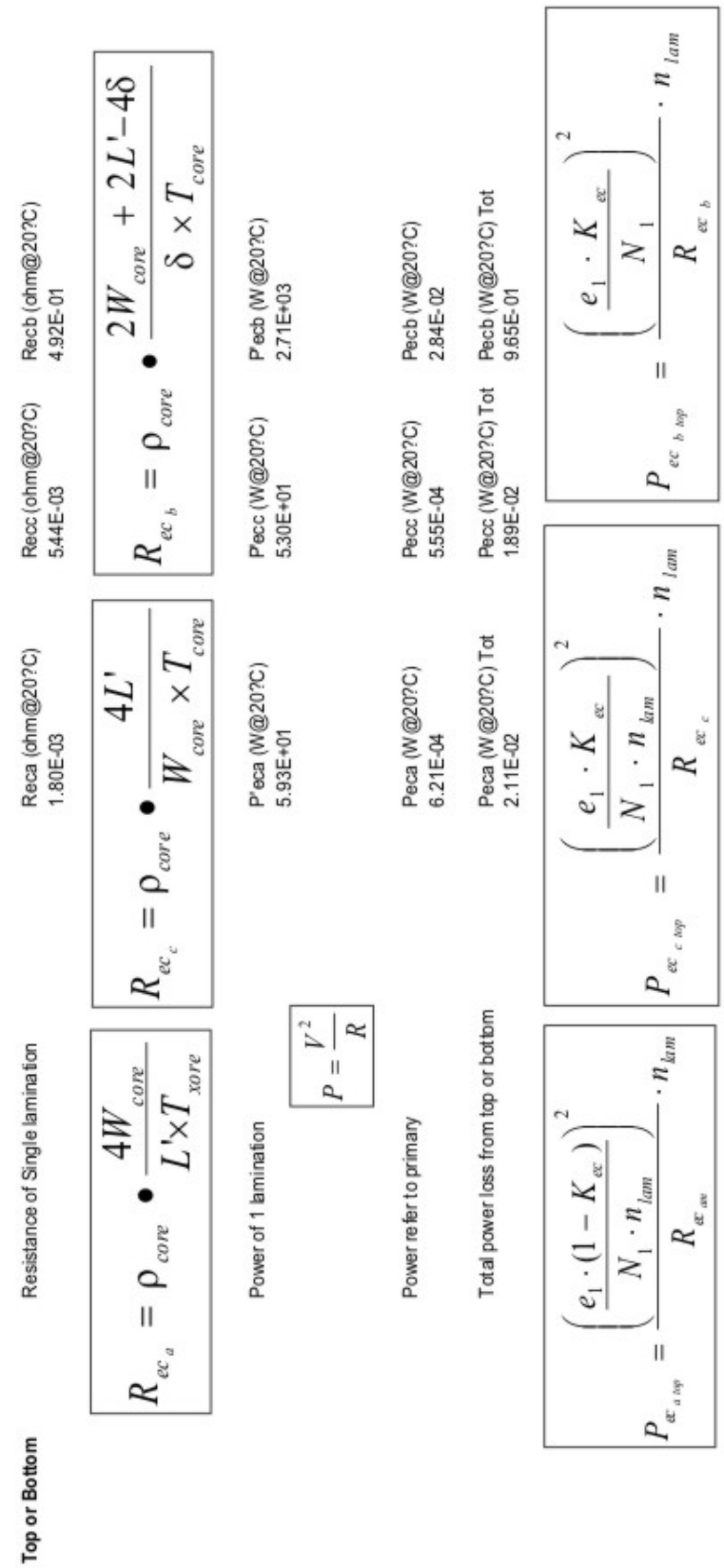

Figure A.6: (Continued) Calculated data of Block B using developed method.

Block C

Lamination (piece)	Block Thickness (m)	Ac (m^2)	Kec	N1
1.60E+01	3.68E-03	4.78E-03	0.62	309

e1 (V)	Voltage distribution in Block C (V)	e1/Nlam in Block C (V)
230	1.35E+01	8.42E-01

Side Area (m^2)	Induced voltage in direction 'b' & 'c' in this block (V)	Total Induced voltage in direction 'b' & 'c' (V)
1.03E-02	8.37E+00	4.39E+01

ρc (ohm.meter) @20?C	Wc (m)	Lc (m)	Tc (m)	δ (m)	L' (m)
0.00000018	7.60E-02	0.484	2.30E-04	6.75E-04	0.135480682

Middle	Resistance of Single Lamination	Recam (ohm@20?C)	$R_{ec_{am}} = \rho_{core} \bullet \frac{4W_{core}}{(l_{core} - 2L') \times T_{core}}$	
		1.12E-03		
	Power of Single Lamination	P'ecam (W@20?C)		
		6.34E+02		
	Power of Single lamination refered to the primary	Pecam (W@20?C)	$P_{ec_{am}} = \frac{\left(\frac{e_1}{N_1 \cdot n_{lam}}\right)^2}{R_{ec_{am}}} \cdot n_{lam}$	
		6.64E-03		
	Total power loss from the middle section	Pecam (W@20?C) Tot		
		1.06E-01		

Figure A.7: Calculated data of Block C using developed method.

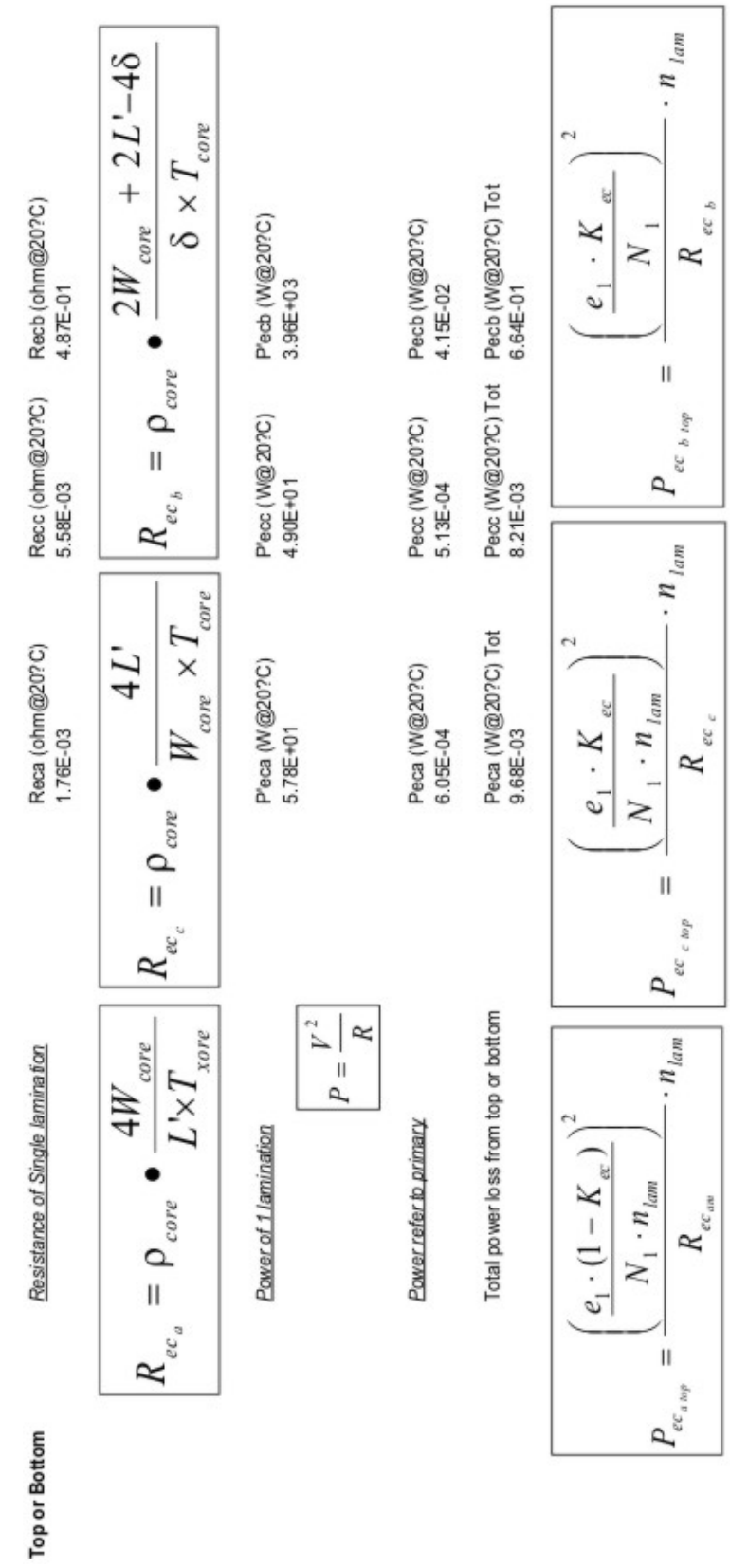

Figure A.8: (Continued) Calculated data of Block C using developed method.

Block D

Lamination (piece)	Block Thickness (m)	Ac (m^2)	Kec	N1
1.60E+01	3.68E-03	4.78E-03	0.62	309

e1 (V)	Voltage distribution in Block D (V)	e1/Nlam in Block D (V)
230	1.29E+01	8.06E-01

Side Area (m^2)	Induced voltage in direction 'b' & 'c' in this block (V)	Total Induced voltage in direction 'b' & 'c' (V)
9.86E-03	8.02E+00	5.01E+01

ρc (ohm.meter) @20?C	Wc (m)	Lc (m)	Tc (m)	δ (m)	L' (m)
0.00000018	7.28E-02	0.484	2.30E-04	6.75E-04	0.13548682

Middle	Resistance of Single Lamination	Recam (ohm@20?C)	$R_{ec_{am}} = \rho_{core} \bullet \frac{4W_{core}}{(l_{core} - 2L') \times T_{core}}$
		1.07E-03	
	Power of Single Lamination	P'ecam (W@20?C)	
		6.07E+02	
	Power of Single lamination refered to the primary	Pecam (W@20?C)	$P_{ec_{am}} = \frac{\left(\frac{e_1}{N_1 \cdot n_{lam}}\right)^2}{R_{ec_{am}}} \cdot n_{lam}$
		6.36E-03	
	Total power loss from the middle section	Pecam (W@20?C) Tot	
		1.02E-01	

Figure A.9: Calculated data of Block D using developed method.

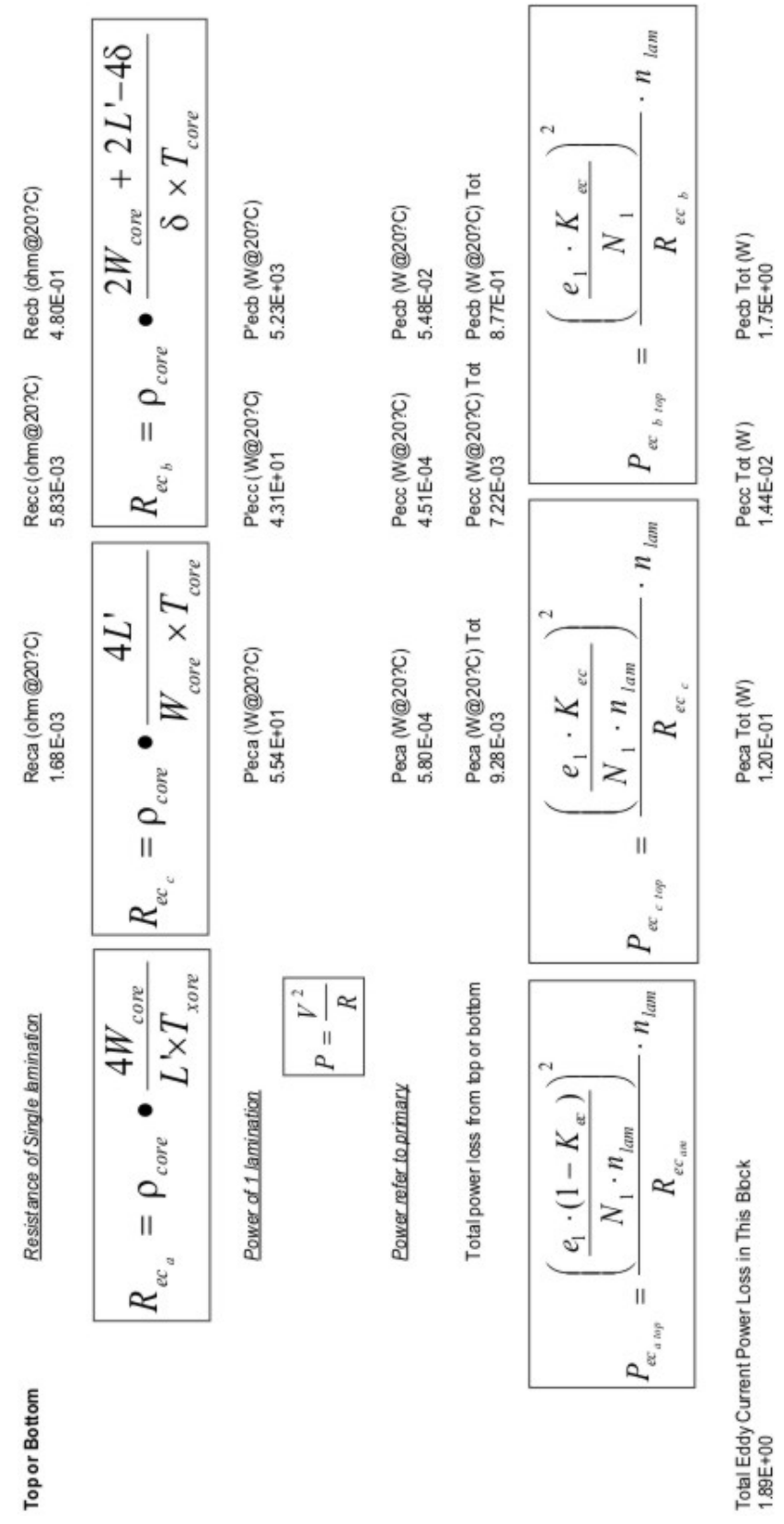

Figure A.10: (Continued) Calculated data of Block D using developed method

Block E

Lamination (piece)	Block Thickness (m)	Ac (m^2)	Kec	N1
1.60E+01	3.68E-03	4.78E-03	0.62	309

e1 (V)	Voltage distribution in Block E (V)	e1/Nlam in Block E (V)
230	1.21E+01	7.59E-01

Side Area (m^2)	Induced voltage in direction 'b' & 'c' in this block (V)	Total Induced voltage in direction 'b' & 'c' (V)
9.28E-03	7.54E+00	5.47E+01

ρc (ohm.meter) @20?C	Wc (m)	Lc (m)	Tc (m)	δ (m)	L' (m)
0.00000018	6.85E-02	0.484	2.30E-04	6.75E-04	0.135480682

Middle			
Resistance of Single Lamination	Recam (ohm@20?C)	$R_{ec_{lam}} = \rho_{core} \bullet \frac{4W_{core}}{(l_{core} - 2L') \times T_{core}}$	
	1.01E-03		
Power of Single Lamination	P'ecam (W@20?C)		
	5.72E+02		
Power of Single lamination refered to the primary	Pecam (W@20?C)	$P_{ec_{lam}} = \frac{\left(\frac{e_1}{N_1 \cdot n_{lam}}\right)^2}{R_{ec_{lam}}} \cdot n_{lam}$	
	5.99E-03		
Total power loss from the middle section	Pecam (W@20?C) Tot		
	9.58E-02		

Figure A.11: Calculated data of Block E using developed method.

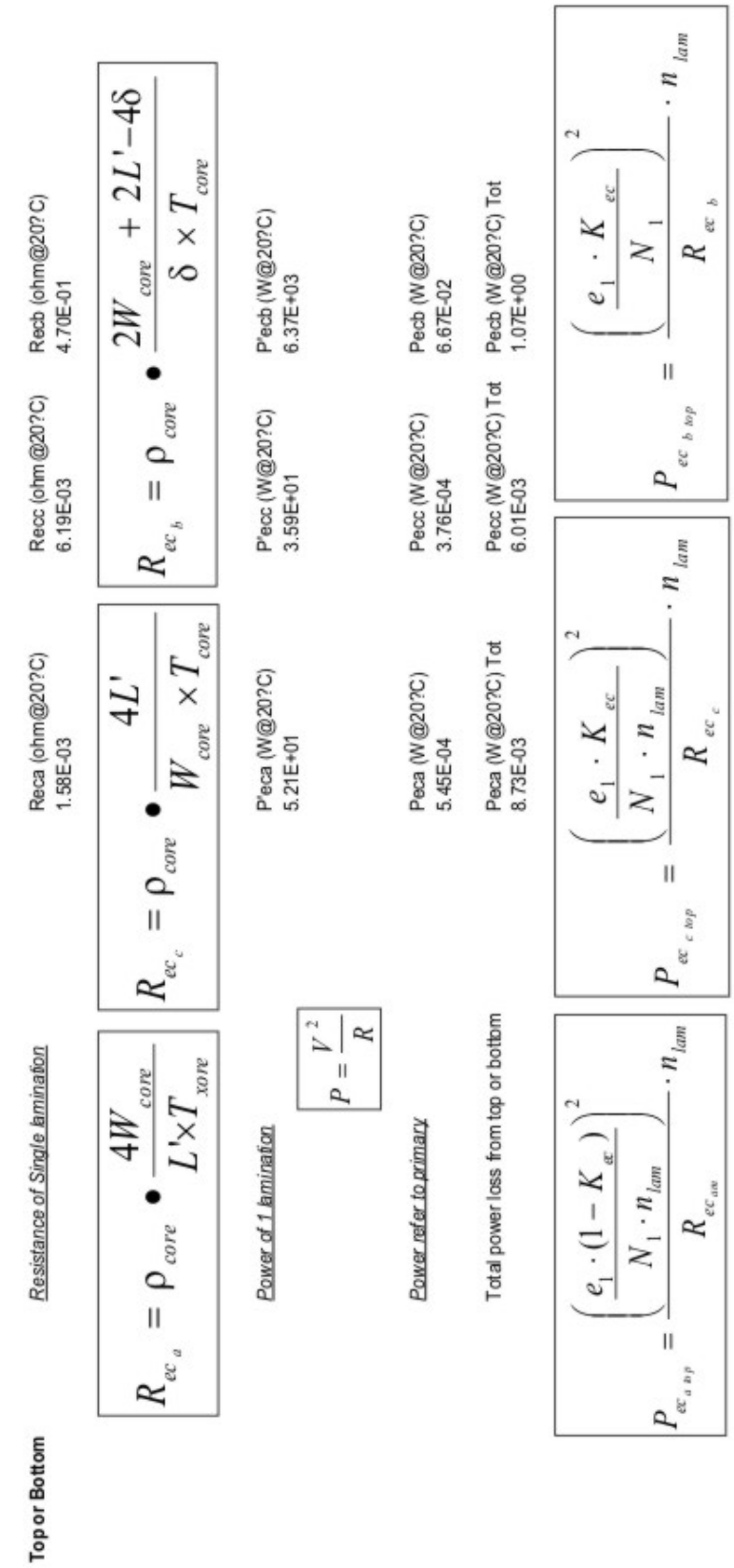

Figure A.12: (Continued) Calculated data of Block E using developed method.

Block F

Lamination (piece)	Block Thickness (m)	Ac (m^2)	Kec	N1
1.60E+01	3.68E-03	4.78E-03	0.62	309

e1 (V)	Voltage distribution in Block F (V)	e1/Nlam in Block F (V)
230	1.11E+01	6.94E-01

Side Area (m^2)	Induced voltage in direction 'b' & 'c' in this block (V)	Total Induced voltage in direction 'b' & 'c' (V)
8.49E-03	6.90E+00	5.70E+01

ρc (ohm.meter) @20?C	Wc (m)	Lc (m)	Tc (m)	δ (m)	L' (m)
0.00000018	6.27E-02	0.484	2.30E-04	6.75E-04	0.135480682

Middle			
	Resistance of Single Lamination	Recam (ohm@20?C)	$R_{ec_{lam}} = \rho_{core} \bullet \frac{4W_{core}}{(l_{core} - 2L') \times T_{core}}$
		9.21E-04	
	Power of Single Lamination	Pecam (W@20?C)	
		5.23E+02	
	Power of Single lamination refered to the primary	Pecam (W@20?C)	$P_{ec_{tot}} = \frac{\left(\frac{e_1}{N_1 \cdot n_{lam}}\right)^2}{R_{ec_{tot}}} \cdot n_{lam}$
		5.48E-03	
	Total power loss from the middle section	Pecam (W@20?C) Tot	
		8.77E-02	

Figure A.13: Calculated data of Block F using developed method.

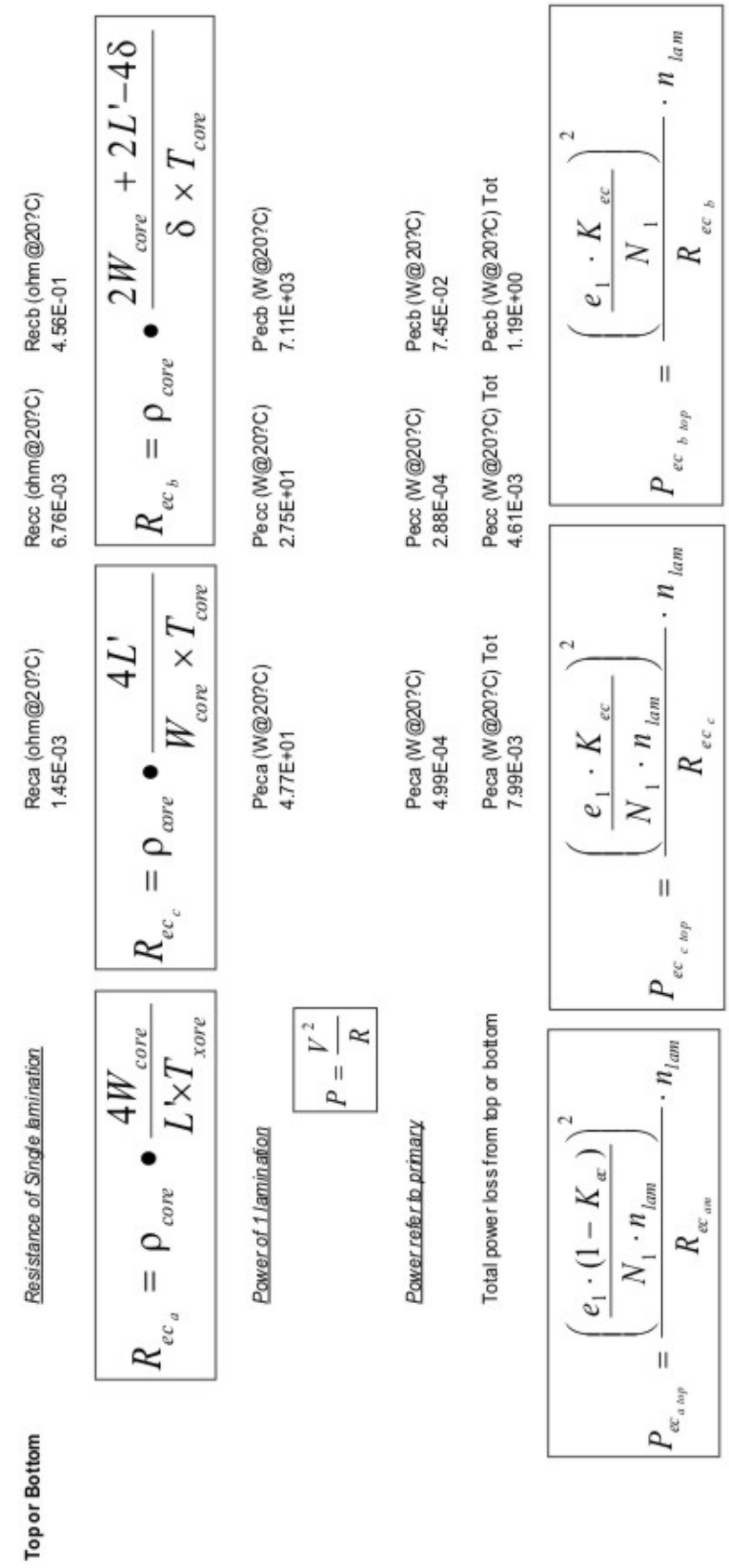

Figure A.14: (Continued) Calculated data of Block F using developed method.

Block G

Lamination (piece)	Block Thickness (m)	Ac (m^2)	Kec	N1
1.60E+01	3.68E-03	4.78E-03	0.62	309

e1 (V)	Voltage distribution in Block G (V)	e1/Nlam in Block G (V)
230	9.76E+00	6.10E-01

Side Area (m^2)	Induced voltage in direction 'b' & 'c' in this block (V)	Total Induced voltage in direction 'b' & 'c' (V)
7.46E-03	6.07E+00	5.61E+01

ρc (ohm.meter) @20?C	Wc (m)	Lc (m)	Tc (m)	δ (m)	L' (m)
0.00000018	5.51E-02	0.484	2.30E-04	6.75E-04	0.13548682

Middle			
	Resistance of Single Lamination	Recam (ohm@20?C)	$R_{ec_{am}} = \rho_{core} \bullet \frac{4W_{core}}{(l_{core} - 2L) \times T_{core}}$
		8.10E-04	
	Power of Single Lamination	P'ecam (W@20?C)	
		4.60E+02	
	Power of Single lamination refered to the primary	Pecam (W@20?C)	$P_{ec_{am}} = \frac{\left(\frac{e_1}{N_1 \cdot n_{lam}}\right)^2}{R_{ec_{am}}} \cdot n_{lam}$
		4.82E-03	
	Total power loss from the middle section	Pecam (W@20?C) Tot	
		7.70E-02	

Figure A.15: Calculated data of Block G using developed method.

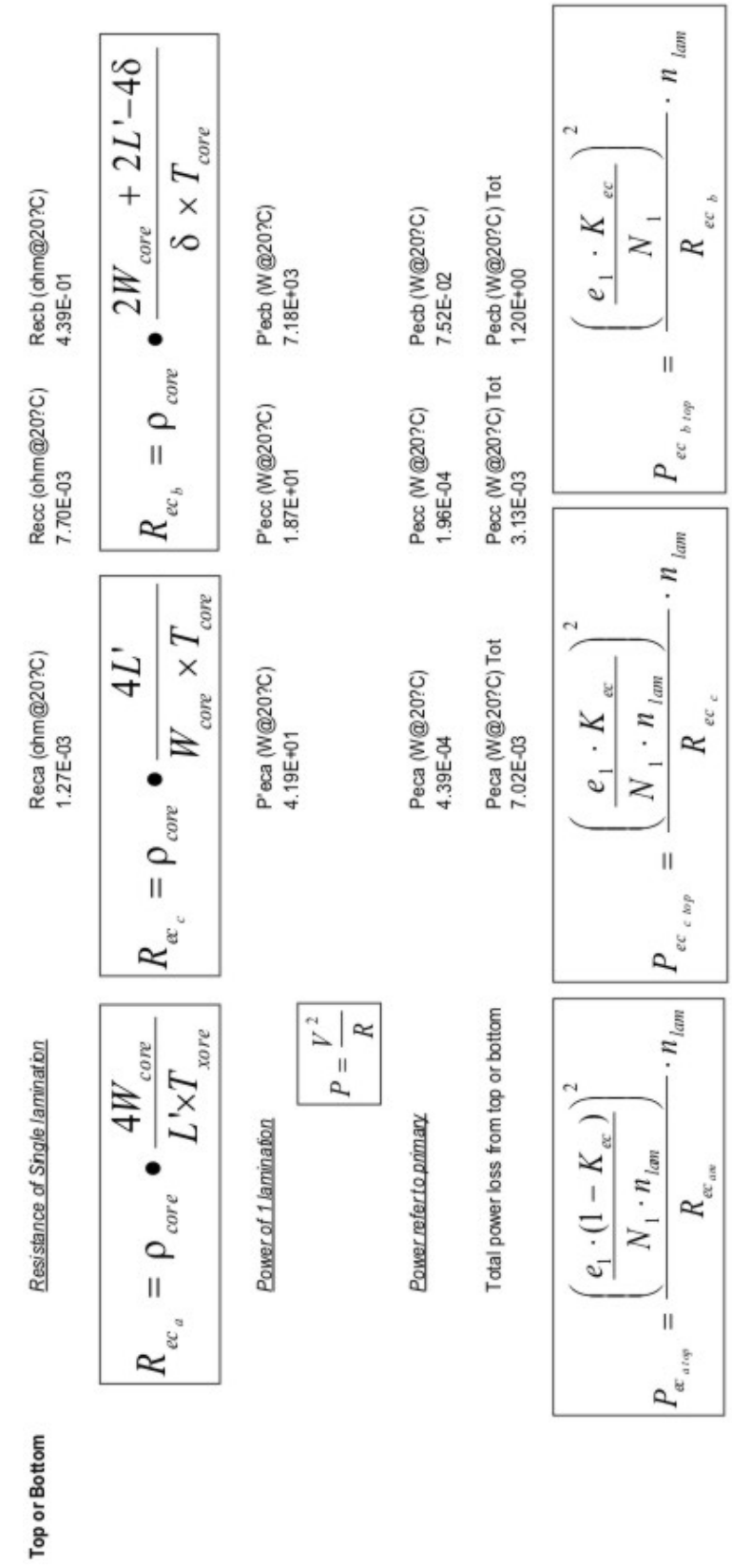

Figure A.16: (Continued) Calculated data of Block G using developed method.

Block H

Lamination (piece)	Block Thickness (m)	Ac (m^2)	Kec	N1
1.60E+01	3.68E-03	4.78E-03	0.62	309

e1 (V)	Voltage distribution in Block H (V)	e1/Nlam in Block H (V)
230	7.95E+00	4.97E-01

Side Area (m^2)	Induced voltage in direction 'b' & 'c' in this block (V)	Total Induced voltage in direction 'b' & 'c' (V)
6.08E-03	4.94E+00	5.14E+01

ρc (ohm.meter) @20?C	Wc (m)	Lc (m)	Tc (m)	δ (m)	L' (m)
0.00000018	4.49E-02	0.484	2.30E-04	6.75E-04	0.13548068

Middle	Resistance of Single Lamination	Recam (ohm @20?C)	$R_{ec_{am}} = \rho_{core} \bullet \frac{4W_{core}}{(l_{core} - 2L') \times T_{core}}$
		6.60E-04	
	Power of Single Lamination	P'ecam (W@20?C)	
		3.75E+02	
	Power of Single lamination refered to the primary	Pecam (W@20?C)	$P_{ec_{am}} = \frac{\left(\frac{e_1}{N_1 \cdot n_{lam}}\right)^2}{R_{ec_{am}}} \cdot n_{lam}$
		3.92E-03	
	Total power loss from the middle section	Pecam (W@20?C) Tot	
		6.28E-02	

Figure A.17: Calculated data of Block H using developed method.

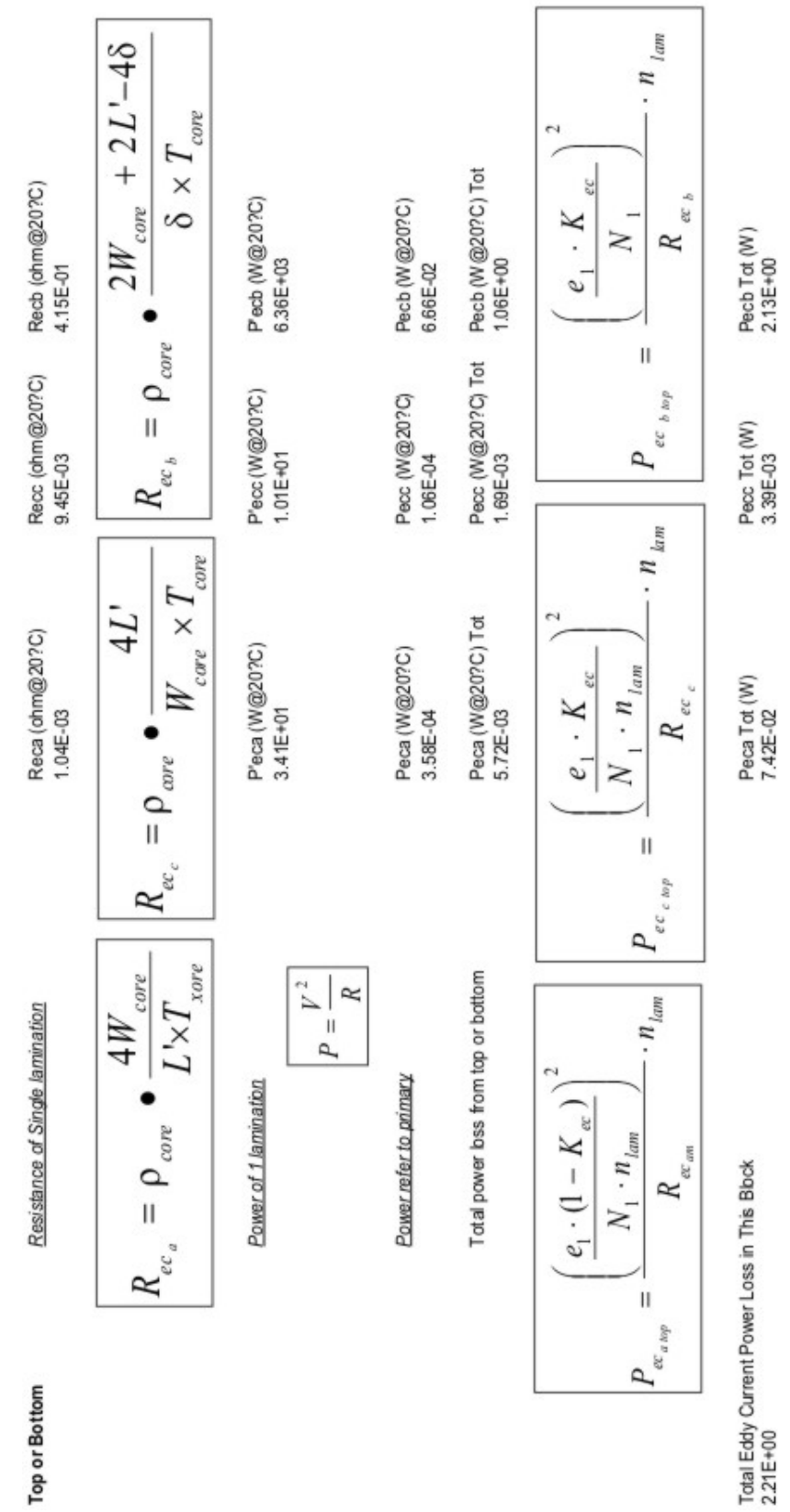

Figure A.18: (Continued) Calculated data of Block H using developed method.

Block I

Lamination (piece)	Block Thickness (m)	Ac (m^2)	Kec	N1
1.60E+01	3.68E-03	4.78E-03	0.62	309

e1 (V)	Voltage distribution in Block I (V)	e1/Nlam in Block I (V)
230	5.16E+00	3.22E-01

Side Area (m^2)	Induced voltage in direction 'b' & 'c' in this block (V)	Total Induced voltage in direction 'b' & 'c' (V)
3.94E-03	3.20E+00	4.01E+01

ρc (ohm.meter) @20?C	Wc (m)	Lc (m)	Tc (m)	δ (m)	L' (m)
0.00000018	2.91E-02	0.484	2.30E-04	6.75E-04	0.13548682

Middle	Resistance of Single Lamination	Recam (ohm@20?C)	$R_{ec_{am}} = \rho_{core} \bullet \frac{4W_{core}}{(l_{core} - 2L') \times T_{core}}$
		4.28E-04	
	Power of Single Lamination	P'ecam (W@20?C)	
		2.43E+02	
	Power of Single lamination refered to the primary	Pecam (W@20?C)	$P_{ec_{tot}} = \frac{\left(\frac{e_1}{N_1 \cdot n_{lam}}\right)^2}{R_{ec_{tot}}} \cdot n_{lam}$
		2.54E-03	
	Total power loss from the middle section	Pecam (W@20?C) Tot	
		4.07E-02	

Figure A.19: Calculated data of Block I using developed method.

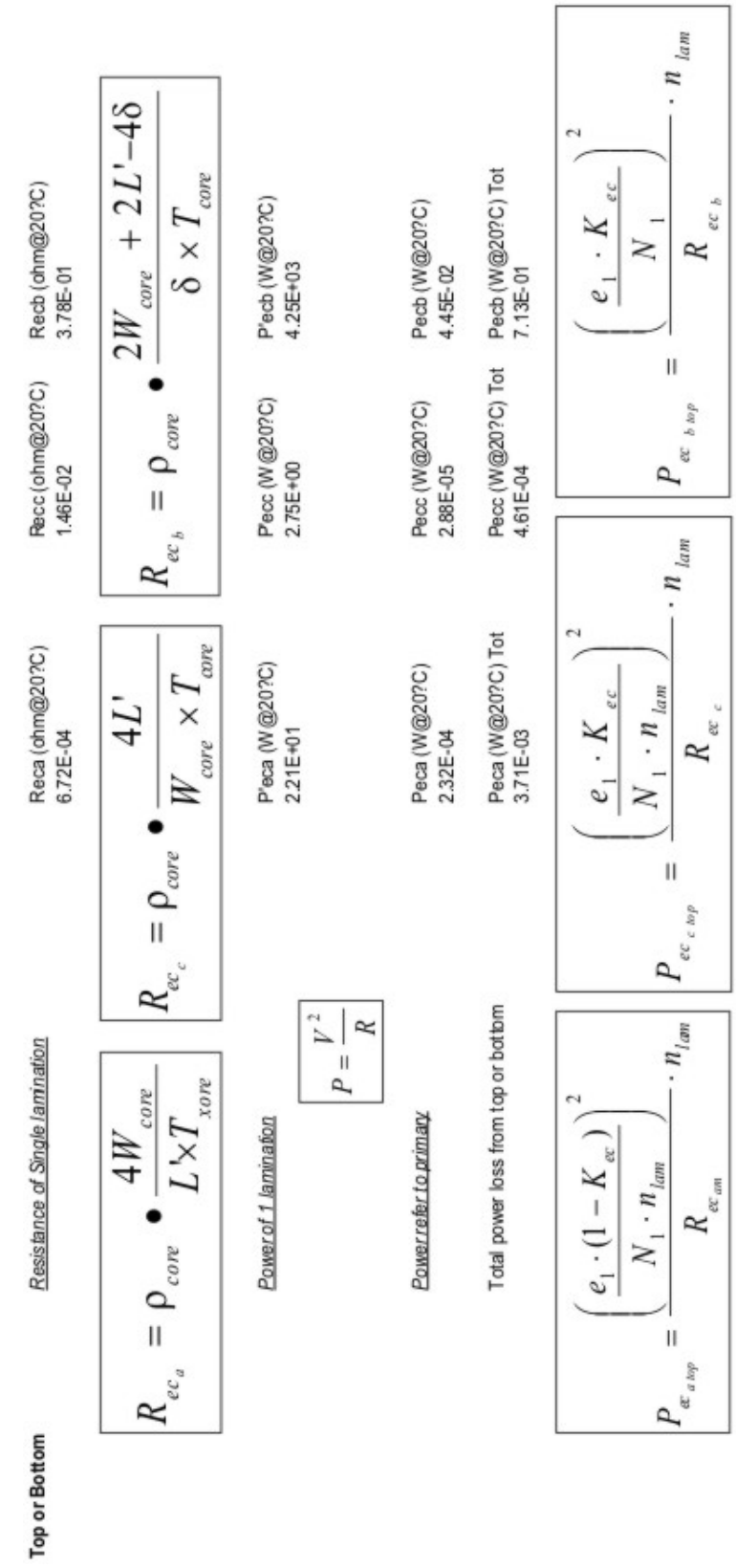

Figure A.20: (Continued) Calculated data of Block I using developed method.